University of Kentucky Master's Theses   Graduate School

2011

EXPERIMENTAL FLOW VISUALIZATION FOR CORRUGATED AIRFOILS AT LOW REYNOLDS NUMBER INCLUDING DEVELOPMENT OF A PITCH AND PLUNGE FIXTURE

Jeremy Ryan Sparks
University of Kentucky, Jeremy.Sparks@uky.edu

Click here to let us know how access to this document benefits you.

Recommended Citation

Sparks, Jeremy Ryan, "EXPERIMENTAL FLOW VISUALIZATION FOR CORRUGATED AIRFOILS AT LOW REYNOLDS NUMBER INCLUDING DEVELOPMENT OF A PITCH AND PLUNGE FIXTURE" (2011). *University of Kentucky Master's Theses*. 141.
https://uknowledge.uky.edu/gradschool_theses/141

ABSTRACT OF THESIS

EXPERIMENTAL FLOW VISUALIZATION FOR CORRUGATED AIRFOILS AT LOW REYNOLDS
NUMBER FLOW INCLUDING DEVELOPMENT OF A PITCH AND PLUNGE FIXTURE

Micro Air Vehicles (MAV's) have small size and extreme maneuverability which makes
them ideal for surveillance. Propulsion mechanisms include propellers, rotors, and
flapping airfoils. Flapping motions, along with biologically-inspired wing profiles, are of
interest due to their use of natural physics. Corrugated airfoil structures appears to
have poor aerodynamic performance at higher Reynolds numbers, but serve well at
Re<10,000. Understanding flow structures around corrugated profiles and comparing
them to a standard airfoil will aid in understanding how these corrugated profiles
perform well and have been adopted by some of nature's most acrobatic flyers.
Motivation for this investigation is to compare static flow visualizations of corrugated
profiles to a standard National Advisory Committee for Aeronautics (NACA) airfoil from
low to high angles of attack and further observe flow structure development of a
pitching and plunging flat plate at a Re<10,000 and a Strouhal number relevant to
natural fliers. The static visualization was conducted at Re=1,000 with a NACA 0012
airfoil and two corrugated models. The Pitch and Plunge Fixture (PPF) developed was
constructed by simplifying flapping wings as a two degree of freedom motion in plunge
(translation) and pitch (rotation). Results obtained from the PPF were compared with a
numerical simulation.

KEYWORDS: CORRUGATED AIRFOIL, DRAGONFLY, LOW REYNOLDS NUMBER, MICRO AIR
VEHICLES (MAV's), PITCH AND PLUNGE

Jeremy Sparks
July 17, 2011

EXPERIMENTAL FLOW VISUALIZATION FOR CORRUGATED AIRFOILS AT LOW REYNOLDS
NUMBER FLOW INCLUDING DEVELOPMENT OF A PITCH AND PLUNGE FIXTURE

By

Jeremy Ryan Sparks

Dr. Suzanne Weaver Smith
Co-Director of Thesis
Dr. Sean Bailey
Co-Director of Thesis
Dr. James McDonough
Director of Graduate Studies
July 22, 2011

RULES FOR THE USE OF THESES

Unpublished theses submitted for the Master's degree and deposited in the University of Kentucky Library are as a rule open for inspection, but are to be used only with due regard to the rights of the authors. Bibliographical references may be noted, but quotations or summaries of parts may be published only with the permission of the author, and with the usual scholarly acknowledgements.

Extensive copying or publication of the thesis in whole or in part also requires the consent of the Dean of the Graduate School of the University of Kentucky.

A library that borrows this thesis for use by its patrons is expected to secure the signature of each user.

<u>Name</u>   <u>Date</u>

_____

_____

_____

_____

_____

_____

_____

_____

_____

THESIS

Jeremy Ryan Sparks

The Graduate School

University of Kentucky

2011

EXPERIMENTAL FLOW VISUALIZATION FOR CORRUGATED AIRFOILS AT LOW REYNOLDS
NUMBER INCLUDING DEVELOPMENT OF A PITCH AND PLUNGE FIXTURE

_____

THESIS

_____

A thesis submitted in partial fulfillment of the
requirements for the degree of Master of Science in the
College of Engineering at the University of Kentucky

By

Jeremy Ryan Sparks

Lexington, KY

Co-Directors: Dr. Suzanne Weaver Smith, Professor of Mechanical Engineering
and:　　　　　Dr. Sean Bailey, Professor of Mechanical Engineering
Lexington, KY
2011

ACKNOWLEDGEMENTS

While I am responsible for putting words on paper, this research has been a culmination of much support from family, advisors, and even high school kids. Without the support of a strong family, passionate advisors, and oblivious high school baseball players I could not have accomplished this thesis and gained the knowledge associated with it.

Coming from a small town in eastern Kentucky I have had many people around me become content with what comes easy and never accepting a challenge. My Mom and Dad have continually reminded me that anything is possible as long as I kept hard work and dedication in my arsenal. That has been advice which continually keeps me firing. While I may have taken on more responsibility at times than I anticipated, the same hard work and dedication has always kept things in order. I cannot thank them enough for the support and lessons they have taught me along the way.

Dr. Smith has been a tremendous advisor during my time in graduate school. An admirable trait I have yet to attain is her ability to balance a schedule and multiple projects. I am amazed at how she can keep up with progress of such a diverse array of projects being conducted consecutively. I have been extremely fortunate to have her as an advisor while experiencing her own work and dedication bringing strong recognition to the College of Engineering at the University of Kentucky.

I would still never claim myself as an expert in fluid dynamics by any means, but I have gained a great deal of experience in theoretical and experimental fluids from Dr. Bailey. His knowledge of experimentation has been a tremendous asset in developing

Table of Contents

List of Tables

List of Figures

Nomenclature

α = angle of attack

c = chord number

CFD = computational fluid dynamics

c_{max} = maximum chord

DC = direct current

E = modulus of elasticity

f = frequency

f_m = motor frequency

I = inertia

l = length

l_c = characteristic length

l_{rel} = relative span length

MAV = micro air vehicle

n = period

NACA = National Advisory Committee for Aeronautics

P_r = pinion gear radius

P_s = static pressure

P_t = total pressure

Pa = Pascal

ρ = density

ρ_m = mass density

RC = remote controlled

Re_c = chord Reynolds number

St = Strouhal number

t = period

Θ_p = pitch angle

U = velocity

V = voltage

v = kinematic viscosity

Y = plunge amplitude

Chapter 1 : Overview

1.1 Introduction

MAV's (Micro Air Vehicles) serve many purposes ranging from surveillance to recreation. These small vehicles, often on the scale of <152mm in any dimension, can be remote controlled (RC) or autonomously operated. Developing technologies are aiming to improve maneuverability and stability of such small aircraft. Designs have ranged from small propeller-powered vehicles, rotorcraft, and even flapping-wing designs. The "Mosquito" shown in Figure 1-1 utilizes an 88mm diameter double rotor and has a maximum length of 101mm (www.rchelicopter.com).

Figure 1-1: Mosquito MAV (www.rchelicopter.com)

The DelFly Micro shown in Figure 1-2 exemplifies a flapping wing configuration and weighs only 3 grams with a tip-tip length of 100mm. A small battery allows flight times of three minutes with a maximum speed of 5 m/s while carrying an onboard camera capable of capturing television quality images (http://www.delfly.nl). This MAV provides an excellent example of small size while being able to collect important information during flight for surveillance.
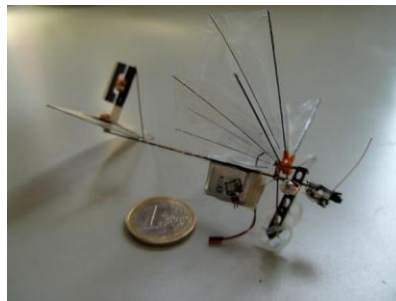
Figure 1-2: DelFly Micro next to Euro Coin (www.delfly.nl)

The flapping configuration of the DelFly mimics a motion found in some of nature's best flyers. Looking at nature for inspiration, the dragonfly exhibits extreme maneuverability and a light-weight design. Maneuverability and light weight are attractive characteristics for small MAV's. Consequently, the dragonfly wings are of

interest for investigation. Their corrugated wing structure provides rigid wings; however, the aerodynamic characteristics of these wings are not yet fully understood.

1.2 Motivation

The motivation for this investigation is to gain a better understanding of flow around corrugated profiles at low Reynolds numbers for static and dynamic cases. While previous experiments have investigated corrugated profiles, little flow visualization data exists directly comparing different biologically inspired corrugated profiles. Comparing multiple corrugated airfoils against a standard smooth airfoil will aid in understanding flow structures generated by each.

Another strong motivation is that few fixtures have been documented which prescribe a motion path similar to that of a dragonfly and allow flow visualization data to be obtained. A fixture allowing dynamic results would be extremely beneficial in providing more representative results of real-life flow structures generated by flapping-corrugated profiles.

1.3 Goals and Objectives

The objective of the current study was to further our understanding of the aerodynamic characteristics of dragonfly wings at low Reynolds numbers. In particular, two areas were selected for investigation: (1) the flow field around corrugated airfoils from low to high angles of attack (here referred to as the static tests); and (2) the flow structure of two-dimensional flapping airfoils (here referred to as the dynamic tests). To conduct the dynamic tests, a fixture needed to be developed which allows Reynolds and Strouhal number to be matched to that of dragonfly flight.

The flow field in both types of studies was investigated experimentally using flow visualization techniques, with different techniques and facilities selected for each type of study. Pertinent background information is provided in Chapter 3 and Chapter 5 describing each experiment apparatus and its development.

1.4 Thesis Overview

This thesis presents research conducted to better understand biologically inspired corrugated airfoils and their aerodynamic performance characteristics compared to a standard airfoil. Chapter 2 introduces important scaling laws used to match flow conditions of dragonfly flight along with information about corrugated airfoils and previous research with varying experimental apparatuses. Chapter 2 also provides additional background information to aid in understanding the direction and contributions of this thesis.

In Chapters 3 and 5, the static and dynamic fixture development is introduced, respectively. In each of these chapters, the reader will find details of specifications, available facilities, facility comparisons, manufacturing, and final experimental setup. The dynamic fixture of Chapter 5 has additional sections regarding control options for each degree of freedom along with motion validation of the complete and mounted fixture.

Results from each fixture follow their respective development chapter. Chapter 4 presents results from the static fixture and Chapter 6 presents dynamic results. Chapter 7 summarizes results obtained and briefly discusses future.

Chapter 2 : Literature Review

2.1 Scaling Laws

Fluid flow research typically involves scaling experiments in order to create comparable flow in a laboratory setting. Scaling the experiment allows dynamically similar flow to be generated in order to replicate flow structures of interest in sizes to accommodate laboratory constraints.

In this investigation, dragonfly flight is of interest and non-dimensional quantities of Reynolds and Strouhal number are used to scale flow characteristics. Reynolds number, shown in Equation 1, is a relationship between inertial and viscous forces in the flow (Batchelor, 2000) and was used for the static and dynamic investigations.

$$Re_c = \frac{Uc}{\nu} \qquad \text{(Eq. 1)}$$

While Reynolds number can be defined in many different ways depending on the representative length selected, chord (c) was used in this investigation. This relates the flow characteristics of velocity (U), fluid kinematic viscosity (ν), and airfoil chord length in order to scale the experiment properly.

Strouhal number relates vortex shedding frequency for oscillating conditions (Batchelor, 2000). In this dynamic investigation, Strouhal number was used along with Reynolds number to create dynamically similar flow in the wind tunnel.

$$St = \frac{fc}{U} \qquad \text{(Eq. 2)}$$

Airfoil chord was also used for the Strouhal number for the representative length, while the shedding frequency is represented by (f).

Reynolds number was specified for this investigation along with Strouhal number in order to match the flight regime of dragonflies. Reynolds number was chosen to be in the range of 1,000 < Re_c < 10,000 which is within the dragonfly flight regime as documented by Wakeling & Ellington (1997). Strouhal number for cruising flight of natural fliers is within a small range of 0.2 < St < 0.4 (Shyy, Lian, Tang, Viieru, & Liu, 2008). With given values for Reynolds and Strouhal number, the remaining parameters were used to create dynamically similar flow for each test case.

2.2 Corrugated Airfoils

Insect flight, such as that of the dragonfly, has been of interest for many years due to the high degree of maneuverability, stability, and light weight structure. Initial observations leave one to think the rough corrugated structure of a dragonfly wing could in no way be aerodynamic; however, their maneuverability motivates further study of this question.

Several models of these corrugated profiles have been proposed. In this study, the profiles selected for investigation were the Kesel Profile 2 (Kesel, 2000) and the Murphy profile (Murphy & Hu, 2009). As a baseline comparison case, the NACA 0012 (Abbott & Von Doenhoff, 1959) was also selected.

These airfoils were selected because the Kesel and Murphy corrugated profiles were commonly used in previous research: Kesel (2000), Murphy & Hu (2009), Kwok & Mittal (2005), and Vargas & Mittal (2004). In addition, these profiles also have specific geometrical differences in their profile shape which can be used to contrast flow structures.

The corrugated shape of dragonfly wings varies depending on the cross section location chosen (Figure 2-1).
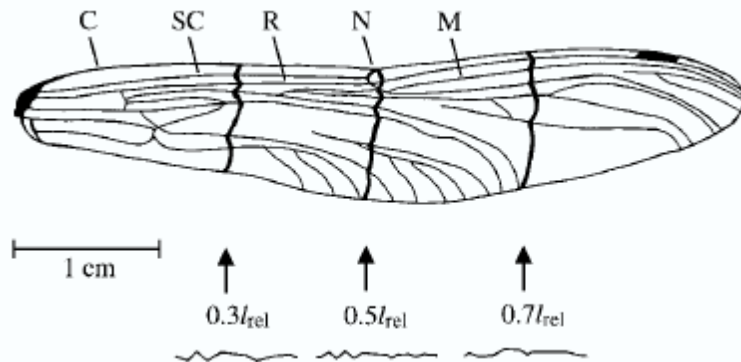
Figure 2-1: Dragonfly Cross Section Locations (Kesel, 2000)

At $0.3l_{rel}$, $0.5l_{rel}$, and $0.7l_{rel}$ in Figure 2-1 you can see the different profile shapes displayed below the wing image. For Kesel's profile airfoil, I chose the mid-span shape, Profile 2, recorded by Kesel and represented in Figure 2-2. Kesel obtained profiles by taking photographs from three positions of a dried Aeshna cyanea dragonfly forewing with a known calibration cube contained in each photograph. Using these images and coordinate transformation software (PICTRAN-D) the wing profile was created (Kesel, 2000). This method was performed at 0.3, 0.5. and 0.7 of the relative span length, l_{rel}, of the wing. Profile 2 was taken at $0.5l_{rel}$ and has been used in many investigations

including Vargas, Mittal, & Dong (2008) and Kwok & Mittal (2005), so it not only provides a biologically inspired corrugated profile to observe the flow field around but also renders itself useful for comparison with other experiments.
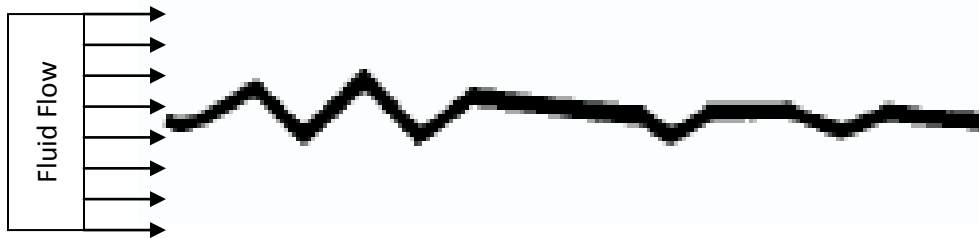
Figure 2-2: Kesel Corrugated Wing Cross Section (Kesel, 2000)

The wing profile identified by Murphy, shown in Figure 2-3, was also selected for comparison of flow structure. This profile closely resembles that of Kesel from the leading edge to 0.6c, with the trailing 0.4c having a different profile, as can be observed by comparing Figure 2-2 and Figure 2-3.

Figure 2-3: Murphy Corrugated Wing Cross Section (Murphy & Hu, 2009)

In Figure 2-2 and Figure 2-3 you can see how the wing appears very rough with peaks and troughs between the leading and trailing edges. These corrugations would seemingly cause poor airflow over the wing; however, previous experimental tests of Vargas, Mittal, & Dong (2008), Kwok & Mittal (2005), Vargas & Mittal (2004), and Kesel (2000) found the wings tend to perform favorably in low Reynolds number flow when compared to typical smooth airfoils due to the increased importance of viscosity at low Reynolds numbers.

This increased importance of viscosity at low Reynolds number can also be expected to negate the geometric differences between the Kesel and Murphy airfoils; however no direct comparisons between the profiles have yet been conducted to confirm this assumption. This investigation aims to document flow structure over these two corrugated foils at the same free-stream conditions to allow comparison between them. In addition, visualizations were also performed of the flow around a NACA 0012 airfoil to determine if the corrugated foils offer any potential aerodynamic improvements over standard airfoil geometries.

2.3 Previous Research on Flow around Dragonfly Wings

Many fixtures have been developed with the goal of recording data of the dynamic motion of a dragonfly wing path. These fixtures typically aim at recording quantitative (lift, drag, moment, particle image velocimetry) or qualitative (parrifin smoke) data. These fixtures can also be classified into two categories: static or dynamic. Static fixtures are held steady during the experiment and typically have only one degree of freedom (pitch) which allows the angle of attack to be changed. On the other hand, dynamic fixtures will move during the experiment. These fixtures may have more than one degree of freedom (pitch and plunge) where a translational displacement is also permitted.

Okamoto, Yasuda, & Azuma (1996) investigated dragonfly wings with three different methods: force/moment measurements, autorotational flight in a vertical wind tunnel, and gliding flights in still air. For the force/moment measurement, the researchers designed three aluminum spars fitted with strain gages to record lift, drag, and moment with a minimum measureable force of 0.0001N in a wind tunnel at Re=11,000-15,000. To attain measurements for this static fixture at angles of attack (α) from -6° to 20°, the wing was swept through angles at a rate of 0.4˚/sec. Each 0.36° increment, the fixture would stop for one second and record ten measurements of aerodynamic force data. Their vertical wind tunnel was designed to have the wing in a free fall state and then measure the wind speed (descent rate), rotational speed, coning angle, and feathering angle. With these values, the aerodynamic characteristics of the 2D wing could be analyzed. In gliding flight, the speed, angle of attack, and gliding angle were measured to characterize the 3D wing. Results for this experiment showed the surface texture and roughness can result in an increase of the maximum lift and maximum lift/drag ratio of the dragonfly wing test models.

Static experiments in a water tow tank were also completed by Sunada, T. Yasuda, K. Yasuda, and Kawachi (2002). Their fixture operated at *Re*= 4000 and recorded lift and drag on various foils via a load cell. Each airfoil was attached to an 8mm diameter circular cylinder which was also submerged under water.
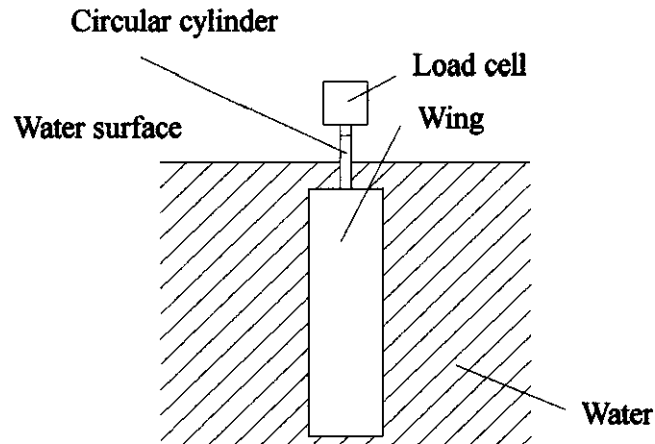
Figure 2-4: Water Tow Tank Fixture (Sunada, et. al., 2002)

Figure 2-4 shows the layout of the fixture with the wing and circular cylinder submerged under water. Effects from the circular cylinder were subtracted by recording the lift and drag generated by the rod alone with no airfoil attached. Interference with the airfoil and side walls was considered negligible since the spacing from airfoil to wall equaled 10 chord lengths. Researchers in this experiment found their greatest error was attributed to angle of attack measurements and signal amplifier noise. Results of this study concluded that proper corrugation can improve the lift to drag ratio when compared to a flat plate (Sunada, Yasuda, Yasuda, & Kawachi, 2002)

Researchers at Virginia Tech have also developed a dynamic fixture which prescribes rapid, truly unsteady, high excursion rate and high Reynolds number maneuvers (Simpson, 2011). The actuation is controlled by three 20.6MPa hydraulic actuators each of which will define plunge, pitch, or roll degrees of freedom. This fixture is termed "DyPPiR" Apparatus (Dynamic Plunge-Pitch- Roll).
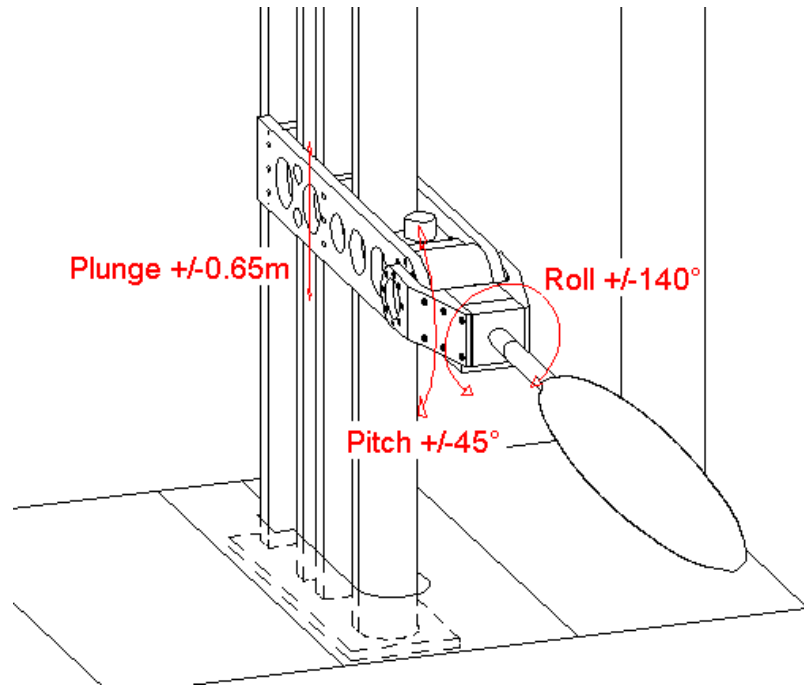
Figure 2-5: Virginia Tech Dynamic Plunge-Pitch-Roll Apparatus (Simpson, 2011)

Figure 2-5 displays the DyPPiR degrees of freedom with a spheroid mounted onto the sting. While this fixture is capable of performing maneuvers at Reynolds numbers of over 4 million, the concept of controlling the plunge, pitch, and roll degrees of freedom was applicable to the fixture required for the current study. Measurements for Virginia Tech's DyPPiR are dominantly time dependant surface pressure and hot film measurements even though force/moment methods have been developed for "submarine" shaped figures (www.aoe.vt.edu/research/facilities/dyppir).

Qualitative flow visualizations over airfoil profiles have also been investigated by Freymuth (1990), Kwok & Mittal (2005), and Murphy & Hu (2009). These investigations provide insight to flow structures generated by different airfoil types which can be used for comparison for qualitative results.

Freymuth produced dynamic flow visualizations of an airfoil with no relative airflow to observe vortices generated by the plunge and pitch motion of a flapping wing. His fixture utilized a 2.54cm chord flat airfoil driven by a direct current (DC) motor with cam-type actuation which can be seen in Figure 2-6. Results from this fixture yielded high thrust coefficients generated by the airfoil in hovering mode utilizing dynamic stall vortices. Time-averaged thrust values were recorded by graphically integrating over squared velocity values gathered with a Pitot-tube from a distance of four chord lengths above the airfoil (Freymuth, 1990). Flow visualization images were also captured of the

9

hovering mode for the flat airfoil. These images shed some light on the vortex generation occurring around the flapping airfoil. Freymuth describes the generation in detail in the referenced article (Freymuth, 1990).

The investigation of Freymuth was different than the objectives of this research in that he was investigating a hover scenario with zero relative flow. The fixture being developed for this thesis aims to pitch and plunge with relative fluid flow. Even so, the Freymuth fixture does provide ideas which could be expanded to control the current fixture for pitch and plunge.
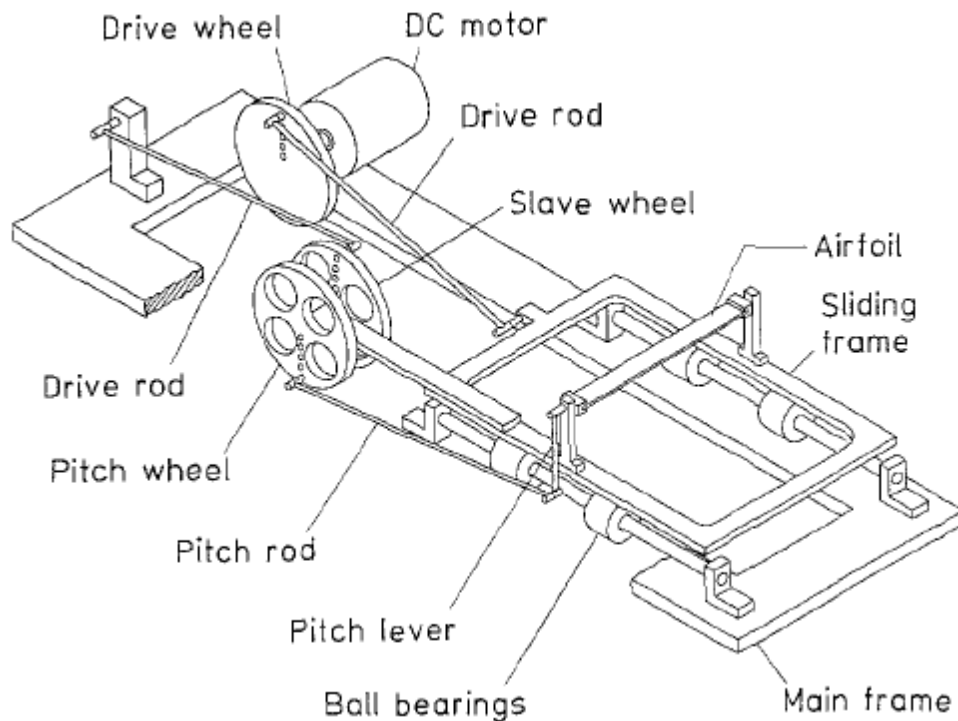
Figure 2-6: Freymuth Hover Mode Apparatus (Freymuth, 1990)

Kwok and Mittal conducted static flow visualization in a water tunnel with a bio inspired corrugated wing profile similar to that utilized by Murphy (Murphy & Hu, 2009) and shown in Figure 2-3. This airfoil was manufactured of 0.2mm thick aluminum with c = 0.2m and l_{rel} = 0.36m. It appears the corrugations were possibly formed around a small diameter cylinder to create the small, smooth radius bends. This is worth taking note of since the boundary of a smooth bend versus a sharp point could affect the flow field in this region by introducing a Reynolds number dependence in the separation behavior. The test model can be seen in Figure 2-7.

Figure 2-7: Corrugated Wing Test Section from Kwok & Mittal (2005)

The Kwok and Mittal water tunnel had a cross section of 0.6096m x 0.3048m. Dye injection was accomplished with an ink/alcohol mixture introduced with a 1.016mm and 1.524mm diameter tube. Velocity in their water tunnel was set at 0.01451m/s yielding $Re_c \approx 2255$.

Kwok and Mittal also gathered quantitative results in a wind tunnel. In the wind tunnel, Kwok & Mittal compared a corrugated model against the same model with transparent tape wrapped around it. The model with tape wrapped around it was termed the "profiled" model. Results from this study show the corrugated model is comparable and even marginally better than its profiled counterpart due to less drag. This observation was supported by flow visualization studies in the water tunnel demonstrating that the flow separates then reattaches to the corrugated profile allowing vortices to be generated in the valleys which resulted in lower skin friction for the corrugated model than the profiled model. This separation and reattachment is one theory behind the corrugated profile's equal or superior performance over profiles airfoils at low Reynolds numbers.

Although many studies have previously been conducted of flapping and corrugated airfoil sections, most of the experiments were completed under flow scenarios different from those selected for the current investigation. The fixture of Virginia Tech is dynamic and operated at Reynolds numbers much higher than the $Re_c < 10,000$ desired for scaling dragonfly flow characteristics.

Kwok & Mittal's static experiment in the water tunnel was similar to the investigation of this thesis but only observed the Murphy corrugated profile. An extension to this under the current investigation is to also compare the Kesel Profile 2 and a standard NACA streamline airfoil at a $Re_c = 1,000$. Their investigation considered conditions leading to $Re_c = 2255$. Kwok & Mittal's wind tunnel experiments were conducted by recording lift and drag measurements in a quasi-static case. Measurements were taken while the airfoil was changing angle of attack very slowly as to not disturb the flow, so not truly dynamic which is a goal of the current investigation. The Reynolds number in their experiment was 31,200 due to wind tunnel limitations.

11

Freymuth's dynamic fixture provides similar pitch and plunge characteristics as the dynamic fixture developed for this investigation but the flow scenario is different. Freymuth collected data in a free air case where there was no relative flow over the airfoil. His investigation was interested in the flow structures created only from the plunge and pitch motion with no forward movement. Similar motion will be prescribed in this investigation, but with relative air flow over the airfoil to match the Reynolds and Strouhal number of dragonfly flight.

Chapter 3 : Static Fixture Development

3.1 Specifications

Static airfoil flow visualizations were performed first to gain understanding of flow structure around the corrugated profiles under a steady flow, non-flapping case and to compare the dependence on the corrugated profile used. This investigation replicated gliding flight with no plunging of the airfoil and matched parameters of Reynolds number and angle of attack of research conducted by Hord & Lian (2011) at the University of Louisville.

The NACA 0012, Kesel, and Murphy foils were used for comparison in the static case. With the NACA 0012 being a typical profiled airfoil, it will serve as the baseline for comparison against the corrugated foils. Research conducted by Lian & Hord (2011) investigated angles of attack between 0°-40°. A few of these angles (0°,8°,16°,28°, & 40°) were matched allowing experimental results to be compared with numerical computational fluid dynamics (CFD) simulation of Hord & Lian, (2011). These angles of attack provided enough information for comparison with generated CFD results.

Reynolds number was the driving scaling parameter for the static case. The Reynolds number, as defined by Equation 1, was chosen with respect to chord length of the airfoil. A Reynolds number of 1000, which is in the region for dragonflies and used in the research of Hord & Lian (2011), was specified to be observed for two corrugated profiles: Kesel Profile 2 and Murphy along with a standard NACA 0012 profile. Which device was selected for the fixture determined the possible Reynolds number range for the experiment.

For dynamic testing, the spacing from the test airfoil to the tunnel wall boundaries is desired to be 10 chords in the plunge direction to minimize wall effects. Under the static investigation this specification was relaxed since the flow is not highly unsteady, but had to be considered when choosing airfoil size to avoid effects from the boundaries.

Capturing images of the flow was the main deliverable of the visualization, therefore, this was the primary consideration when developing the fixture and choosing an experimental fluids device to house the fixture. Since the objective of the static case was to perform qualitative visualization of flow structure, no consideration was given during development to recording loads now or in the future with the fixture.

3.2 Available Facilities

Located at the University of Kentucky are three experimental devices that could be utilized for the current study: wind tunnel, water tunnel, and tow tank. The sizes of each device are different which defines their capabilities for the desired experiment. Specifics for each device and an image are listed below:

i. Engineering Laboratory Designs 406 (B) Wind Tunnel
    a. Cross Section: 61cm x 61cm
    b. Fluid Speed: 3-45.7 m/s

Figure 3-1: ELD Wind Tunnel

The ELD Wind Tunnel shown in Figure 3-1 is an open circuit tunnel and has the largest cross section of the three devices. Clear panels can be installed on each boundary of the test section allowing viewing from any angle. The length of the test section is also suitable to observe a large distance downstream from the specimen. Since the fluid can be continually moved, the test duration for experiments is infinite.

ii. Engineering Laboratory Designs 501 Water Tunnel
    a. Cross Section: 15.24cm x 15.24cm
    b. Fluid Speed: 0.03-0.30 m/s

Figure 3-2: ELD Water Tunnel
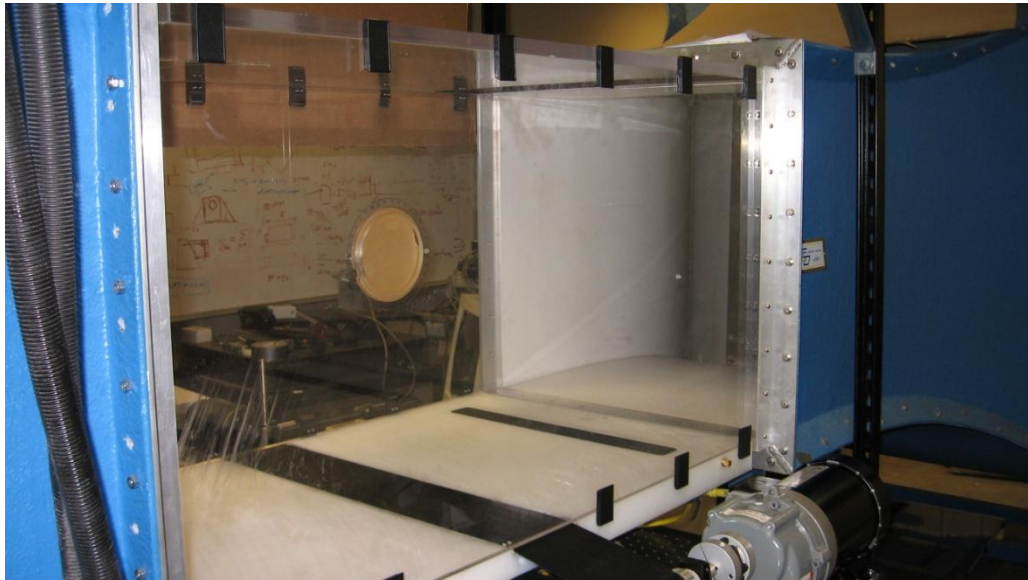
The ELD Water Tunnel shown in Figure 3-2 is a closed circuit tunnel and has the smallest cross section of the three devices. As with the wind tunnel, the test duration is infinite and clear panels surround the test section.

    iii.   University of Kentucky Tow Tank
        a. Cross Section: 38.1cm x 30.5cm
        b. Fluid Speed: Variable with gearing

Figure 3-3: Tow Tank

Unlike the other fixtures, the tow tank shown in Figure 3-3 has a finite test duration. Testing in this device would require the specimen to accelerate from rest up to the desired velocity, maintain the desired velocity for a certain distance, and then decelerate before reaching the end of the tank. The specimen is viewable from any angle except from above where views are obstructed by the frame supporting the panels. Translation is controlled by an external DC motor with a pulley system connected to a trolley. Plunge displacement might be difficult to achieve with this device.

3.3 Facility Comparison

Choosing the best suited device was a process of evaluating the Reynolds number capable of being produced by the published specifications while meeting the desired spacing requirements. Striving for the maximum chord was desirable because it would be easier to manufacture the corrugated airfoil and provide more distinct flow visualization.

First, the minimum and maximum Reynolds number is calculated for each fixture with the appropriate maximum chord length previously determined and manufacturer's stated fluid speed limits. Fluid speed values presented for the tow tank were gathered by averaging three times taken for the tow tank trolley to travel a distance of 1.0m with a stopwatch at a low and high motor angular velocity. Raw data is presented in

Table 3:1: Static Fixture Facility Parameter Study

Fixture	Kinematic Viscosity (m^2/s)	Speed Range (m/s)	Re Range
Wind Tunnel	1.57E-05	3.0-45.7	5500-84600
Water Tunnel	1.52E-06	0.03-0.3	150-1400
Tow Tank	1.52E-06	0.1-0.7	1200-8000

Upon initial investigation, the wind and water tunnels are both capable of producing a Reynolds number below 10,000 with the water tunnel being much lower and closer to 1,000. Additionally, the tow tank is capable with proper gearing. The size of the wind tunnel permits the largest chord of the three fixtures but additional efforts were necessary to know whether the wind tunnel would satisfy our Reynolds number criteria. To validate the manufacturer's specifications, the fluid speed was measured in

the wind tunnel to obtain the lowest velocity produced. This was completed with a manometer and Omega PX653 pressure transducer shown in Figure 3-4.

A Pitot-static tube was placed into the wind tunnel to record the pressure difference between static and total pressure. This difference was recorded by the aforementioned pressure transducer while also generating a fluid displacement in an inclined manometer for reference. To record the pressure differential with the transducer and manometer, the static pressure tube and total pressure tube each contained a "T" joint allowing the transducer and manometer to be used at the same time. A schematic for the setup is displayed in Figure 3-4. Each component is labeled with tubing displayed with orange lines.

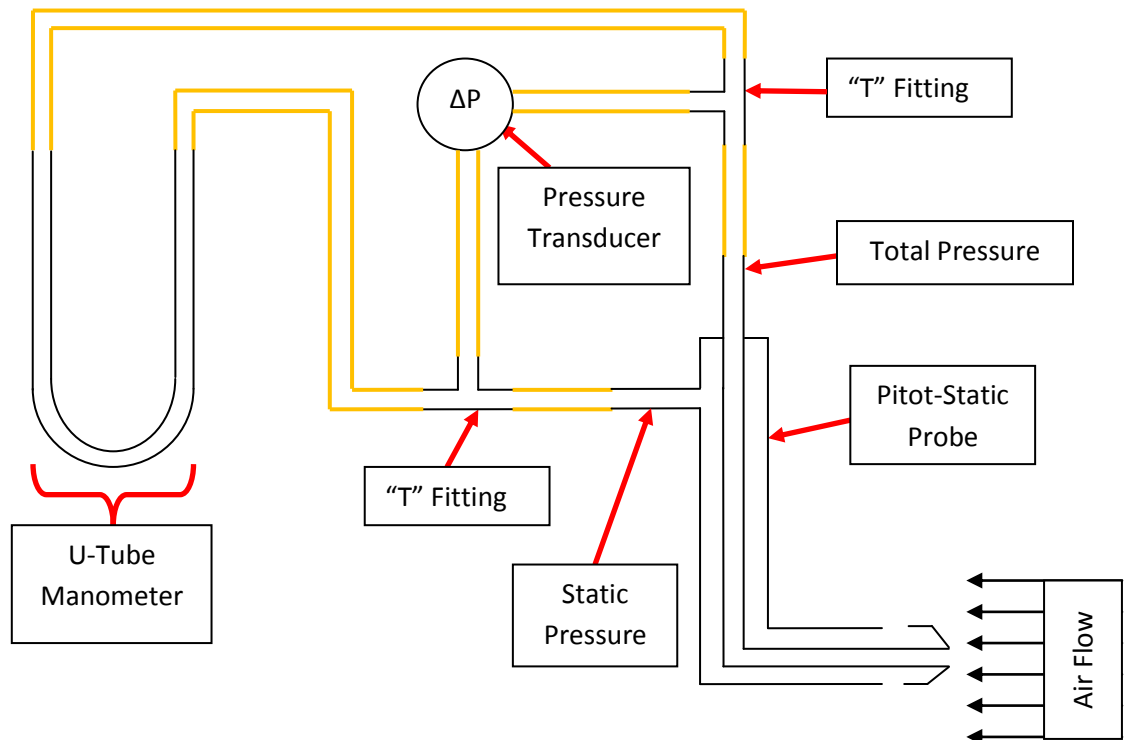Figure 3-4: Wind Tunnel Velocity Experimental Setup

During the experiment, the frequency of the motor controller was swept from 0-6Hz. At each desired frequency the transducer voltage was collected. Correlating transducer voltage to inH_2O was completed first by creating a plot of the pressure transducer manufacturer's calibration curve of voltage against fluid displacement which is shown in Figure 3-5.
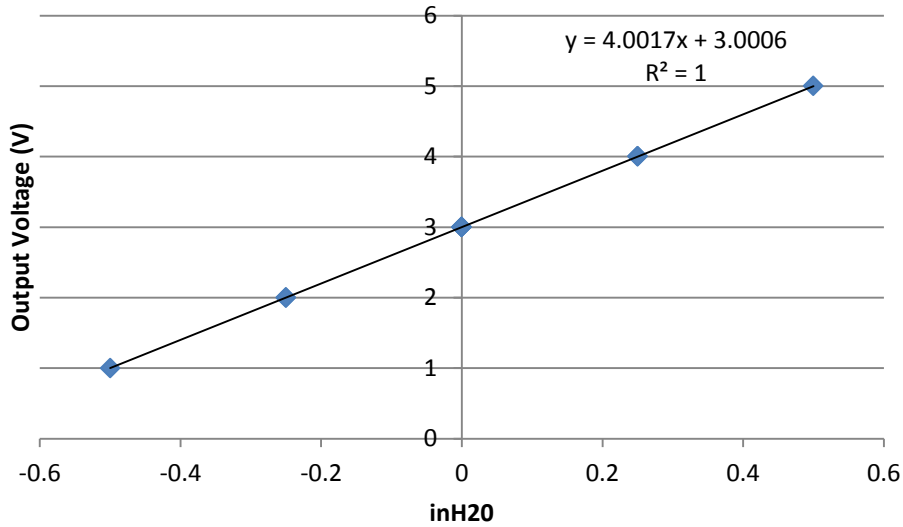
Figure 3-5: Pressure Transducer Calibration Curve

The calibration curve in Figure 3-5 yields a linear relationship between output voltage and inches of displaced water from the manufacturer of the pressure transducer. A linear trendline was determined for the data and the equation was included in the plot. The equation was rearranged to solve for inH_2O in Equation 3 with V= output voltage.

$$inH_2O = \frac{V - 3.006}{4.0017} \qquad \text{(Eq. 3)}$$

This relationship was then used to relate the output voltage obtained during the frequency sweep to the correlating displacement of H_2O. After applying Equation 3 to determine inches of displaced water, negative values were found for low voltages. This indicated the pressure transducer had crept from the manufacturer's value at $0inH_2O$ which was found to be 3.006V from Equation 3. To accommodate this creep, the recorded output voltages for 0Hz, which represents $0inH_2O$, were averaged and used to determine the inches of displaced water. This shifted the 0Hz output voltage from 3.006V to 2.985V. Table 3:2 includes data calculated using the updated offset.

Table 3:2: Wind Tunnel Raw Data

Hz	Output V	inH20	Pa	Velocity (m/s)
0	2.98	-0.001	-0.311	#NUM!
1	2.989	0.001	0.249	0.644
2	2.995	0.002	0.622	1.018
3	3.006	0.005	1.307	1.476
4	3.035	0.012	3.111	2.277
5	3.101	0.029	7.218	3.468
6	3.17	0.046	11.511	4.380
5	3.101	0.029	7.218	3.468
4	3.035	0.012	3.111	2.277
3	3.006	0.005	1.307	1.476
2	2.995	0.002	0.622	1.018
1	2.99	0.001	0.311	0.720
0	2.989	0.001	0.249	0.644

With the displacement completed in inH_2O, the values were converted into Pascals using the relationship in Equation 4.

$$1 inH_2O = 249 Pa$$ (Eq. 4)

With the displacement converted into pressure, the pressure differential was applied to Bernoulli's equation in Equation 5 and converted into velocity with P_t= total pressure, P_s= static pressure, and ρ= density.

$$U = \sqrt{\frac{2(P_t - P_s)}{\rho}}$$ (Eq. 5)

This conversion then allowed a plot to be generated relating motor frequency to fluid velocity. This relationship was used to alter the tunnel fluid speed in order to match Reynolds number for each experiment. Figure 3-6 established that velocities below 1.0 m/s were attainable with the wind tunnel.
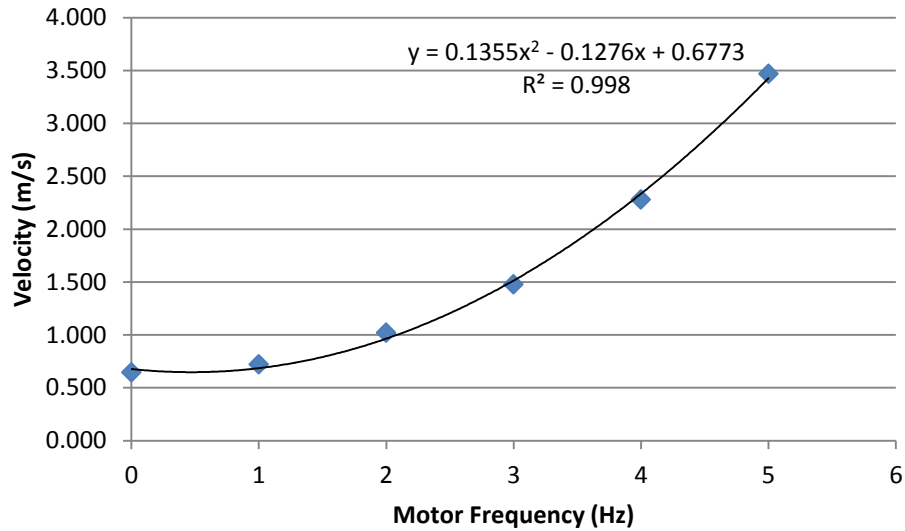
Figure 3-6: Velocity vs. Motor Frequency

The quadratic trendline equation was taken from Figure 3-6 and used to solve for motor frequency in Equation 6 where U=velocity using the quadratic formula which can be found in most mathematical textbooks.

$$0 = 0.1355 f_m{}^2 - 0.1276 f_m + 0.6773 - U \qquad \text{(Eq. 6)}$$

Raw data can be found in the appendix, but this data depicts a speed as low as 1.0 m/s can be obtained in the wind tunnel. Applying this speed to Equation 1 with c = 2.54cm yields a lower Reynolds number of 1850 that can be produced by the wind tunnel.

With each device capable of satisfying our specifications, more investigation and fixture operation was considered in order to choose the proper device. At this point, each device was visited and evaluated for benefits and drawbacks.

3.3.1 Wind Tunnel

The wind tunnel provides the largest test section of the three fixtures and is capable of fluid speed down to approximately 1.0 m/s. Capability to house a large chord is attractive since the wing model could be scaled up to allow easier flow visualization of vortices expected to be generated in the valleys of the model. However, the minimum speed of 1.0 m/s generates a higher Reynolds number than desired.

20

3.3.2 Water Tunnel

The water tunnel has the smallest cross section of the three devices but is properly equipped with a protractor to record angle of attack (α) while investigating static flow. A method to inject dye would need to be added for flow visualization.

Creating the corrugated profiles for the water tunnel has the advantage of being smaller and easier to produce with rapid prototyping methods which are often limited in size.

Allowing for a static test section and infinite test duration is attractive which allows as much data as desired to be collected without resetting the fixture.

3.3.3 Tow Tank

Operation of the tow tank requires the test model to traverse a finite distance and be reset for each test setup. Since the fixture would accelerate to a constant speed then decelerate before reaching the end of the tank, only a finite region exists to collect the proper data. Collecting the data could also pose an issue since the collection equipment would also be required to traverse with the test section to collect data which would be considered static.

After evaluating each device, the water tunnel was chosen since it was already properly equipped to record the static angle of attack and could match the desired Reynolds number. Size of the water tunnel also yields the test sections appropriately sized for production via rapid prototyping methods (stereolithography, 3D printing, etc.) which is highly beneficial given the complicated structure of the corrugated profiles.

3.4 Fixture Manufacturing

The ELD Water Tunnel at the University of Kentucky was chosen to observe streak lines and vortices generated by the corrugated airfoils at various angles of attack. This device was chosen since it could match Re=1,000 and was already marked to track the angle of attack of the mounted specimen from 0°-360°. Test models of both corrugated profiles and a method to inject dye upstream of the specimen were required to complete the static flow visualization setup.

Visualization of the streak lines is aided with a larger chord length in the water tunnel. A larger model scales the corrugations up allowing for the vortices and flow structure to be observed more easily. The largest chord allowable is 50.5mm due to the hole size where the airfoil is inserted in the side wall of the water tunnel, so this chord length was chosen.

A 3D model was sketched in Pro-Engineer solid modeling software by tracing the profile trajectory of both the Kesel and Murphy foils with a thickness of 1.58mm. These models were then created by the University of Louisville's Rapid Prototyping Center with a Dimension 3D printer and ABS substrate. Figure 3-7 compares the physical test section with that of the printed profiles. Printed profiles are above with physical test sections below while Kesel is farther left and Murphy right. Thickness-to-chord appears to distort the comparison slightly but the profile trajectory is the main concern since the thickness has been set to 1.58mm. Following the profile, the physical and printed match very well at respective peaks and valleys.

Figure 3-7: ABS Airfoil Comparison Kesel (2000) left, and Murphy (2009) right

The 3D printed models initially had some rough edges with respect to the peak/valley sizes of the wing and blunt peaks which were a concern for altering the flow structure. Figure 3-8 below indicates one section which was considered rough, and an example of blunt peaks can be seen as well in the green square.
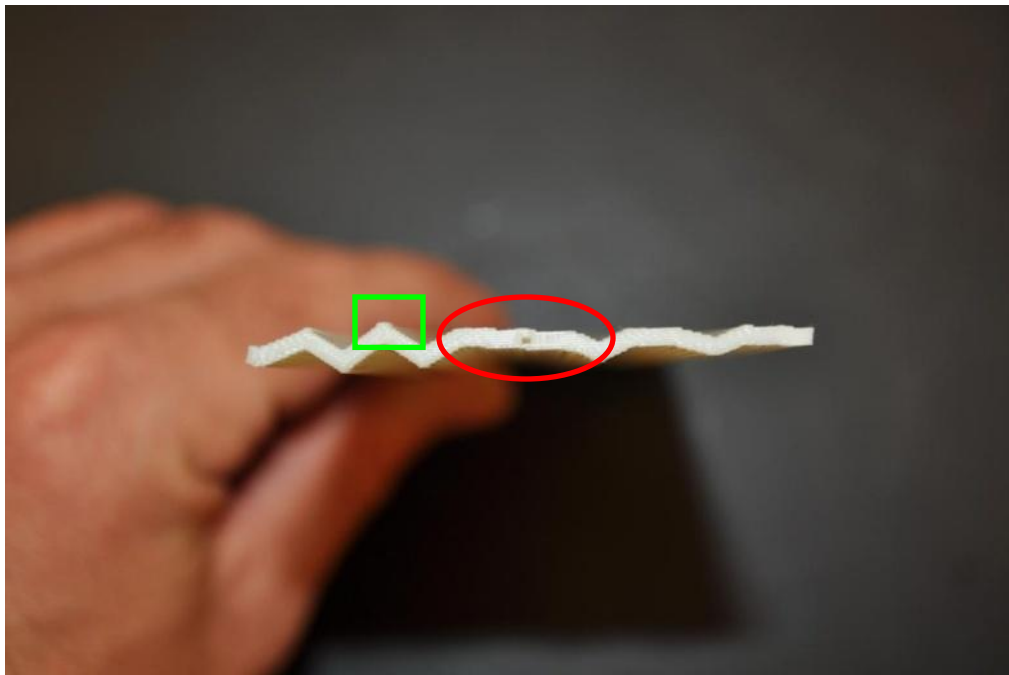

Figure 3-8: Kesel Rough ABS Corrugated Airfoil

The easiest rough section to see is depicted on the Kesel airfoil in Figure 3-8 from 1/3c to 2/3c of the airfoil and identified with the red circle. Instead of a smooth section, the method of depositing the plastic creates a stair-stepped effect. This was expected since the 3D printing method used deposits of a 0.25mm layer thickness with each pass and the airfoil was created from the bottom upward.

To smooth out the airfoil, a square point hobby knife was used to file down the stair stepped edges and create sharper peaks and valleys. The modified Kesel airfoil had the shape in Figure 3-9 below, mounted in the water tunnel.
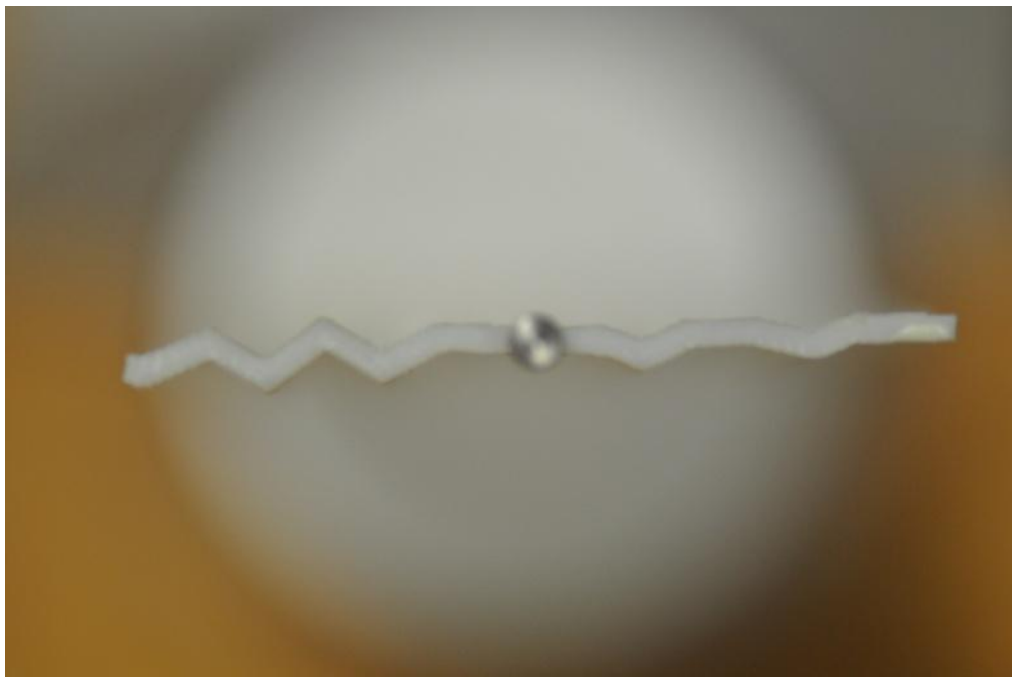

Figure 3-9: Kesel Smoothed ABS Corrugated Airfoil

Comparing the region from 1/3c to 2/3c, you can see how the region has been smoothed and the peaks and valleys are more defined in the other areas. The Murphy airfoil was smoothed in the identical manner as Kesel.

With the airfoil reshaped, it was then attached to a plug sized to fit the 50.5mm hole in the water tunnel wall. This plug was slightly undersized from 50.5mm and fitted with a rubber O-ring to seal water from exiting the water tunnel. On the plug side, the airfoil was pinned with two 0.79mm diameter steel dowel pins for constraint with the opposite end also pinned with a 0.79mm pin expanded to 3.15mm and shown in the Appendix. The 3.15mm section inserts into pre-existing mounting holes in the wall of the

water tunnel constraining the tip from translating while allowing rotation for varying the angle of attack.

Figure 3-10 displays a completed water tunnel test model. The wall plug is located on the left end of the wing and has the black rubber O-ring attached. The left end also has two locating pins attaching the wing to the plug but they cannot be seen since they are inserted both inside the wing and plug. The end pin protrudes from the right end of the wing at mid chord. Notice the face of the end plug where the wing is attached is painted white. This was done to provide a good background for streaklines and vortices during flow visualization. Engineering drawings of the end pin and wall plug are provided in the Appendix.
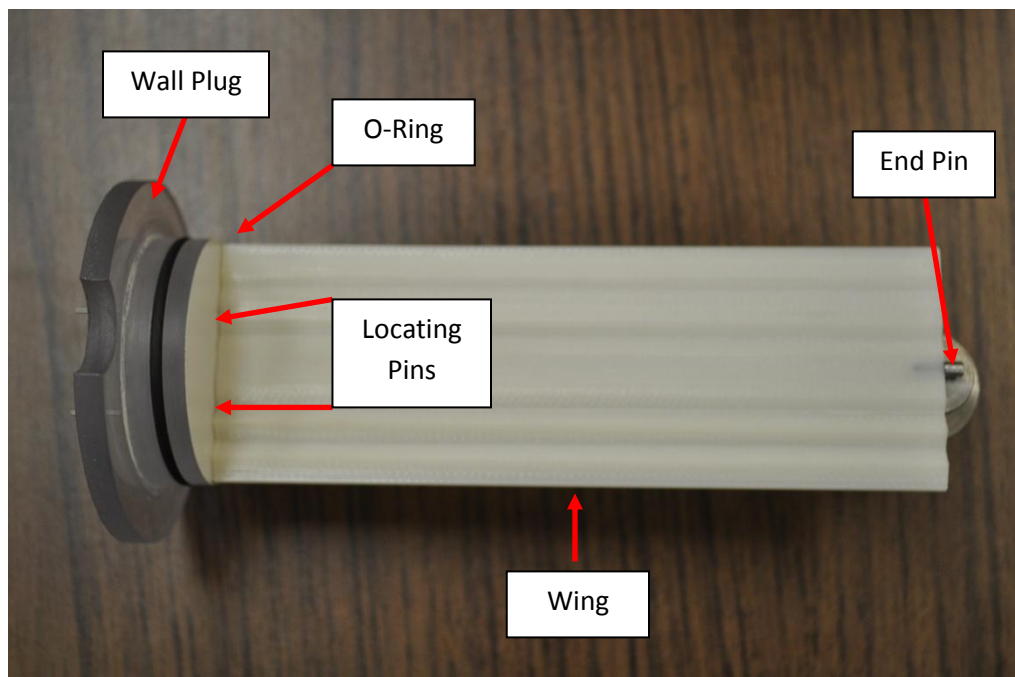

Figure 3-10: Water Tunnel Corrugated Test Section

3.5 Experimental Setup

Once the test section was completed, it was then inserted into the water tunnel for flow visualization. Food coloring was diluted with water at a ratio of 1 drop of food coloring per 10cc water to create the dye. The dye delivery system consisted of a small 0.5mm inner diameter stainless steel tube gravity fed from a container filled with dye. The injection depth of the tube was adjustable with a lead screw so it could be placed at the airfoil leading edge height for each angle of attack. The flow rate was controlled with a needle valve in the feed line. Figure 3-11 below displays the flow visualization setup with the dye injection reservoir mounted with blue dye. Behind the reservoir is the lead screw controlling depth. You can also see the corrugated airfoil mounted in the test section area and rotated to a high angle of attack. Work lights mounted above the tunnel are used to provide ample lighting for capturing flow visualization images.
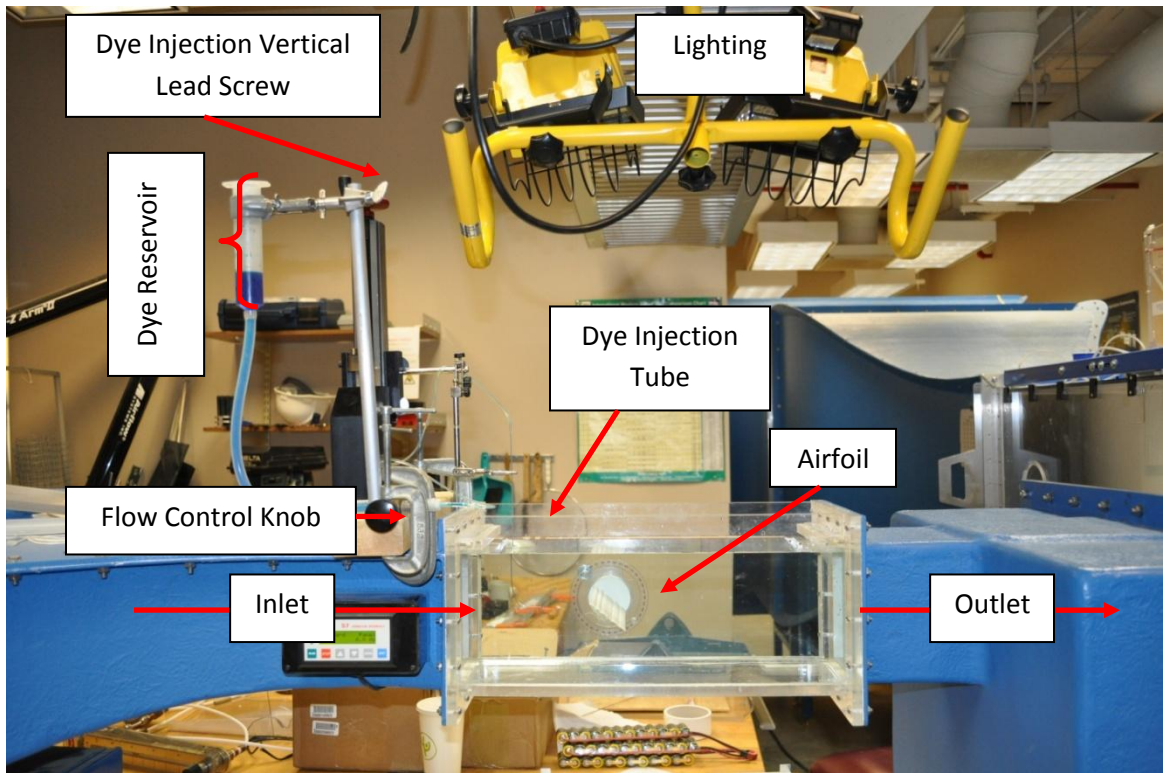

Figure 3-11: Dye Injection Setup

Of interest for the corrugated profiles was the generation of vortices in the valleys of the foils. To investigate the vortices more closely, dye of a different color was introduced manually into the valleys of the corrugated profiles with a syringe and

stainless steel probe shown in Figure 3-12 below. Care was taken to inject the dye slowly in order to minimize turbulence creation at the injection site.
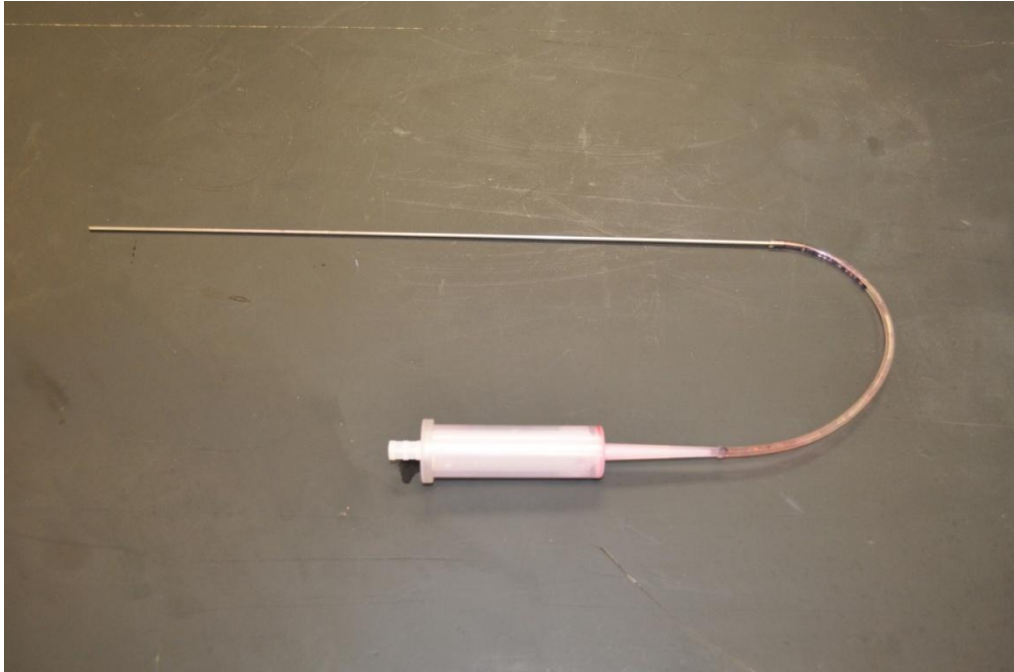

Figure 3-12: Manual Dye Injection Syringe

A Nikon D5000 digital single-lens reflex camera with a 105mm Nikon Micro-Nikkor Macro lens was used to capture static flow visualization images. Using the macro lens allowed the dye streaklines to be focused very clearly. The disadvantage is that the macro lens has a very shallow depth of field which causes the near-end of the airfoil to become blurry in the images while the streaklines are very clear. With a maximum aperture value of f/2.8, the macro lens allowed ample light in to expose the static images clearly. Even with a low f value, it is important to provide ample lighting in the region of interest to improve the image quality.

Chapter 4 : Static Flow Visualization Results

4.1 Top & Stagnation Streaklines

Streaklines were observed by lowering the dye injection tube to the appropriate height at each angle of attack. Six injection points were selected at each angle of attack for each of the foils. They will be treated as: Top Streakline, Stagnation Point Streakline, Vortex #1, Vortex #2, Vortex #3, and Vortex #4. For the standard NACA airfoil, vortex injection points were not observed on the airfoil since they are not present. The Top and Stagnation Point Streaklines were observed by manually traversing the dye injection tube vertically until the dye streak was just above the stagnation point for the top streakline and at the stagnation point for the stagnation streakline. For all vortex cases, the Top Streakline was maintained while injecting an alternate color dye into the corresponding valley of the wing.

Figure 4-1 below represents identification of the injection location as well as top and bottom streaklines. The stagnation point streakline consisted of the top and bottom streaklines simultaneously.
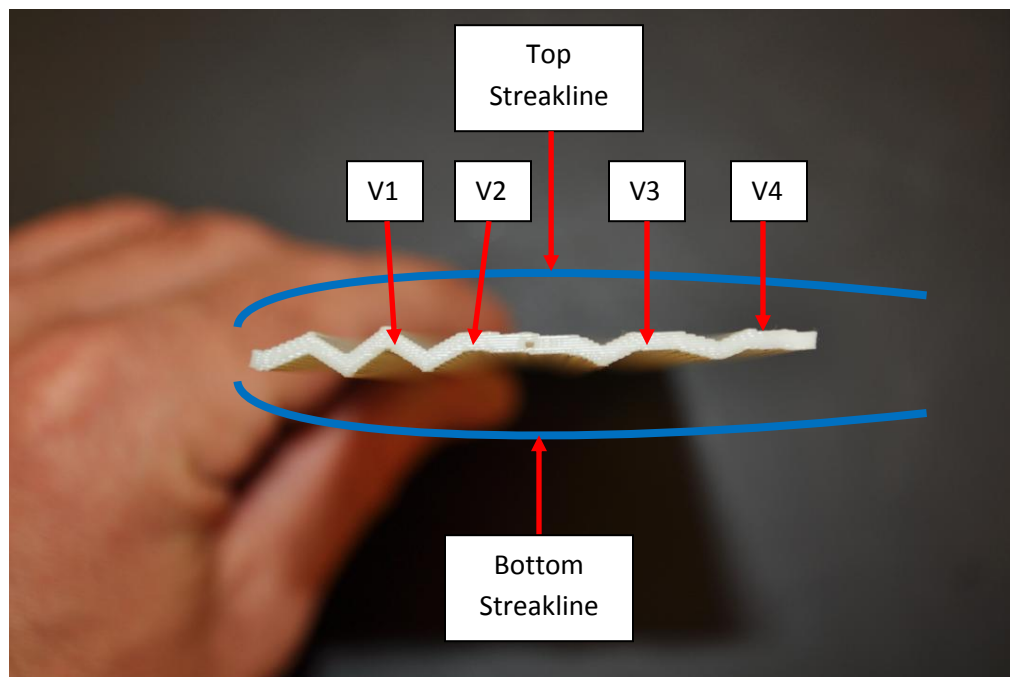

Figure 4-1: Flow Structure Naming Convention

All static flow visualization images were captured at Re_c=1,000, U = 0.03m/s, and the airfoil profiles submerged in water with diluted food coloring dye injected upstream.

The reference scale displayed against the airfoil is divided into $c/16$ increments and will be used for quantitative comparisons of each airfoil. The scale is also centered on the support pin at mid-chord in each image and not rotated to correspond with α, but rather remains vertical. Each image also contains a red line which corresponds to the chord line of each airfoil.

Figure 4-2 displays the airfoils at 0 degrees with the top (left) and stagnation (right) streaklines being introduced for the NACA 0012 (a,b), Murphy (c,d), and Kesel (e,f) models. In this case the streaklines hold close to the airfoil surface and do not separate along the airfoil.

a.   b.

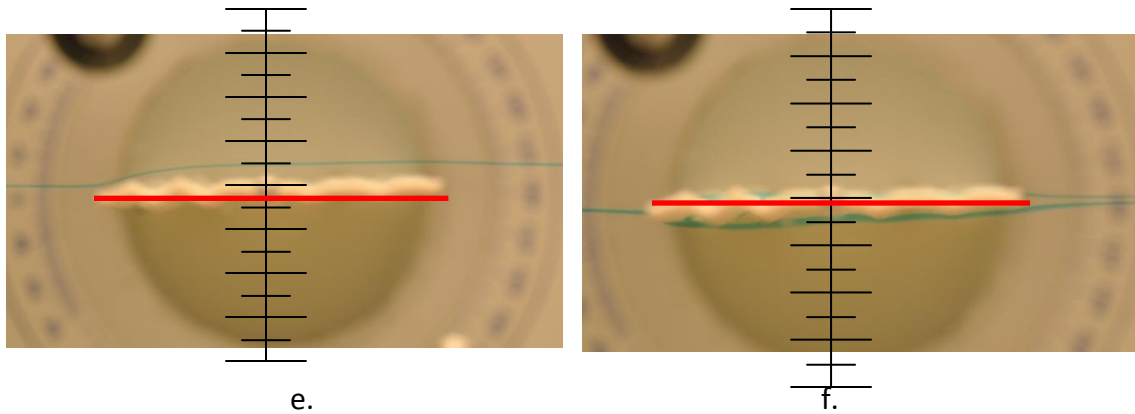c.   d.
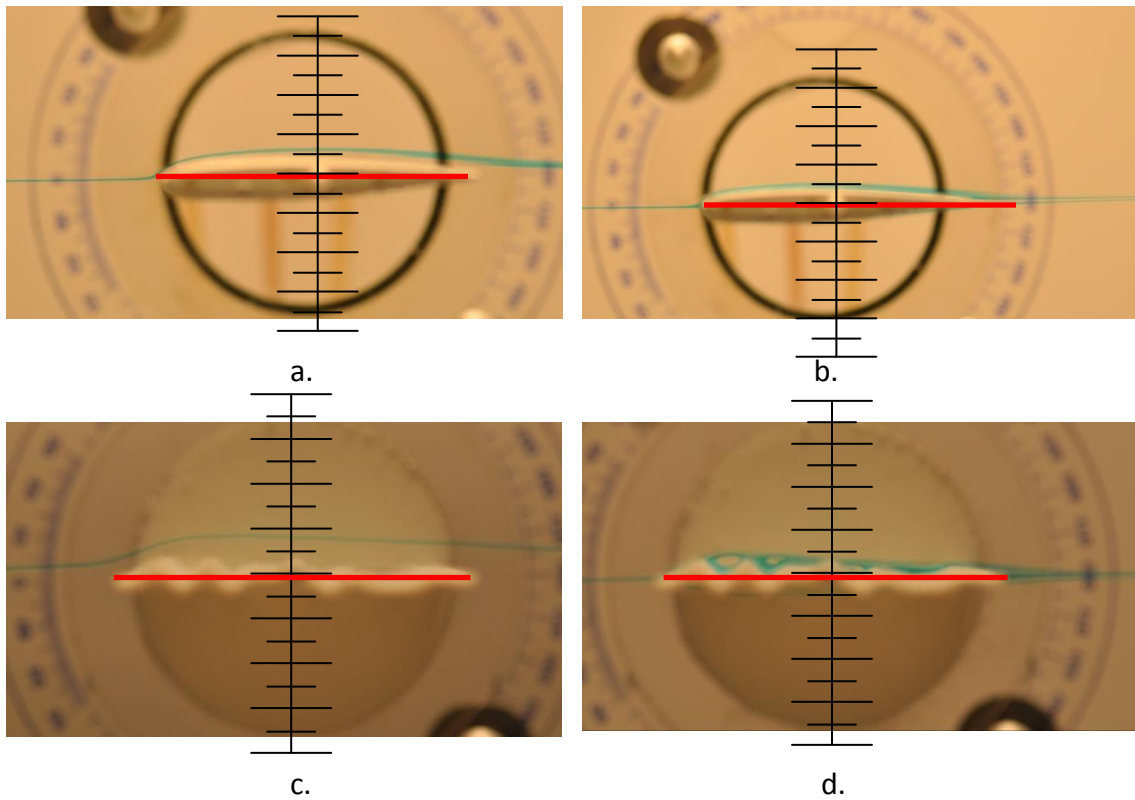
Figure 4-2: 0 degrees AoA Top (left) and Stagnation (right) Streaklines for NACA 0012, Murphy, and Kesel

Figure 4-2.a represents the NACA airfoil in which the top streakline follows the surface closely from the leading to trailing edge. Figure 4-2.c and Figure 4-2.e show the Murphy and Kesel airfoil top streaklines respectively. Even with the corrugated profile, the top streakline appears smooth as it passes over the airfoil surface. Just observing the streaklines, it can be noticed that the shape over the corrugated profiles resembles that generated by the smooth NACA airfoil. This behavior was expected as the streaklines pass over the corrugations and was also documented by Vargas & Mittal (2004). While the top streakline provided a visual aid of flow around the airfoil, the stagnation streaklines were more consistent for replicating the dye injection location for each airfoil. With that fact, all quantitative comparisons are completed with measurements taken from the stagnation streakline images.

Lowering the injection tube slightly allows the stagnation streakline to be generated and shown in the right image column of Figure 4-2. The stagnation streakline initiates at the stagnation point and proceeds around the wing before joining back together slightly behind the trailing edge of the foils. This case shows the attached flow on top and bottom surfaces. The streakline on the bottom side of the airfoil was anticipated to be identical to the top at 0 degrees for the NACA 0012 airfoil since it is symmetric along the chord with no camber. Maximum thickness between streaklines in this orientation for the NACA 0012 is approximately $0.13c$ which is nearly identical to the 12% maximum thickness of the airfoil identified from the NACA nomenclature. Distance from the chord line to the top streakline is $.06c$.

Figure 4-2.d represents the Murphy profile with a maximum distance of $0.06c$ from the chord line to the top streakline compared to less than $0.06c$ for the Kesel profile of Figure 4-2.f. Both distances occur at the first peak encountered by the flow at

the leading edge while both corrugated profiles traverse smoothly over the length of the airfoil. Another observation was the blue streakline profiles being asymmetric over the corrugated profiles while the NACA 0012 remained symmetric.

Stagnation streaklines also represent the vortex formation in valleys of the corrugated airfoils very well. The Murphy (d) case is a good representative and shows distinct vortices developed in the valleys of the profile. The Kesel profile (f) in this case does not represent the profile as clearly as Murphy due to most of the dye passing along the bottom of the airfoil. Here, the Murphy profile generates a maximum thickness of slightly more than $0.13c$ located at vortex #1 ($0.19c$) in conjunction with the labeling convention introduced in Figure 4-1 earlier while the Kesel profile generates a thickness of $0.13c$ located at the same location as Murphy.

The angle of attack was increased to 8° for each airfoil in Figure 4-3 with the top and stagnation streaklines represented as they were for 0°.
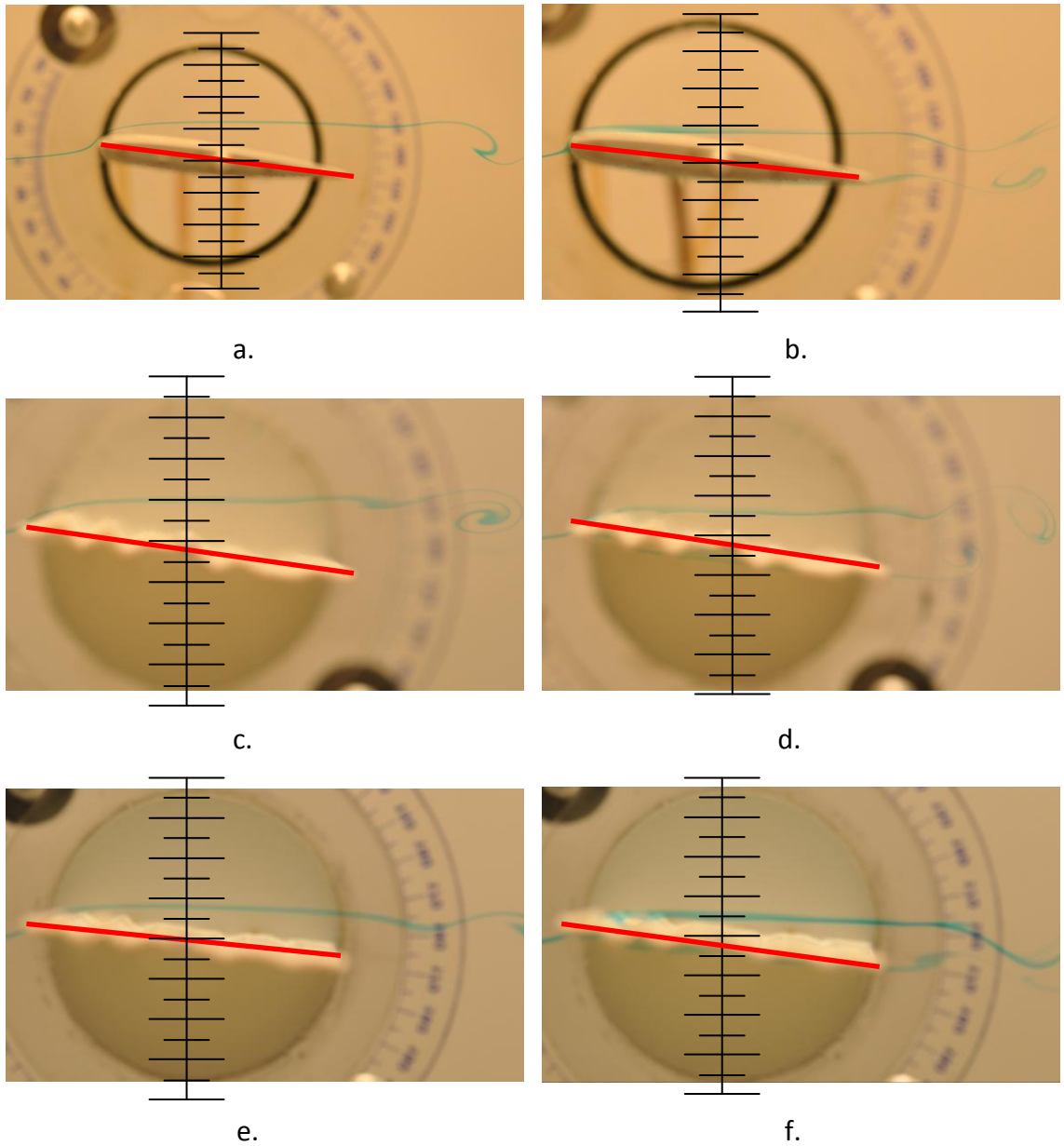
Figure 4-3: 8 degrees AoA Top (left) and Stagnation (right) Streaklines for NACA 0012, Murphy, and Kesel

At α=8°, the top streakline flows smoothly over each airfoil as was the case for 0°. Shed vortices from the top streaklines can also be seen downstream of the trailing edge at approximately 0.5c for the NACA 0012 and Kesel, while the Murphy airfoil was 0.44c. The Murphy airfoil has the best representation of a shed vortex with the image capturing interior detail of the vortex. The NACA and Kesel profiles have the shed vortex but only capture the exterior of the shape. Even though the level of detail differs for each airfoil, the vortex size can be used for comparison in flow structure. The vortex

generated by the NACA and Kesel foils had a diameter of 0.06c with the Murphy profile generating a larger diameter of 0.13c.

Stagnation streaklines at α=8° are shown in the right column of Figure 4-3. Separation from the top surface initiated at 0.5c for the NACA 0012 and Kesel profiles while the Murphy profile separated earlier at 0.13c. Separation occurred on the top while the bottom remained attached to the airfoil surface for each profile. Separation distance from each airfoil was measured at the trailing edge for each angle of attack. Maximum separation distance between streaklines for the NACA 0012 is just over 0.13c. The Murphy and Kesel profiles had separation distances of 0.19c and 0.13c respectively. Separation for the Murphy profile in Figure 4-3.d appears to be much larger than the NACA 0012 or Kesel profile partly due to a vortex beginning to form and rolling the top streakline upward just before the trailing edge. Separation from each airfoil increased from the α=0° case in which no separation was generation by either airfoil.

Rotating the airfoil α=16° phase generates the flow represented in Figure 4-4 below. Here, the top streakline is shown in the left column with stagnation streaklines displayed on the right. At α=8°, the flow had separated from each airfoil. Increasing the angle of attack resulted in similar flow structure with increasing separation distance and vortex diameter. Observing the streaklines in Figure 4-4 you can see similarities in the flow structure.
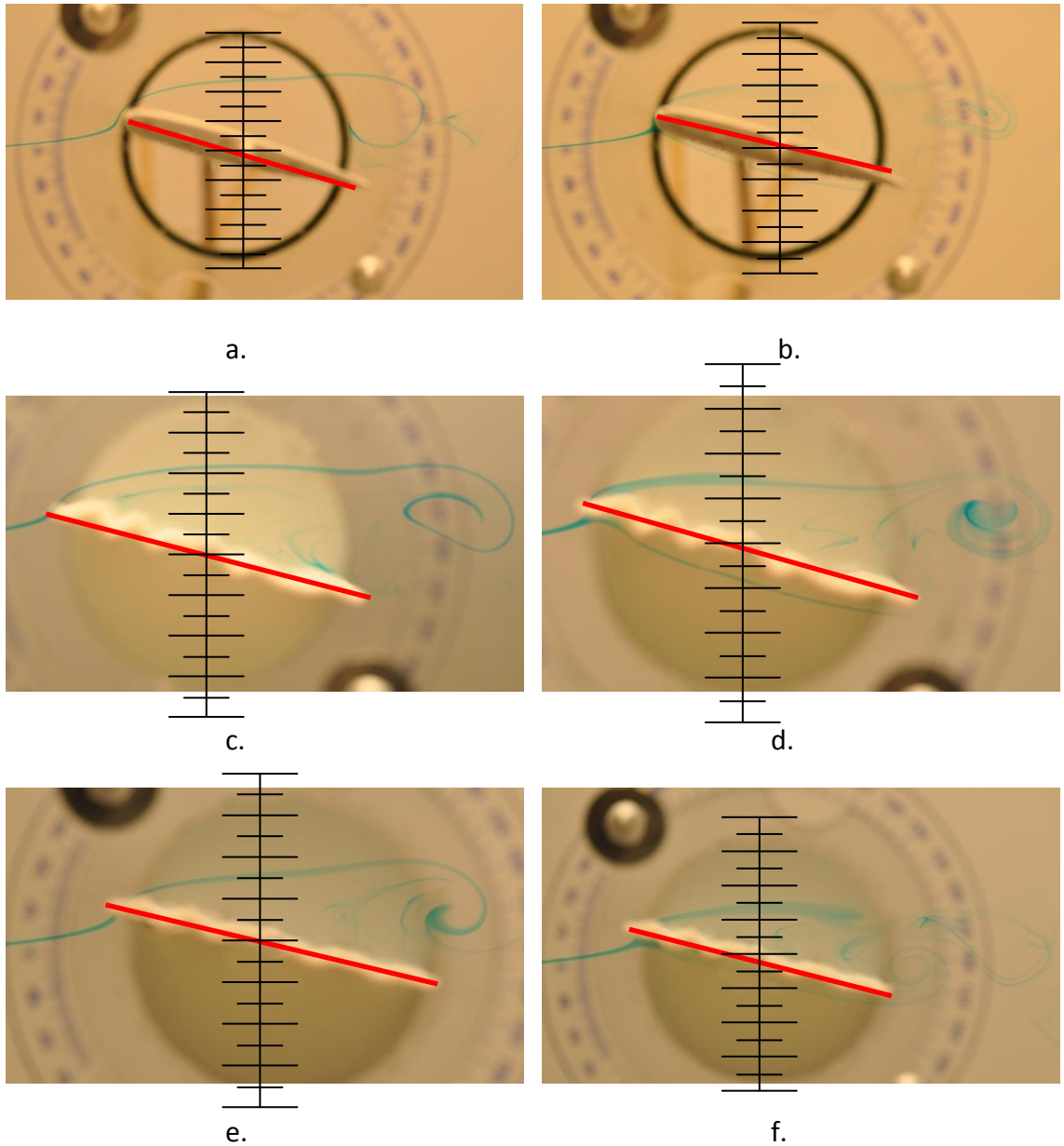
Figure 4-4: 16 degrees AoA Top (left) and Stagnation (right) Streaklines for NACA 0012, Murphy, and Kesel

Separation can be seen at the leading edge of each airfoil with the top streakline breaking away from the foils and not reattaching. In this case, the foils are considered to be completely stalled. The top streakline is easily distinguished with a vortex being generated above the trailing edge of the airfoil in each left image of Figure 4-4 and represent the generalized flow shape created by each airfoil. Separation distances were once again compared with stagnation streaklines. The stagnation streakline in Figure 4-4 became faint and difficult to distinguish in the α=16° orientation. This could likely

be due to turbulence dispersing the dye as the streakline traverses along the disturbed region between the top surface and top streakline.

The NACA 0012 airfoil in Figure 4-4.b had a separation distance of 0.44c measured at the trailing edge. Diameter of the NACA 0012 shed vortex captured Figure 4-4 is 0.13c. The Murphy profile in Figure 4-4.d generates a separation distance of 0.38c along with a shed vortex with a diameter of 0.13c while the Kesel profile in Figure 4-4.f has a separation distance of 0.31c between the top and bottom streaklines and shed vortex of 0.13c.

Continuing to increase the angle of attack, the foils were rotated to α=28° in Figure 4-5. Since we have already observed separation at the leading edge for a lower angle of attack we are observing similar flow structure for this case with only the separation distances changing.
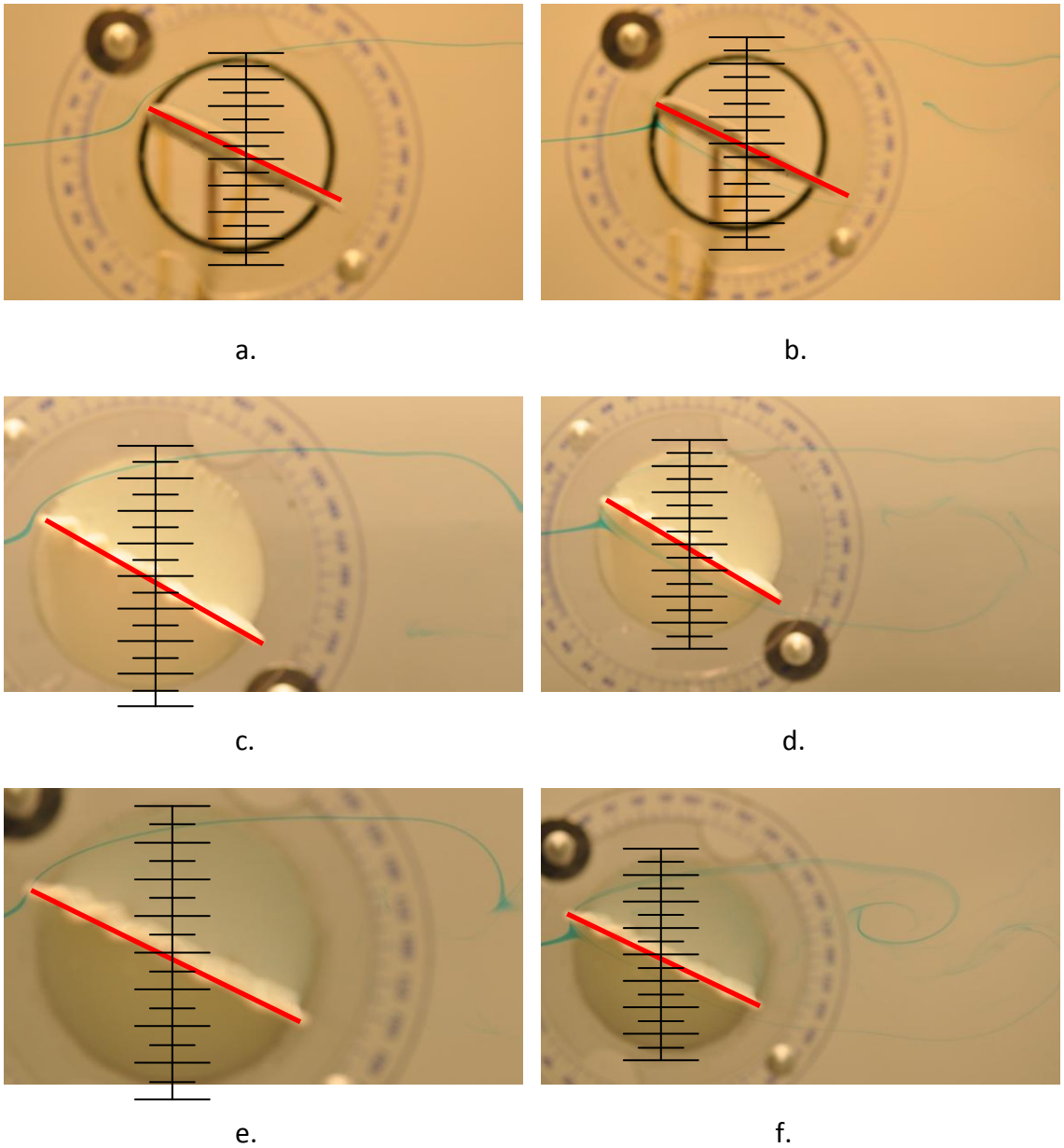
a.

b.

c.

d.

e.

f.

Figure 4-5: 28 degrees AoA Top (left) and Stagnation (right) Streaklines for NACA 0012, Murphy, and Kesel

The top and stagnation streaklines at α=28° are shown in Figure 4-5 and resemble the flow structure shown in Figure 4-4 seen previously. Even with the same shape, the 28 degree angle of attack causes a much larger distance between the top and bottom streaklines. In this case the maximum distance has increased to 0.88c, 0.81c, and 0.75c for the NACA 0012, Murphy, and Kesel foils respectively. The separation distance for each airfoil increased from those measured in Figure 4-4 at α=16°. Another interesting thing to note is the separation distance trend was the same for α=28° as with

16° with the NACA 0012 airfoil having the largest distance followed by Murphy then Kesel with the smallest distance.

The largest angle of attack generated in this investigation was α=40° which is represented in Figure 4-6. As with the previous angles of attack, the flow is stalled and has similar shape as α=16° and 28° only with larger separation.
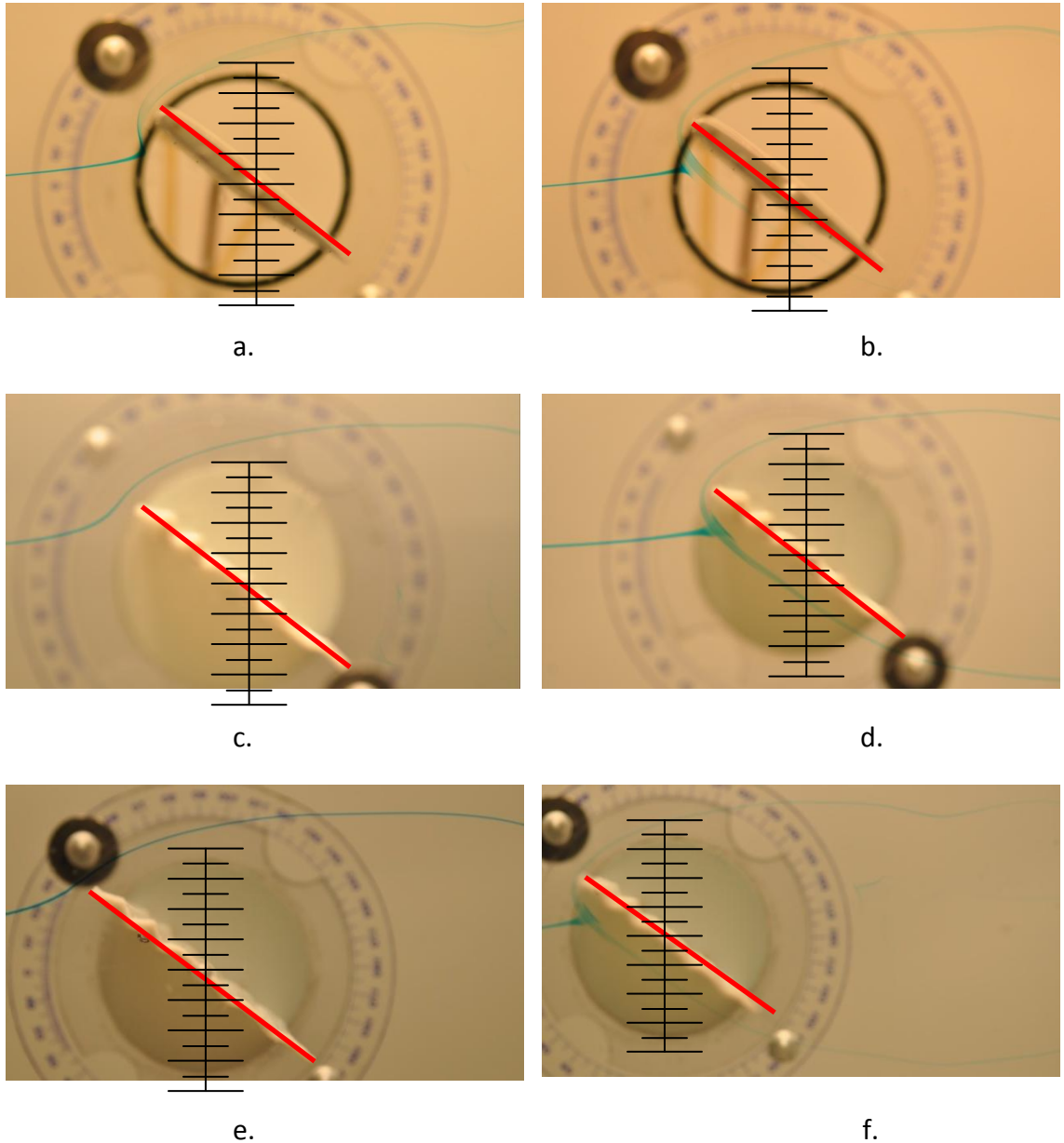

a.

b.

c.

d.

e.

f.

Figure 4-6: 40 degrees AoA Top (left) and Stagnation (right) Streaklines for NACA 0012, Murphy, and Kesel

The left images of Figure 4-6 display the top streaklines and show a larger separation than previously at α=28° and the shed vortices are not captured in the images. Stagnation streaklines are once again shown in the right column and were used to compare separation distances between foils. At this high angle of attack, the NACA 0012 airfoil had a separation distance between top and bottom streaklines of 1.125c which again is an increase from previous smaller angles of attack. The Murphy profile in Figure 4-6.d and Kesel of Figure 4-6.f both had a 1.0c separation distance.

Increasing the angle of attack for each airfoil consistently increased the separation distance for each airfoil. However, the order of least to greatest separation distance between foils was not always the same at each angle of attack. This rearranging of order gave support that the foils performed differently at various angles of attack. Even with similar flow structure, the Murphy profile consistently generates a larger separation from the chord centerline than the Kesel profile at similar angles of attack. Using flow visualization figures previously represented, the separation distance values were averaged for the captured images of each airfoil at each angle of attack (0°, 8°, 16°, 28°, and 40°).
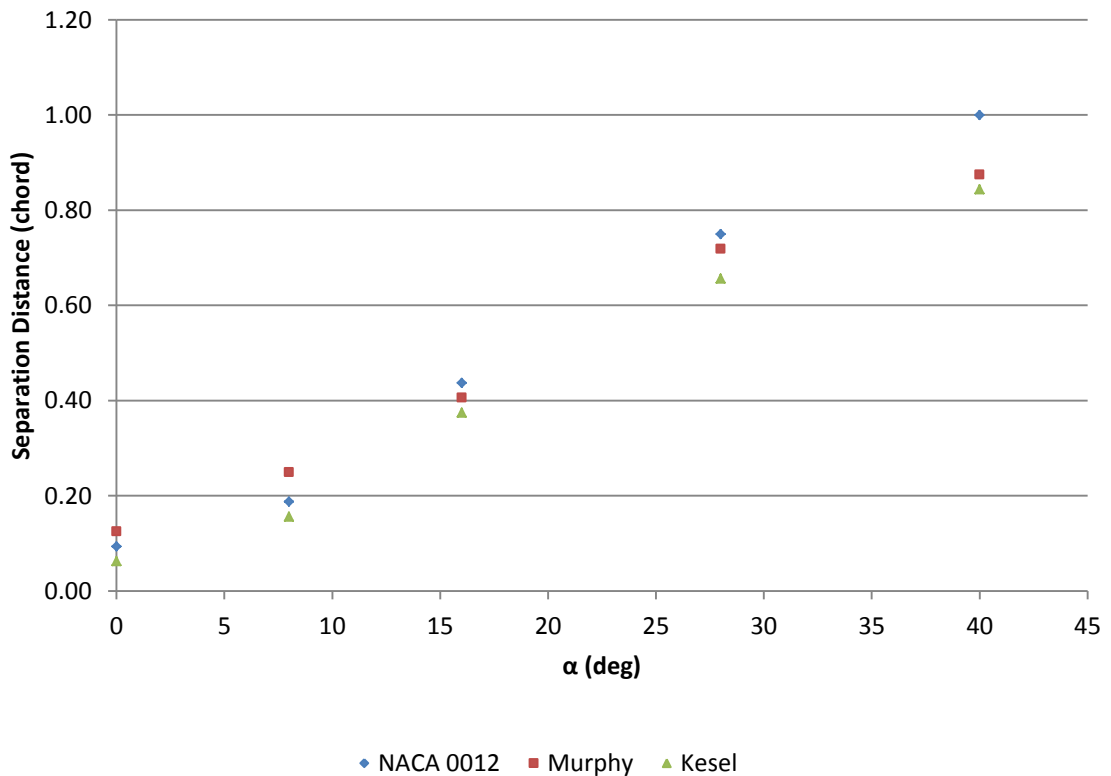

Figure 4-7: Top Streakline Separation Comparison

From Figure 4-7, it can be noted that there is not much difference in the separation distances from the chord line to top streakline values of each airfoil. At α < 25°, the separation values are at most 0.09c different. Higher angles of attack yield a maximum difference of 0.16c. Another pattern to notice is the Kesel profile has the least separation at each angle of attack. On the other hand, the Murphy profile has the largest separation at α= 0° and 8° after which the NACA 0012 generates the largest separation at 16°, 28°, and 40°. Larger separation distances likely result in greater drag due to creation of a larger frontal area for the foils. This larger frontal area will create a larger low pressure region immediately downstream of the airfoil which increases pressure drag. Lower pressure behind the foil downstream will "pull" the airfoil opposite of its travel. Assuming the pressure in the wake region is approximately equal between the airfoils, increasing this region serves to increase the pull and yield more drag. The performance increase for the corrugated profiles appears to be most apparent post-stall (α > 8°), where the corrugated profiles yield the least separation distance.

Figure 4-8 presents data for the same airfoils and angles of attack except the separation distances are from the stagnation streakline images.
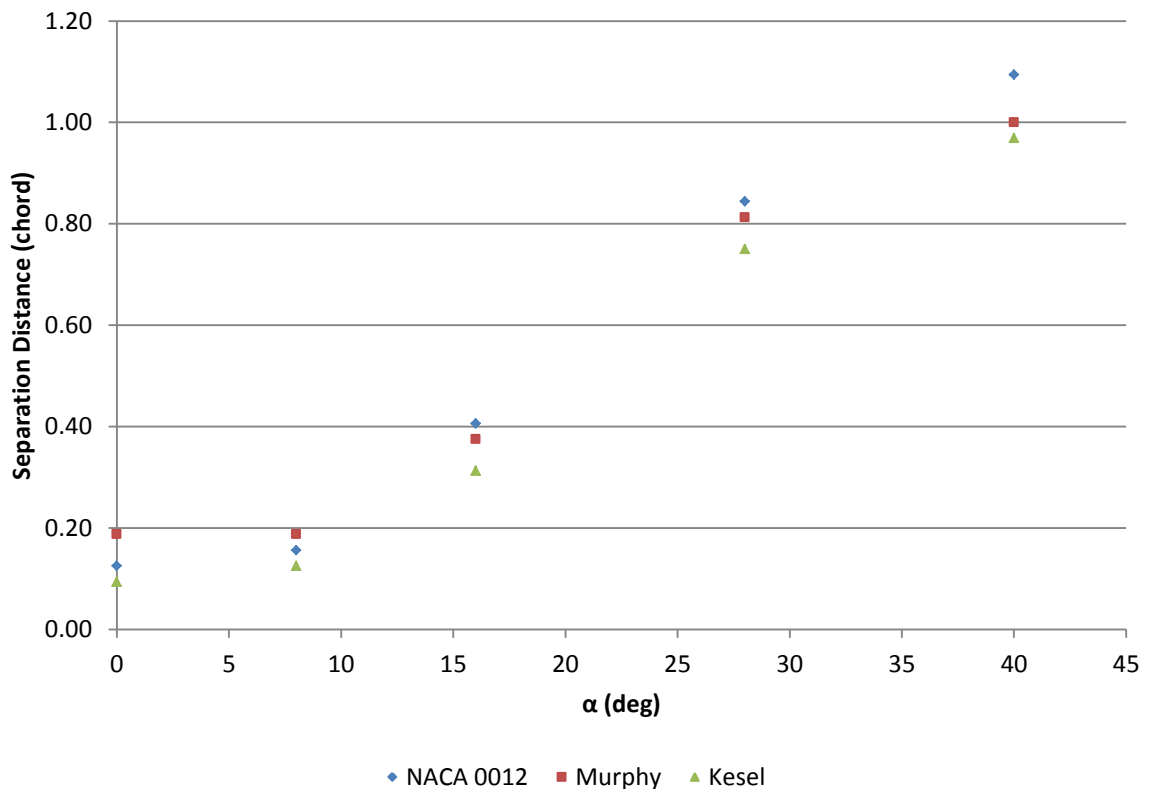

Figure 4-8: Stagnation Streakline Separation Comparison

The stagnation separation comparison in Figure 4-8 has the same trend as Figure 4-7. That is, the Murphy profile has the largest separation at angles of attack below 25° and the NACA 0012 has the largest separation for angles above 25°. Again the Kesel profile has the least separation at each angle of attack indicating it may produce the least drag of the three foils under investigation.

Generating the stagnation streaklines also permitted the stagnation point location to be identified at the investigated angles of attack for the three airfoils. Documenting how the stagnation point location moves at each α provides insight with regards to lift generated by the foils. The same images used for Figure 4-7 and Figure 4-8 were used to compare the stagnation point location.

Locating the stagnation point was completed by using a similar scale as before in the images with a higher resolution. Location of the stagnation point was measured from the leading edge to the streakline stagnation perpendicular to the chord line of the airfoil. An example of the scale and method is represented in Figure 4-9.
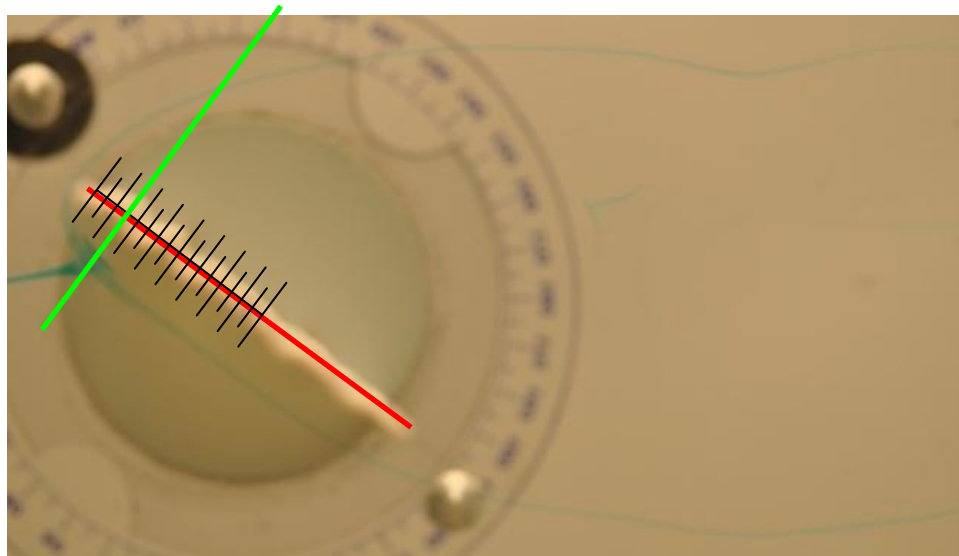

Figure 4-9: Stagnation Location Point

The small tick marks of the scale in Figure 4-9 are increments of $c/32$. The green line is drawn perpendicular to the chord line and passing through the center of the stagnation point. In this example the stagnation point initiates at $0.14c$. This process was completed for each airfoil at the angles of attack under investigation. Results of this data are presented in Figure 4-10.
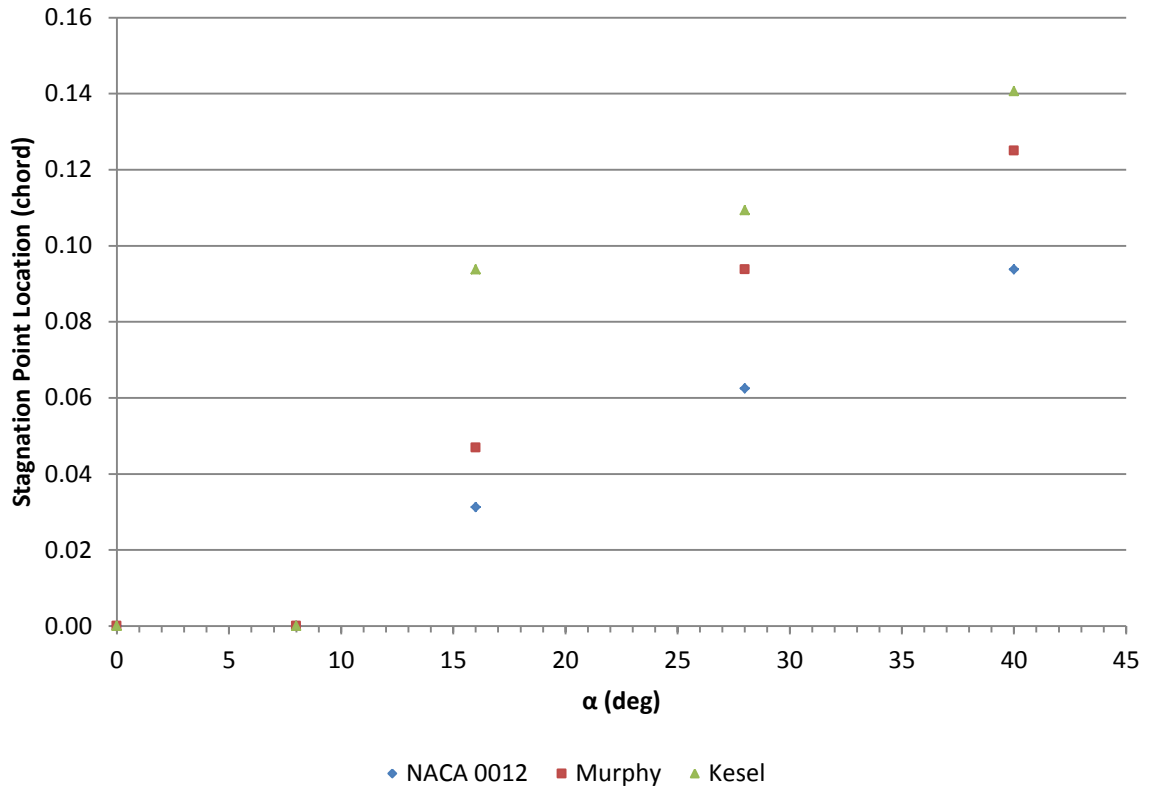
Figure 4-10: Stagnation Point Location

At α=0° & 8°, the stagnation point could not be identified behind the leading edge. These stagnation points were documented as 0.0*c*. The remaining angles of attack were identified and plotted in Figure 4-10. An interesting trend can be noted in this chart identifying the corrugated profiles had their stagnation points located further from their leading edges than the smooth NACA 0012 airfoil at each angle of attack. Furthermore, the Kesel profile had the largest distance from the leading edge at each angle. Location of the stagnation point is relevant to the lift generated by the different airfoils. As the flow splits around the airfoil, the flow passing on top of the airfoil must accelerate forward and around the leading to reach the top surface. Increasing the distance traveled by the top streakline increases the low pressure surface area used in calculating lift. Increasing the low pressure area on the surface of the airfoil leads to more lift generated by using Equation 7 (Wilcox, 2003).

$$L = i \cdot \oiint [-(p - p_\infty)n + \tau_w t] dS \qquad \text{(Eq. 7)}$$

While pre-stall stagnation point locations were not documented, the corrugated airfoils once again showed favorable aerodynamic characteristics at post-stall angles of attack.

40

4.2 Corrugated Vortices

As mentioned in section 3.5 Experimental Setup, great interest lies around the flow structures in the valleys of the corrugated profiles labeled in Figure 4-1. To examine flow in these regions the dye injection syringe from Figure 3-12 was utilized to introduce dye directly onto the desired surface. Using a different color dye for the top streakline and vortex allows the boundary to be distinguished more easily. The top streakline was maintained in order to observe the smooth boundary as well as the flow structure in the corrugated valleys.

Figure 4-11 displays vortex #1 generated in the first valley of the Murphy airfoil. It can be seen in the image how the top streakline distinctly flows over the vortex without mixing. This vortex represented with purple dye can be seen very easily and supports the hypothesis of Vargas and Mittal (Vargas & Mittal, 2004) who claims these types of vortices may become trapped in the corrugation and create a smoother airfoil even with the rough corrugated profile.
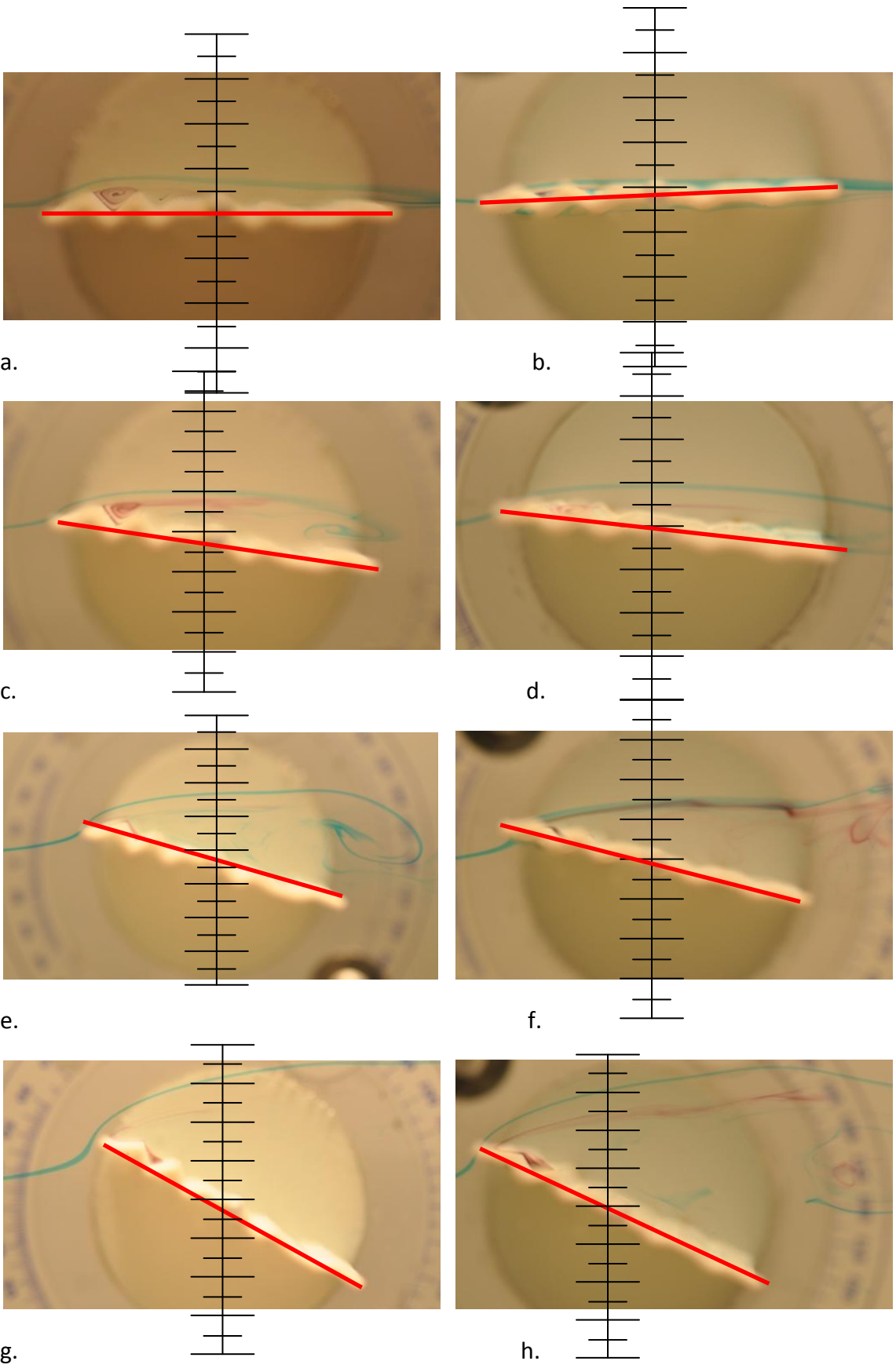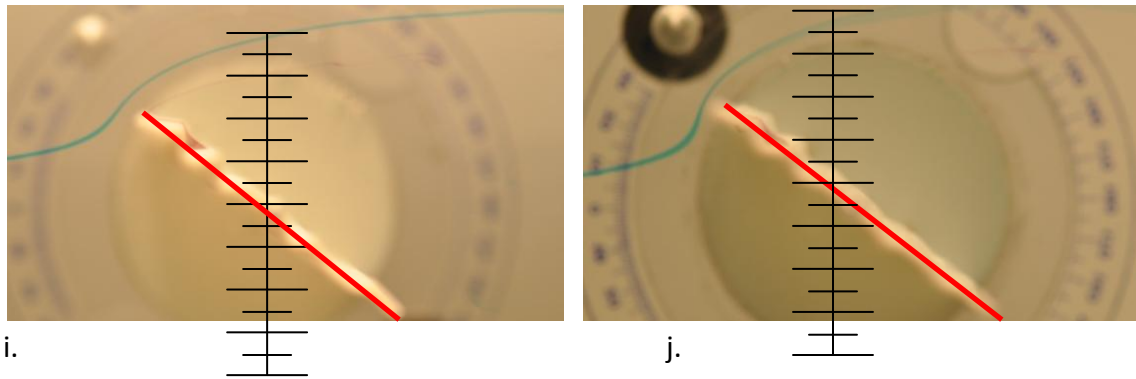
Figure 4-11: Corrugated Profile Vortex #1 for Murphy (left) and Kesel (right) at α=0°, 8°, 16°, 28°, and 40° (top-bottom)

Each corrugated profile had the additional cases investigated with dye injected into each valley with the top streakline maintained. Figure 4-11 represents the Murphy (left) and Kesel (right) profiles with vortex #1 observed at each angle of attack. You can see the top streakline in blue following the smooth profile shape observed previously as well as the vortex generated in the valley in purple. Notice how the top streakline and vortex do not mix but appear to develop independently.

While both profiles trap vortices in the valley at α=0°, the Murphy profile generates a much more pronounced vortex. The Murphy vortex has a height of slightly over 0.06c when measured from the centerline and a profile thickness of 0.13c when measured from the same centerline. The Kesel profile on the other hand, has a vortex height of roughly 0.03c and profile thickness of 0.06c when measured from the centerline. Once the centerline is drawn it appears the Kesel profile actually has a negative angle of attack which could account for the much smaller profile and vortex dimensions on the top of the airfoil.

Some mixing is evident at the trailing edge of α=0° with the distinct top streakline mixing and breaking apart. This is expected to be due to the formation of the von Karman vortex wake from shear layer separation at the trailing edge.

At α=8° in Figure 4-11.c, the Murphy profile has a vortex generated with a height of just over 0.06c while the Kesel profile of Figure 4-11.d has a smaller height of around 0.03c when measured from the chord line.

At no angle of attack above 8° in Figure 4-11 does a vortex generate in the valley #1 region. Instead of creating a vortex, the flow is pulled forward to the leading edge where it separates and departs the airfoil surface to follow just below the top streakline still in view. Flow structure is identical in each case represented here except for the

separation distance increasing which has already been observed and documented in Figure 4-2-Figure 4-6.

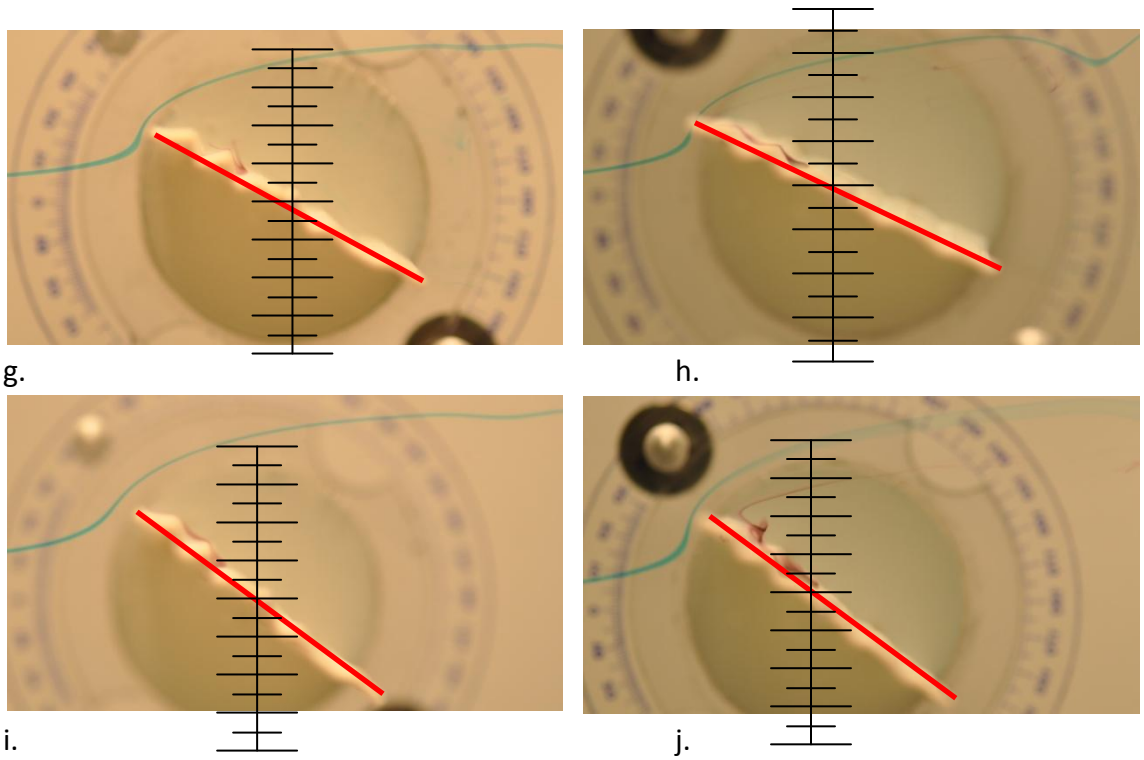Vortex #2 was generated identically as vortex #1 and displayed in Figure 4-12.

a.

b.

c.

d.

e.

f.

g.

h.

i.

j.
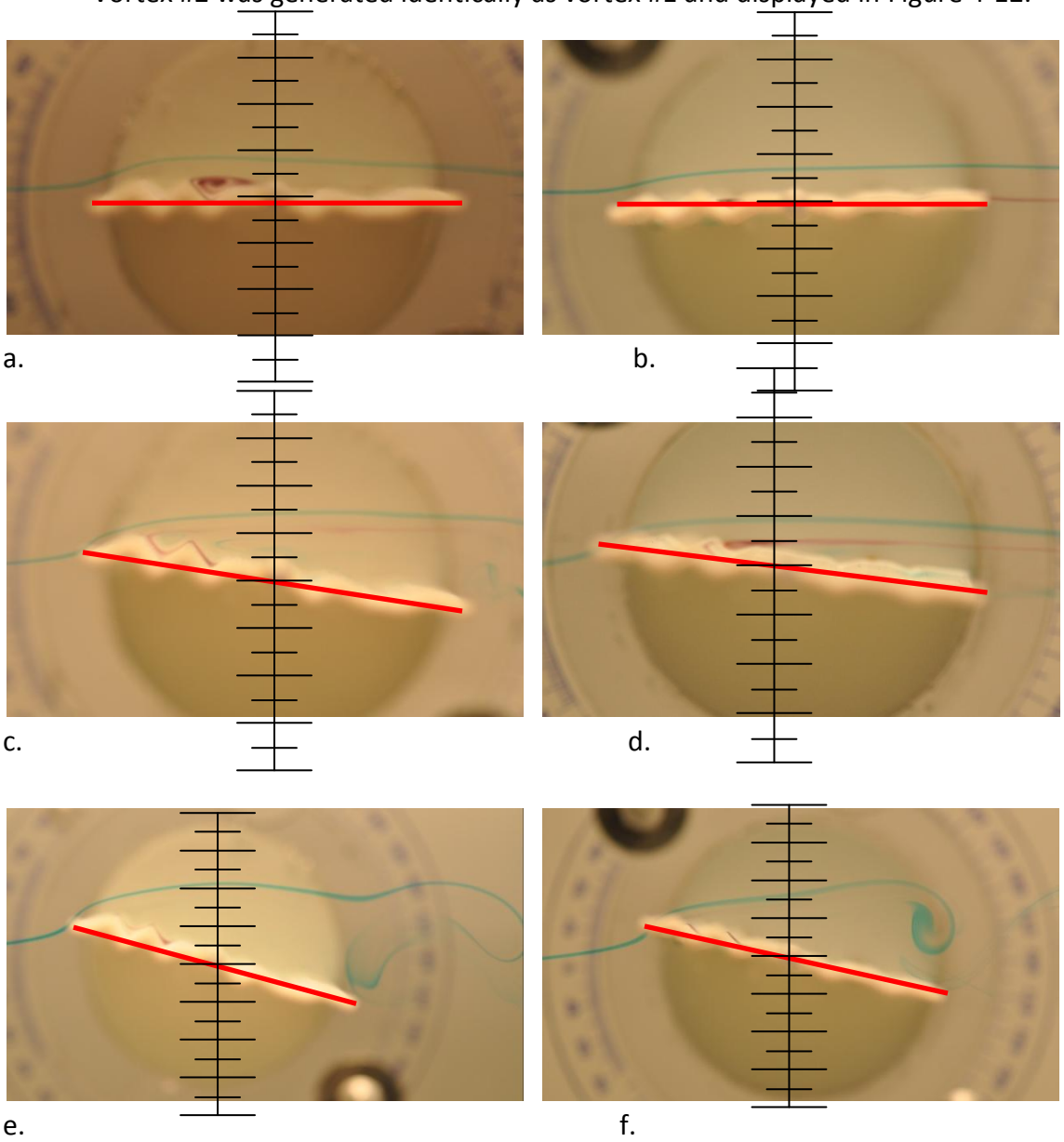
Figure 4-12: Corrugated Profile Vortex #2 for Murphy (left) and Kesel (right) at α=0°, 8°, 16°, 28°, and 40° (top-bottom)

Vortex #2 is quite distinct and easily identified in its region on the Murphy profile in Figure 4-12.a for α=0°. The front side of the vortex follows the airfoil profile very closely. At the back end, you can see the vortex trailing down the wing towards the trailing edge. With the rear boundary shorter than the front, the vortex is permitted to expand outside the valley causing it to not be contained as well as vortex #1 was. The Murphy profile has a vortex with a height of slightly over 0.06c when measured from the chord line in Figure 4-12.a compared to a height of only 0.03c for the Kesel profile at the same angle of attack.

As α is increased, the separation distance of the top streamline increases as well. At α=8° a vortex is not formed in the valley of Murphy. Instead, the dye injected into valley #2 is pulled forward to the first peak from the trailing edge before it breaks away and trails under the top streakline. Lack of a vortex generating indicates stall has occurred and the separation point is closer to the leading edge. This was noticed in Figure 4-3.d where the Murphy profile has separation occurring at 0.13c for α=8°. An interesting thing to note here is the purple dye comes close to reattaching to the second peak of the Murphy profile and represents the boundary between recirculating fluid in valley #1 and flow passing over the airfoil smoothly.

45

Recalling that separation occurred at 0.5c for the Kesel profile at α=8° from Figure 4-3.f, you can see that the Kesel profile does have the vortex form in the second valley and shown in Figure 4-12.d along with the streakline trailing from the vortex at its back side. The vortex is formed in valley #2, unlike the Murphy profile, due to the separation location being behind valley #2. In this case, the vortex has a diameter of 0.06c which is twice that generated in the same valley at α=0°.

Once again, similarities can be seen between the corrugated profiles and the changes in flow structure size when the angle of attack is increased. As with the flow located in Figure 4-12.c the vortex at the profile surface of valley #2 does not develop and only sweeps forward before separating from the airfoil. The same flow structure can be seen in Figure 4-12.e-j for both corrugated foils.

Vortex #3 was generated in the same manner as vortex #1 and #2 and is presented in Figure 4-13 below.
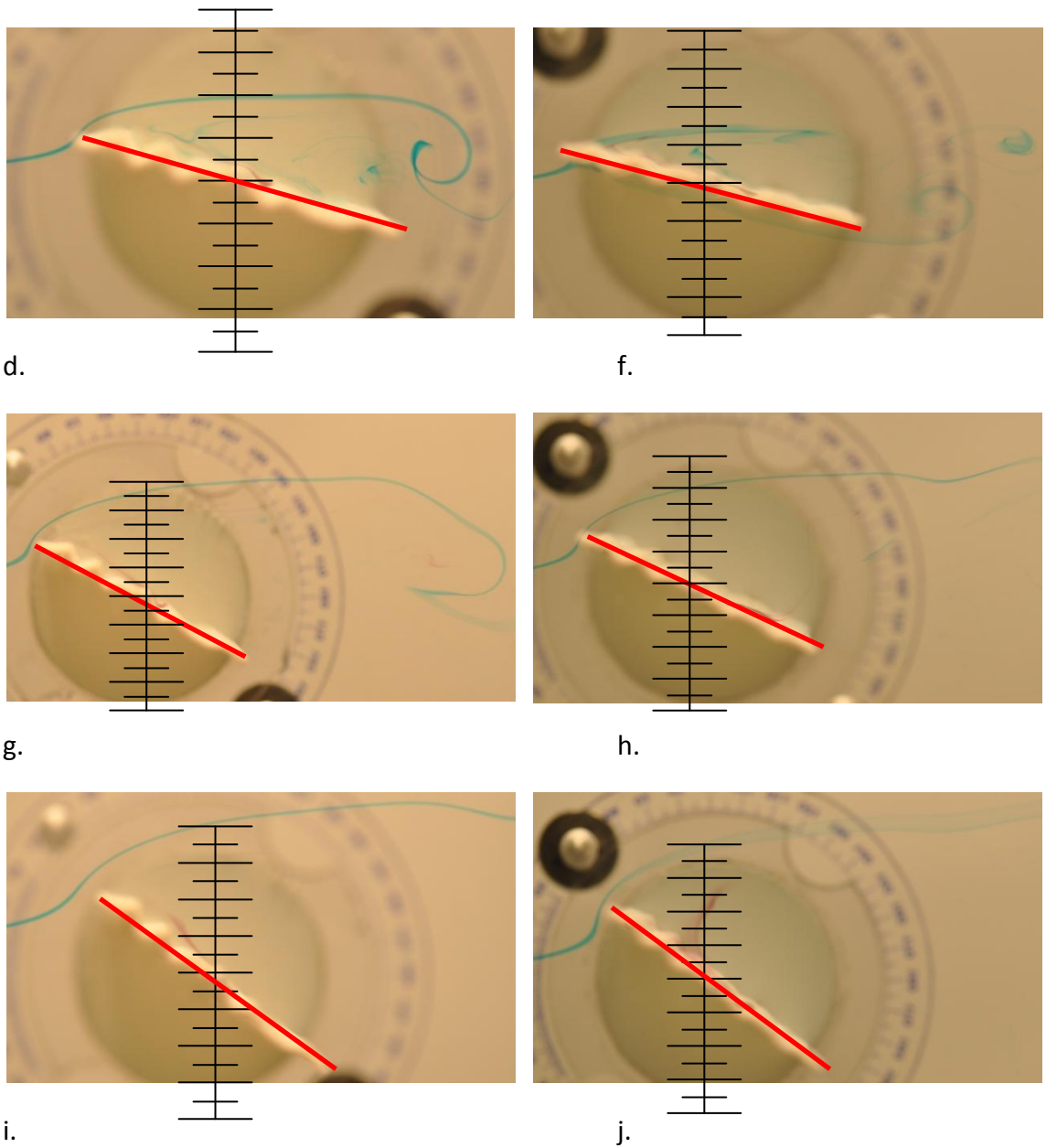

a.

b.

c.

d.
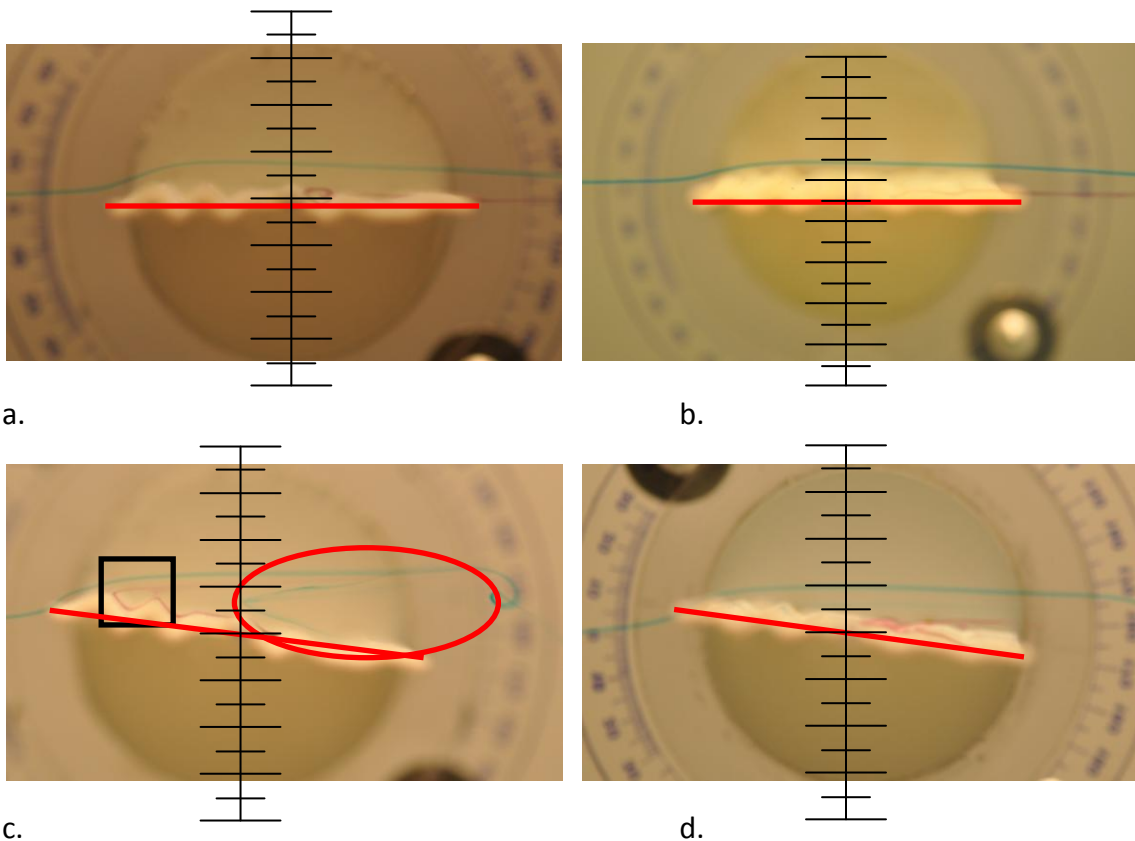
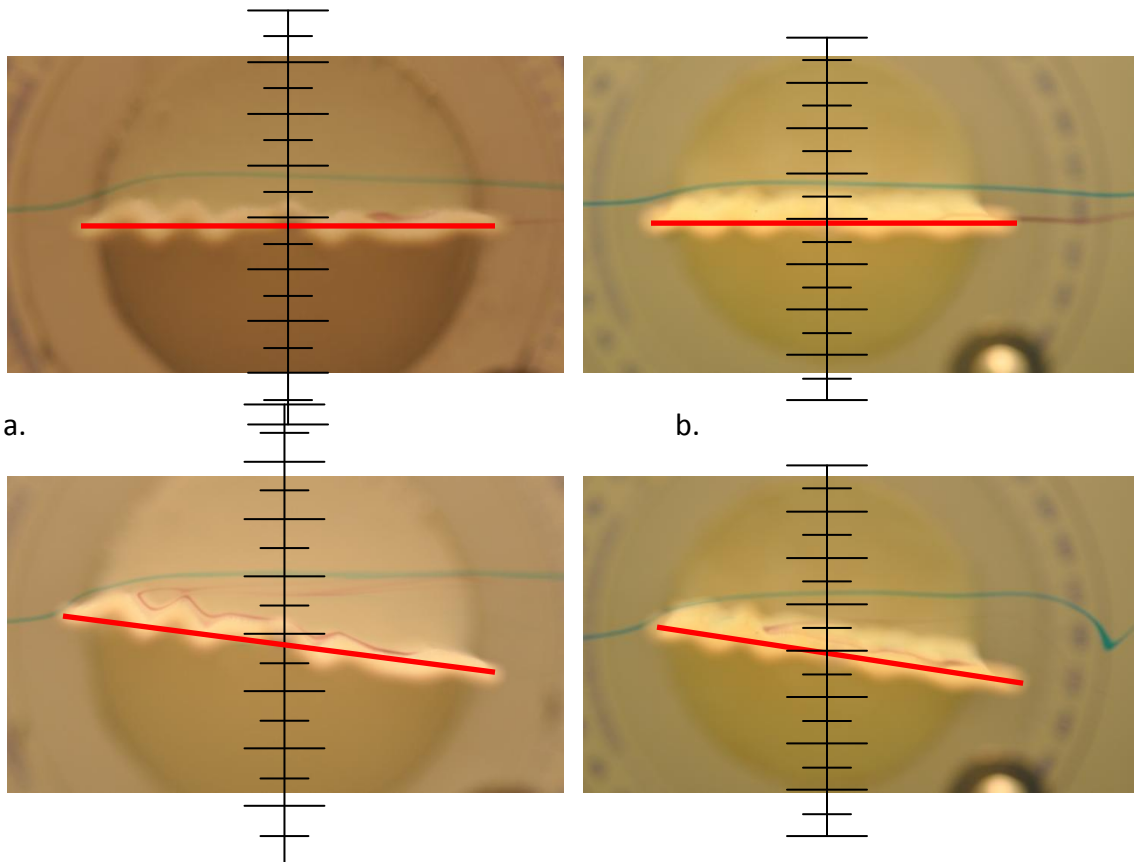Figure 4-13: Corrugated Profile Vortex #3 for Murphy (left) and Kesel (right) at α=0°, 8°, 16°, 28°, and 40° (top-bottom)

Figure 4-13 represents the third vortex for each corrugated profile. The Murphy profile has a vortex in valley #3 with a diameter of 0.03c at α=0° when measured from the chord line while the Kesel profile does not generate a vortex. Again, neither profile has a vortex generated at an angle of attack above α=8°. As for vortex #2 in Figure 4-12, the dye holds close to the profile surface and is pulled forward to the leading edge before breaking off and following the top streakline. Looking closer at the flow structure, you can see the recirculation below the top streakline indicated at the red circle for Murphy in Figure 4-13.c. This recirculation is responsible for pulling the

injected dye forward and keeping a vortex from being generated up to valley #2 as a consequence of separation occurring at the first peak.

The Kesel profile has a similar flow structure as with Murphy. Kesel's profile shape has a similar valley that is more shallow than Murphy's and therefore has the dye pulled forward as before. One difference is the Kesel dye does not pull as far forward as did Murphy. Instead of going to the leading edge before breaking away, the Kesel breaks away just after passing the valley moving forward which is shown in Figure 4-13.d.

Another interesting thing to notice is the purple dye re-attaching at a peak after it has separated from the surface at valley #1 and highlighted with the black square in Figure 4-13.c for the Murphy profile. This streakline does not become trapped in the vortex of valley #1 but continues to trail down just below the top streakline and indicates the separation location and recirculation region as mentioned before for the Murphy profile at α=8°. This flow reattachment represented here was documented by (Kwok & Mittal, 2005) in their flow visualization study as well.

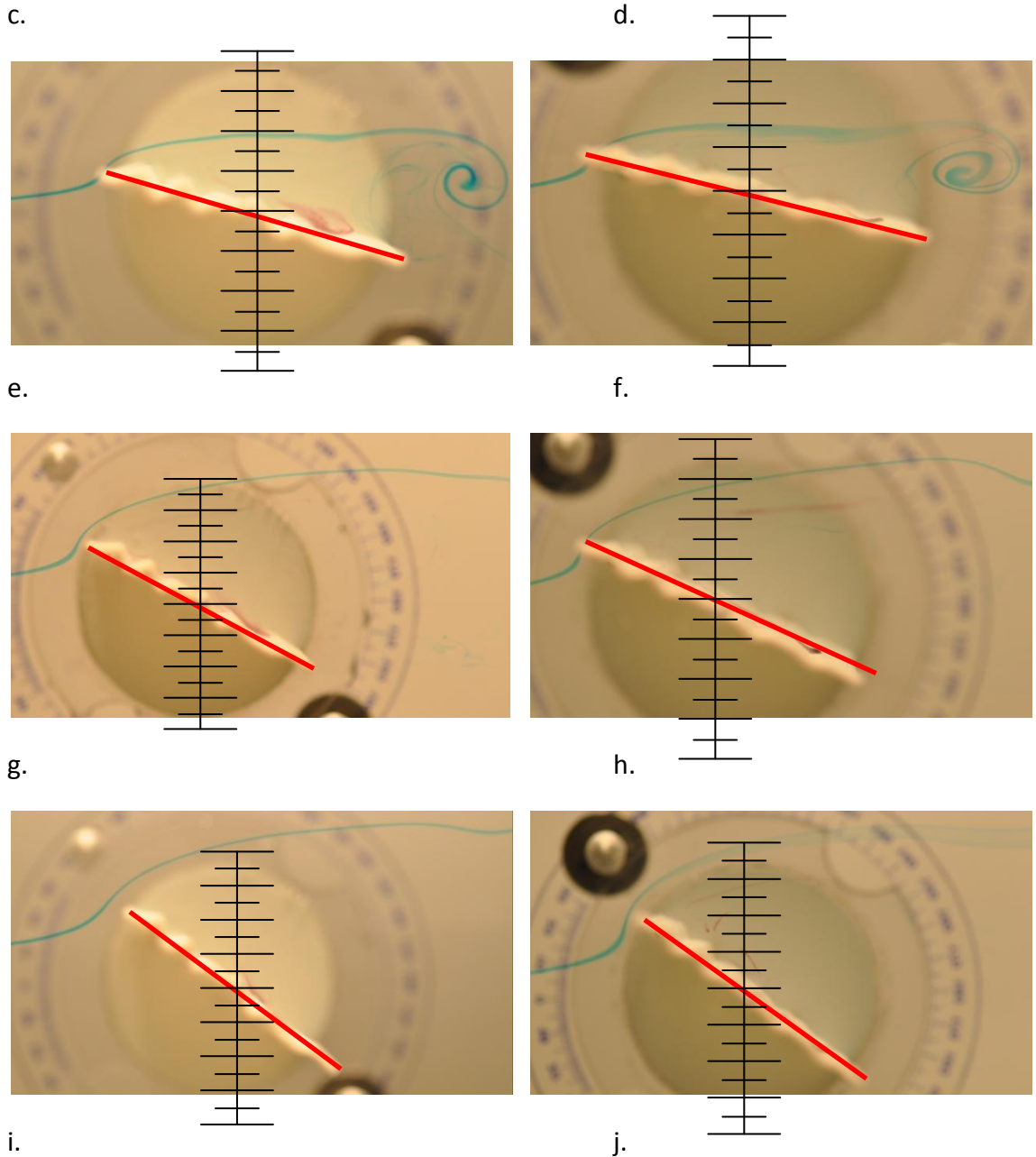The final vortex observed for the corrugated profiles was vortex #4 which is displayed in Figure 4-14.

a.

b.

Figure 4-14: Corrugated Profile Vortex #4 for Murphy (left) and Kesel (right) at α=0°, 8°, 16°, 28°, and 40° (top-bottom)

Valley #4 for the Murphy profile is a wide and shallow region that does not generate a vortex on the surface at any angle of attack.   At α=0°, the injected dye holds close to the surface with little movement noticed. As α is increased, the dye persists to travel towards the leading edge as was noticed before.   Another instance of the dye separating and re-attaching as documented in Figure 4-13.c is observed again in Figure 4-14.c for the Murphy profile at α=8°.   Above α=8°, each airfoil has the manually

injected dye separating and following below the top-blue streakline. However, the separation location of the manually injected dye occurs at the second peak of the Murphy profile whereas the Kesel profile separates behind the second peak and closer to mid-chord of the airfoil.

4.3 Tuned Corrugated Profiles

The streamlined profiled generated with stagnation streaklines for the Murphy profile in Figure 4-15 displays how the corrugated profile resembles a NACA four digit series airfoil shape. Using conventional NACA four digit series airfoil naming convention taken from Abbott & Von Doenhoff (1959), the boundary generated by the Murphy profile resembles the shape of a NACA 1112. This is an approximation created by sketching the mean camber line for the foil (represented with the red line) and measuring camber values, camber location, and profile thickness with the scale displayed below the Murphy airfoil in $c/32$ increments. While the Murphy boundary profile may not follow the equation prescribed for a NACA four digit series cambered profile perfectly, tuning the corrugated profile could generate a very similar shape. Generating a similar NACA XXXX airfoil shape can be observed in instances where the flow around the airfoil remains attached allowing for clear observation of the boundary generated by the corrugated profile.
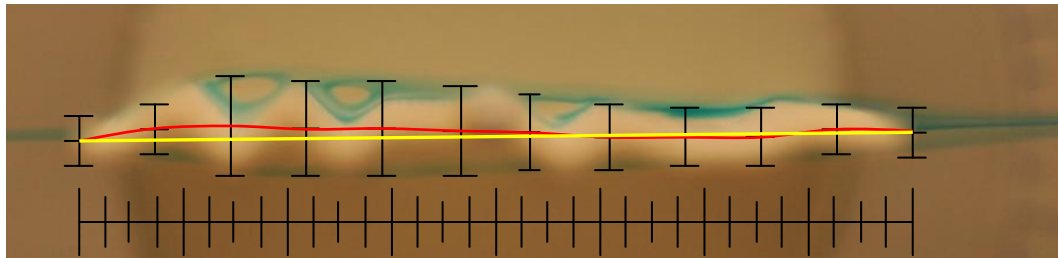

Figure 4-15: Murphy Stagnation Streakline at α=0°

4.4 Comparison with Computational Fluid Dynamics

CFD results obtained by Hord & Lian (2011) for the Murphy corrugated profile at $Re_c=1,000$ are compared against experimental results from the water tunnel for α = 0 & 8° and shown in Figure 4-16 and Figure 4-17 respectively.

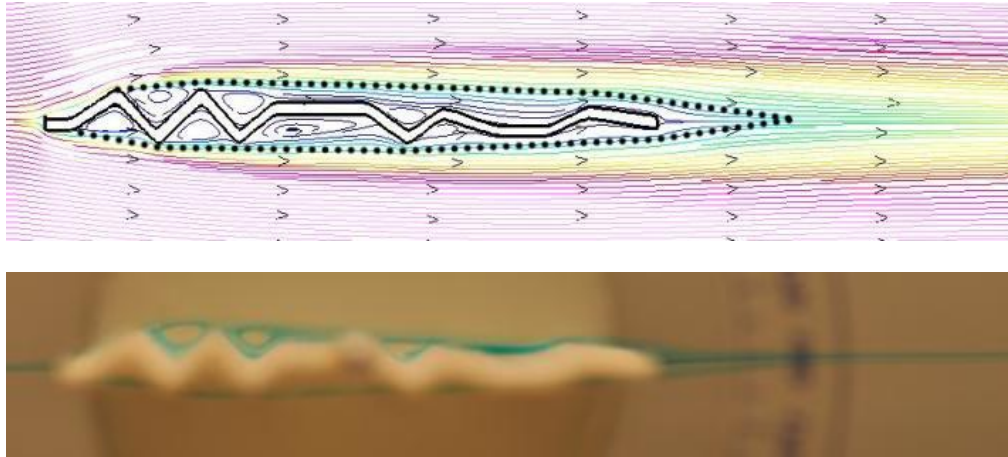Figure 4-16: Murphy Experimental (bottom) vs. CFD (top) Comparison at α=0°

Comparing the dotted profile of the CFD streamline plot to the streaklines of the experimental image at α=0° you can notice a similar profile shape. Vortices captured in valleys #1-#3 of the experimental image are also displayed in the CFD results. Valley #4 of the experimental image does not generate a vortex but has a streakline which holds close to the surface while passing towards the trailing edge. A similar result for valley #4 is also apparent for the CFD result. What appears to be different between the images is the generation of vortices on the bottom side and the appearance of a symmetrical profile generated by CFD while the experimental profile is more cambered. Vortices on the bottom side of the experimental image may exist and not be captured due to camera angle or insufficient dye to highlight the vortices. However, the difference in profile shape does differ which may be due to slight profile differences or CFD model assumptions.
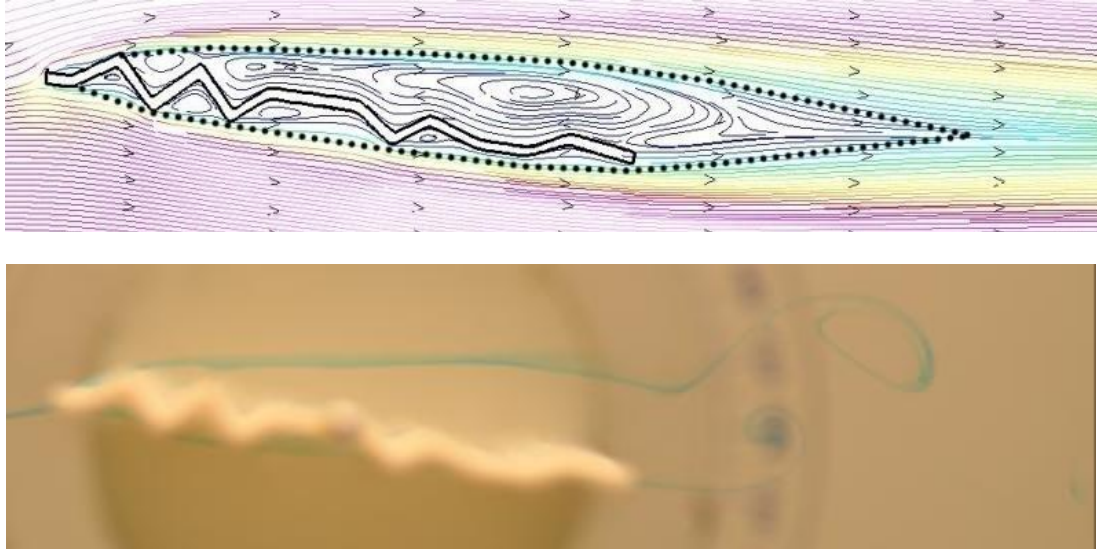
Figure 4-17: Murphy Experimental (bottom) vs. CFD (top) Comparison at α=8°

α = 8° is shown in Figure 4-17 comparing results as well. In this case the profile shape appears similar with faint rotations captured in valley #1 of the CFD and experimental result. However, the biggest difference is the CFD result does not capture the vortex shed from the trailing edge of the top or bottom surface as represented in the experimental result. This difference could lie in the CFD assumption of pure laminar and steady flow at the investigated Reynolds number of 1,000 while the experimental results are unsteady in time.

Chapter 5 : Dynamic Fixture Development

5.1 Specifications

While the natural motion of flight is quite complicated and typically takes the "Figure 8" shape, this investigation will simplify the motion into a two degree of freedom motion of "pitch" and "plunge". Here, pitch describes rotation about an axis perpendicular to, and at midpoint of, the chord while plunge describes vertical translation of the airfoil. Images representing the motion can be seen in Figure 5-1.
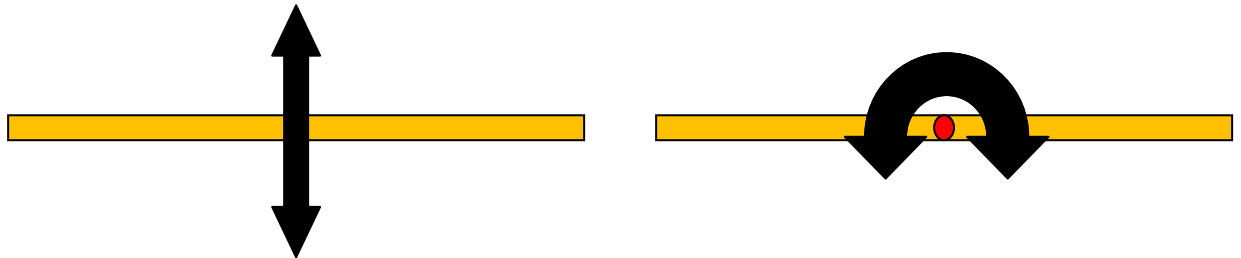

Figure 5-1: Simplified Degrees of Freedom (left: Plunge, right: Pitch)

The plunge motion used is +/-0 .5c at the specified frequency. Pitch will match the plunge frequency with amplitude of +/- 45° while being in phase with plunge displacement. These specifications were chosen to match previous CFD simulations of Hord, Broering, & Lian.

Combining these two pitch and plunge motions creates the motion path represented in

Figure 5-2 where t represents the cycle period. Phases of this motion are described in regards to plunge direction and pitch angle in Table 5:1 as well. Maximum pitch amplitude occurs at the maximum vertical plunge displacement while the minimum pitch amplitude occurs at the minimum plunge displacement.
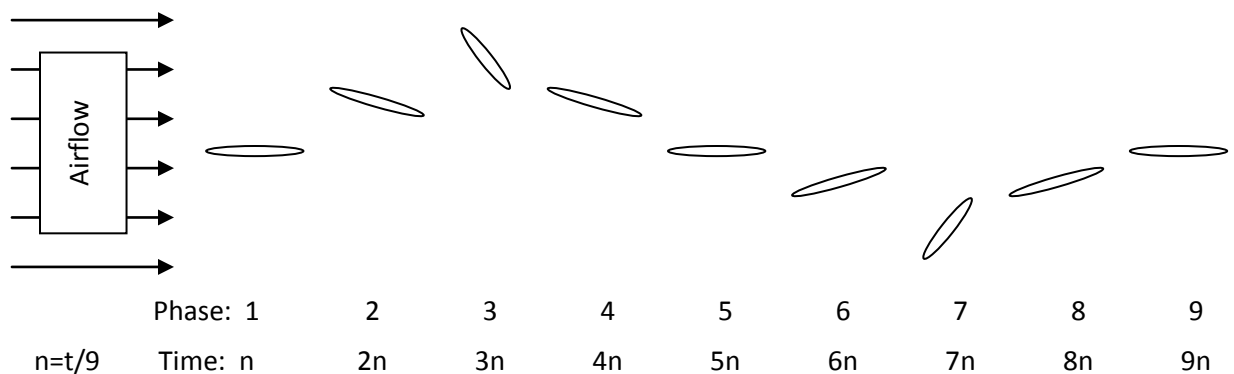

| | Phase: 1 | 2 | 3 | 4 | 5 | 6 | 7 | 8 | 9 |
| n=t/9 | Time: n | 2n | 3n | 4n | 5n | 6n | 7n | 8n | 9n |

Figure 5-2: Pitch and Plunge Motion Path

Table 5:1: Motion Path Description

Phase	Plunge Direction (up/down)	Approximate Plunge Displacement (chord)	Pitch Angle (+/-)
1	↑	0.0	0
2	↑	+0.5	+
3	Maximum	+1.0	+ Maximum
4	↓	+0.5	+
5	↓	0.0	0
6	↓	-0.5	-
7	Minimum	-1.0	-Minimum
8	↑	-0.5	-
9	↑	0.0	0

Observing Table 5:1, you can see at Phase 1 the plunge direction was upward (↑) with the pitch angle equal to 0° and plunge displacement 0.0c. Phase 2 continues the upward motion with a positive pitch angle (+) before reaching the maximum plunge displacement of +1.0c and maximum pitch angle of Phase 3. Phase 4 has changed plunge direction to downward (↓) while maintaining a positive pitch angle and positive plunge displacement. Phase 5 passes through the 0° location again as Phase 1 except now the plunge direction is downward. Phase 6 continues the downward plunge with a negative pitch angle (-) before reaching the minimum pitch angle and plunge displacement of -1.0c of Phase 7. At Phase 8, the plunge direction has once again switched directions to upward while still having a negative pitch angle and negative plunge displacement. Phase 9 is identical to Phase 1 where the cycle repeats itself.

Scaling equations which drive development of the fixture are chord Reynolds number and Strouhal number introduced previously. In addition to these scaling laws, a spacing of 10 chord lengths was required from the mid-chord point to the closest rigid boundary. This distance was required to avoid fluid interaction with the facility walls during the motion. The target Reynolds number for this investigation, to ensure low Reynolds number flow was 1,000 but any value under 10,000 was also considered acceptable. Thus, the final produced airfoil size, facility type, and flow velocity had to be selected in order to achieve this Reynolds number range. Typical natural flyers operate in cruising flight between Strouhal numbers of 0.2 and 0.4 (Shyy, Lian, Tang, Viieru, & Liu, 2008), so this fixture was designed to be in the same region.

To simplify airfoil construction, the airfoil used in the dynamic fixture was a simple flat plate spanning the wind tunnel width with the appropriate chord specified

from the scaling equations. Thickness of the airfoil was chosen to provide proper stiffness which will be discussed in more detail in section 5.5 Fixture Manufacturing.

5.2 Available Facilities

The same facilities available to house the static fixture (water tunnel, wind tunnel, and tow tank) were available for consideration for the dynamic fixture as well. The capabilities of each facility were investigated to compare its feasibility of meeting the target specifications.

5.3 Facility Comparison

Choosing the best suited facility was a process of evaluating the Reynolds number capable of being produced by the published specifications while meeting the desired spacing requirements. The maximum chord allowable to satisfy 10 chord spacing from a boundary was derived following

$$C_{max} = \frac{l_c}{21} \qquad \text{(Eq. 8)}$$

Where C_{max} is the maximum chord which would meet this specification and l_c is the characteristic length of the facility. In this case, l_c is the test section dimension in the plunge dimension.

Striving for the maximum chord was desirable because it would be easier to manufacture the airfoil and would provide a larger aerodynamic force for a given fluid speed in the event that forces were measured directly.

Next, the minimum and maximum Reynolds number could be calculated for each fixture with the appropriate maximum chord length previously determined and the manufacturer's stated fluid speed limits. Table 5:2 represents data presented previously in Table 3:1 with the addition of maximum chord for each fixture presented.

Table 5:2: Dynamic Fixture Facility Parameter Summary

Fixture	Kinematic Viscosity (m^2/s)	Max Chord (m)	Speed Range (m/s)	Re Range
Wind Tunnel	1.57E-05	0.029	1.0-45.7	1850-84600
Water Tunnel	1.52E-06	0.007	0.03-0.3	1400-150
Tow Tank	1.52E-06	0.018	0.1-0.69	1200-8000

5.3.1 Wind Tunnel

The wind tunnel provided the largest cross section which meets the wall-condition requirement and allows the largest airfoil. A larger airfoil makes the airfoil easier to produce versus the other devices. This device also permitted either vertical or horizontal mounting and was absent of liquid. No liquid present made electrical connections much easier to utilize if necessary. The arrangement of the test section of the wind tunnel also allowed the flexibility to mount the airfoil as either a cantilevered beam or fixed at both ends. Further analysis determined which mounting scenario was acceptable. Since this device drives the fluid while the test section is stationary, the test duration is infinite. This allowed data to be gathered in the quantity desired without the need to perform fixture setup multiple times. Previous research had been completed using flow visualization techniques of PIV and smoke trails in this device. Minor modifications of this visualization equipment could render it useful for this study as well.

5.3.2 Water Tunnel

The water tunnel was designed to insert an air airfoil into the side of the test section for static measurements while changing the angle of attack. In order to mount the airfoil for a pitch-plunge scenario a new test section would need to be designed. This design would be required to be water tight and likely limited to a cantilevered scenario. Mounting the airfoil vertically would be necessary so that the test section would not need to be water tight on two sides.

This facility has the smallest cross section of all available facilities, causing the airfoil to be the smallest. The smaller airfoil requires a small plunge displacement (+/-3.5mm) and more difficulty in constructing the airfoil. Facility fluid speed and a small chord also yield a Reynolds number range that was low but does satisfy the current specification of Re_c=1,000. Scaling the Reynolds number up for future research would not be possible with this device. Aerodynamic force generated for this specimen was also the smallest of the three devices making it the least desirable in this regards.

One benefit of this device was the ease of flow visualization with dye injection. Test models were available which introduce dye at the airfoil surface while it was also possible to inject dye upstream for other prototype models. Images can be captured easily through the clear sidewalls of the device for qualitative flow analysis. An example flow visualization conducted during facility assessment is displayed below in Figure 5-3.
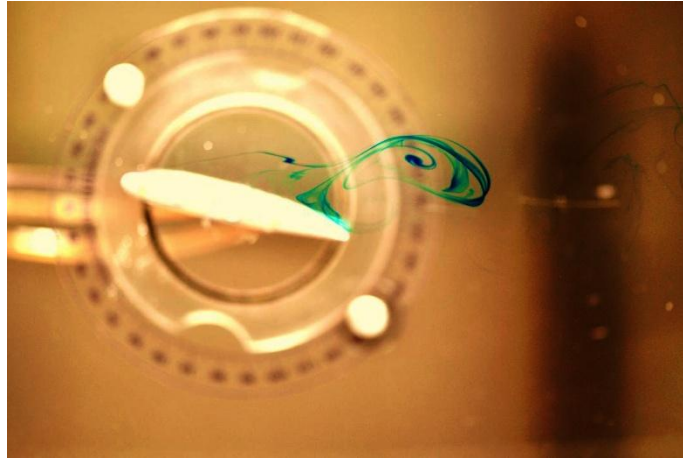
Figure 5-3: Water Tunnel Flow Visualization

5.3.3 Tow Tank

One benefit of the tow tank was its flexibility for tow speed. Modifications of gearing and motor frequency allow the speed to be set as desired. However, the tow tank has a finite test section since the airfoil would traverse the length of the tank then required to be reset. During motion, the airfoil must accelerate from rest to the desired velocity then decelerate before coming to a complete stop at the end of the tank. Considering this motion yields an effective smaller test section since only the region of constant velocity would be of interest. Translating the airfoil with the available equipment would also generate vibrations from the gear and coiled rope which was undesirable as these vibrations may disturb the flow over the airfoil. Flow visualization could be completed with the tow tank as well but could prove difficult with the airfoil traversing through the tank as previously mentioned.

After evaluation, the wind tunnel was chosen to house the Pitch-Plunge Fixture (PPF). This device was most capable of satisfying requirements and aided manufacturing more than the other two devices. The next step was to consider the PPF in more detail in regards to defined motion.

5.4 Control Options

5.4.1 Plunge Motion

Several options were visited to control the motion of pitch and plunge before a method was selected. Three options were considered for the plunge degree of freedom: linear actuator, cam with DC motor, and electronic shaker. Each method had its benefits and pitfalls.

The linear actuator provides a controllable linear translation. With the proper actuator, feedback could also be utilized to better control the prescribed motion. The high speed required for this fixture was quite high for typical actuators and lead to extreme costs to attain an appropriate specification.

Designing a cam which attached to a DC motor to provide the plunge motion was also considered. This option would allow easy control of the frequency by adjusting the voltage applied to the motor. However, the offset required to provide the displacement would create an imbalance on the rotating assembly which was undesirable and therefore disregarded.

A third option considered was using an electronic shaker to generate the plunge motion. Most available shakers are used for high frequency/low amplitude excitations and therefore not suited for this application. After some research, it was found that a long stroke shaker already owned by our Dynamic Structures and Controls Lab met the frequency and plunge range specifications required for this fixtures motion. This shaker was an APS Model 113 Long Stroke Shaker.

5.4.2 Pitch Motion

For the pitch degree of freedom, two options were considered: rotary actuator and rack and pinion.

The rotary actuator, as with the linear actuator, would serve well if feedback were required. The actuator would also allow pitch to be prescribed in a different phase relationship with the plunge motion if desired.

The beauty of the rack and pinion configuration was the plunge and pitch frequency were forced to be equivalent since the pinion gear would be controlled by the plunge rack. Since we were assuming the frequencies for pitch and plunge are the same while also being in phase, this is the simplest mechanism available. Using a rack and pinion to control the pitch motion was chosen for its simplicity. This approach does not preclude alteration to a different approach if necessary for phasing control.

Choosing a pinion gear was directly related to the plunge amplitude in order to achieve the proper pitch angle. The relationship between plunge amplitude and pitch angle was

$$\theta_p = \frac{Y}{P_r} \qquad \text{(Eq. 9)}$$

where Y is the plunge amplitude, P_r is the pinion gear radius and θ_p was the pitch angle in radians.

If a different pitch angle were desired for the plunge displacement, a proper radius pinion gear could be chosen or manufactured if not commercially available.

After the decision was made to utilize the electronic shaker and rack and pinion setup for the assumed degrees of freedom, a structure to house the components was designed.

5.5 Fixture Manufacturing

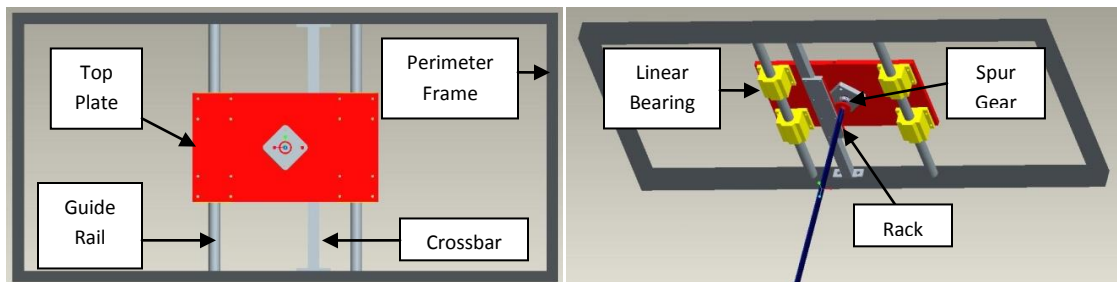Figure 5-4 below displays a model of the Pitch-Plunge Fixture minus the shaker which will be displayed later.

Figure 5-4: Model of Pitch-Plunge Fixture Top (left) and Bottom (right) View

In Figure 5-4 you can see the different components displayed in various colors. The following section steps through the assembly process and gives detail on individual components.

Constraining the plunge degree of freedom was completed with polished guide rails and closed pillow-block linear ball bearings. A hardened precision steel shaft with 2.54cm diameter is used for the guide rail. The bearings chosen allowed for a small misalignment (≈1°) of guide rails while maintaining smooth linear motion. These guide rails and linear bearings were purchased from McMaster Carr and are displayed in Figure 5-5. The guide rails were required to be machined to length and tapped on each end to allow attachment to the perimeter frame. One benefit and reason for choosing the pillow block linear bearing is the mounting holes already present allowing for additional components to be attached.

a.

b.
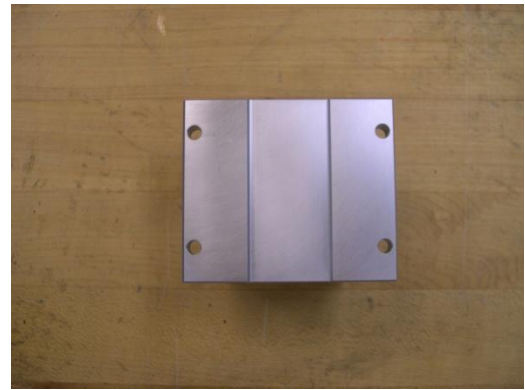
c.

Figure 5-5: Guide Rail (a) and Linear Bearings (b,c)

Sitting atop the pillow block linear bearings is the top plate to attach the pitch ball bearings for the airfoil shaft and pinion gear. Figure 5-6 displays the top plate (left) and pitch bearings (right). Dimensions of the aluminum top plate are 40.64cm long x 24.13cm wide x 1.27cm thick. The pitch bearings were placed above and below the top mounting plate in 7.62cm x 7.62cm aluminum blocks 2.54cm thick to space the bearings and reduce misalignment of the airfoil shaft. These pitch ball bearings accept a 0.95cm diameter rod and are pressed in aluminum blocks allowing them to be attached to the top plate.   The hole centered in the top plate allows the pitch rod to pass perpendicular through the plate and extend down into the wind tunnel. Four holes around the center hole shown in the dashed red square allow the pitch bearing blocks to be bolted to the top plate. The remaining square hole (shown in green dashed squares) patterns in each corner are used to attach the top plate to the pillow block linear ball bearings.
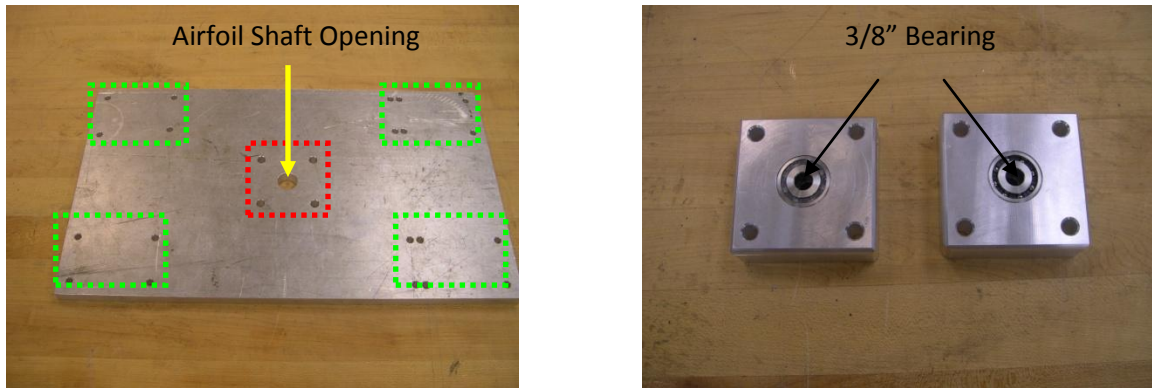
Figure 5-6: Top Plate and Pitch Bearings

The rack portion of the rack and pinion has a diametral pitch of 48 and is attached to a crossbar. This rack was purchased from Stock Drive Products/Sterling Instruments. The crossbar is constructed of 2.54cm square steel tubing with flanges welded to each end for attachment to the perimeter frame. The flanges are bolted into a slot cut in the perimeter frame allowing adjustability to accommodate varying size gears.

The left image in Figure 5-7 shows the complete assembly of the crossbar and rack. On the right, a close up view of the rack gear is shown to better represent the teeth.
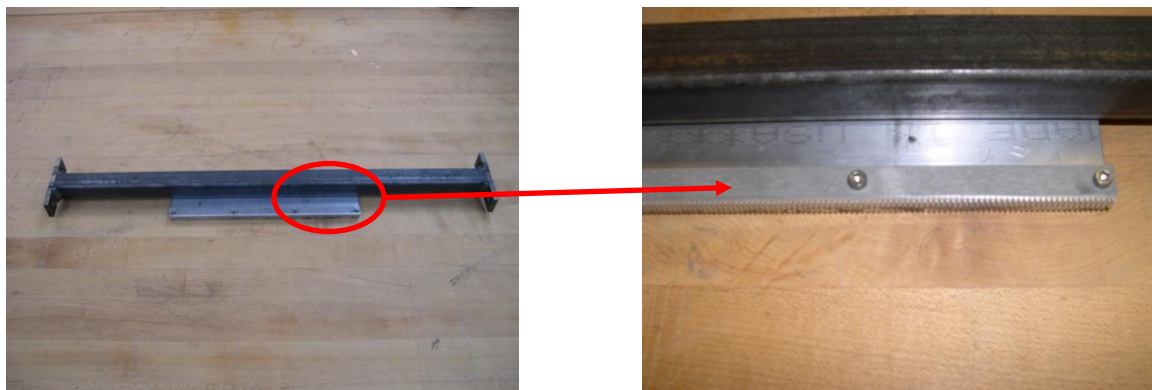
Figure 5-7: Crossbar and Rack Gear

The airfoil shaft was constructed to have the airfoil and pitch gear attached to it. A slot was milled into the end of a hardened steel rod the same thickness as the airfoil and 3.81cm deep. There was also a flat portion machined into the steel rod allowing a set screw to be attached for the pitch gear. Two 0.32cm holes drilled through the slot also allowed the airfoil to be attached to the shaft. Figure 5-8 shows the shaft with the

milled slot and flat face to seat the set screw. Figure 5-9 shows a better angle for the 0.32cm holes to attach the airfoil.

Airfoil Milled Slot

Set Screw Flat
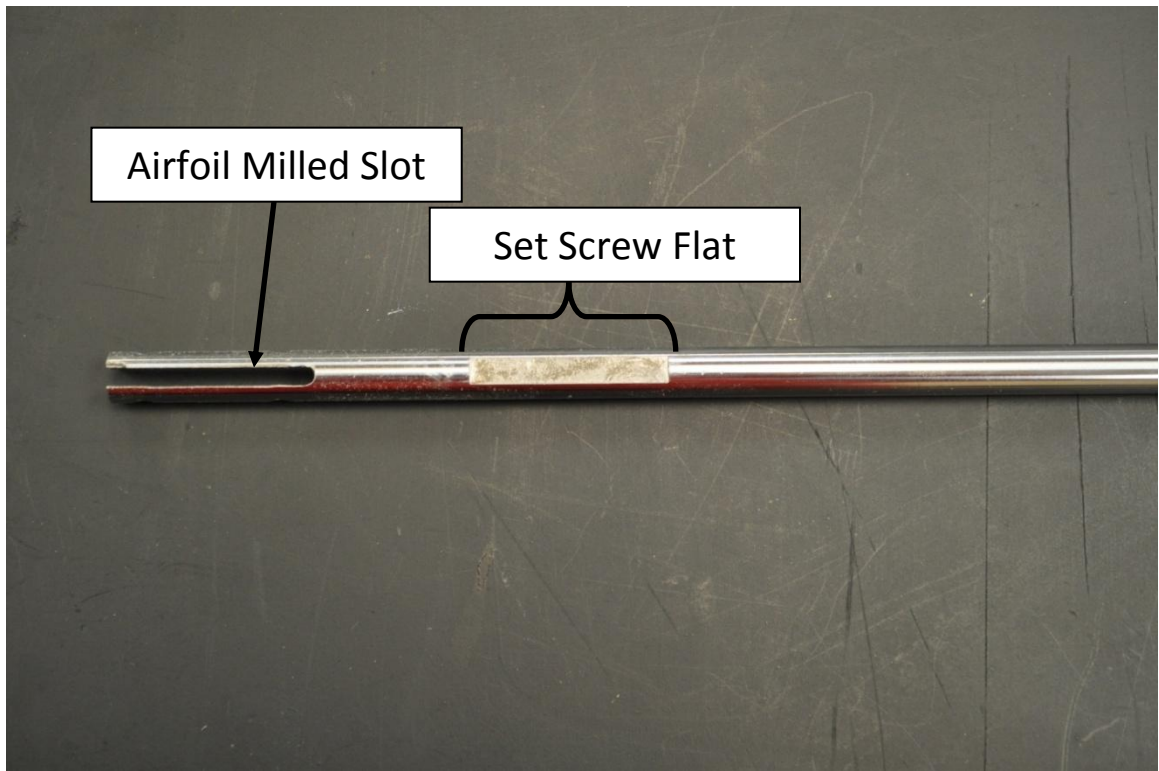
Figure 5-8: Airfoil Shaft Front View

Airfoil Bolt Holes
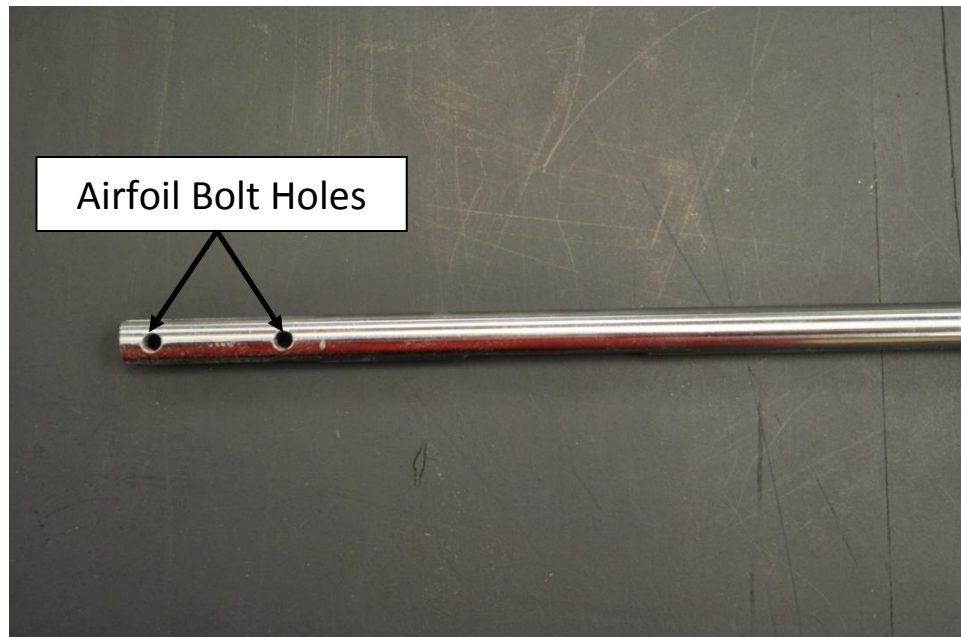
Figure 5-9: Airfoil Shaft Top View

With the airfoil shaft machined, the pitch gear was then attached and seated with the set screw shown in Figure 5-10.
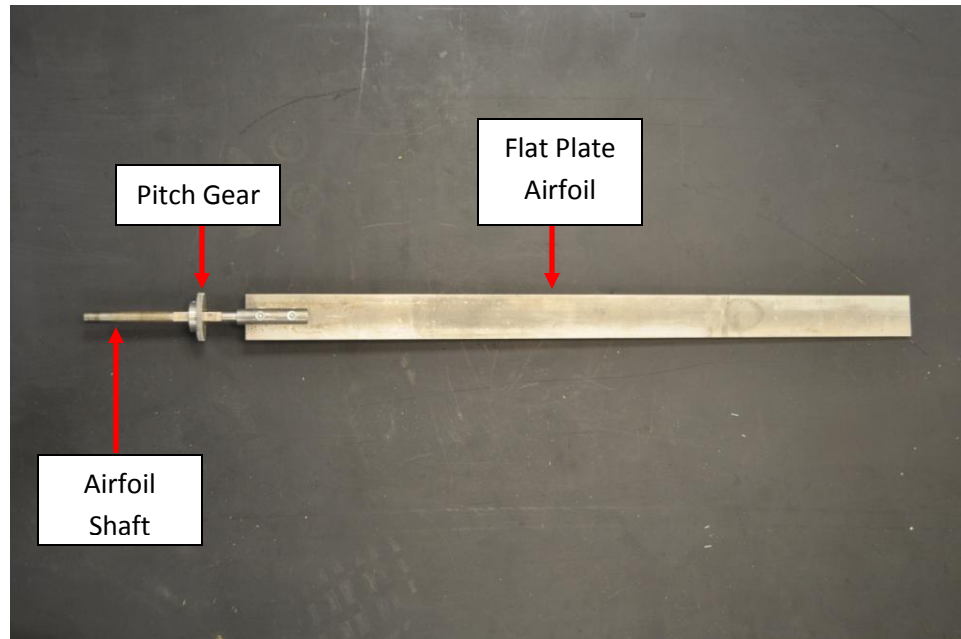
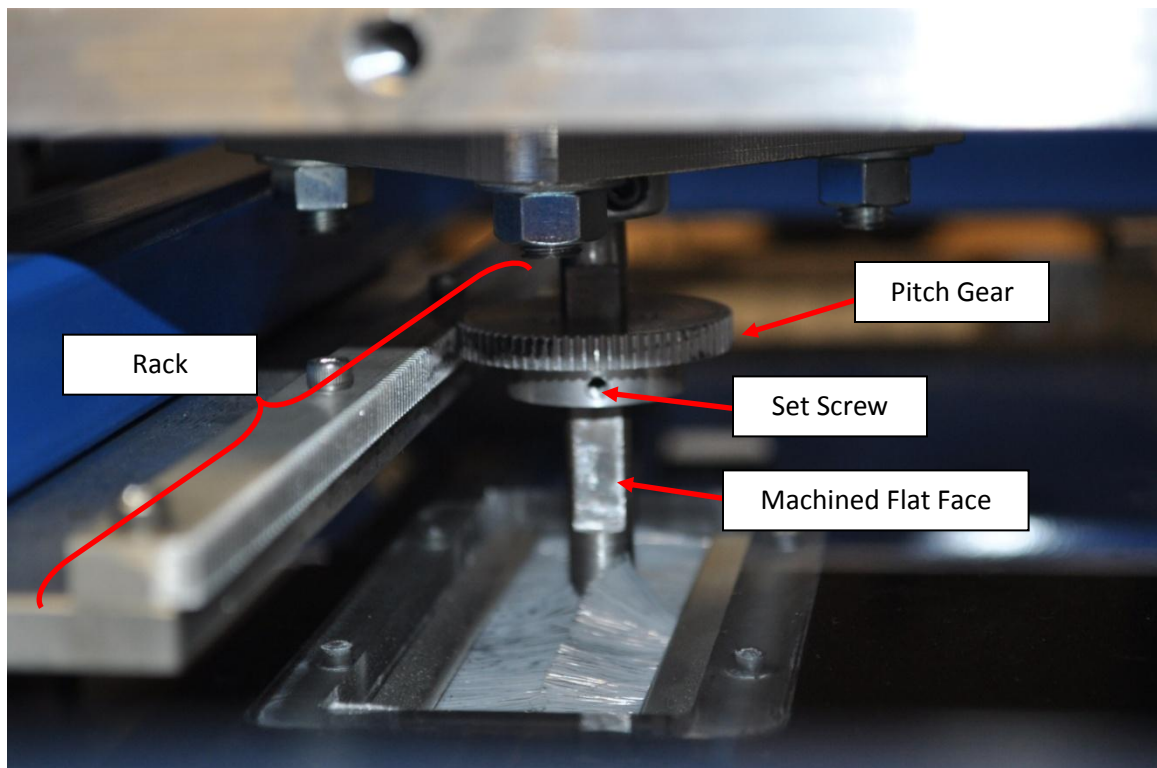Figure 5-10: Airfoil Shaft with Airfoil and Pitch Gear Attached

Figure 5-11: Pitch Gear Mounted on Airfoil Shaft

Figure 5-11 displays the pitch gear mounted onto the airfoil shaft and also installed into the wind tunnel. This angle also depicts the set crew location which tightens onto the flat face previously machined to constrain the gear to the shaft.

With the components manufactured, the fixture was assembled before being placed in the wind tunnel. The foundation of the fixture is the perimeter frame which has all the components attached to it and ultimately attaches to the wind tunnel. The guide rails with two pillow block linear ball bearings attached to each were first bolted into place.
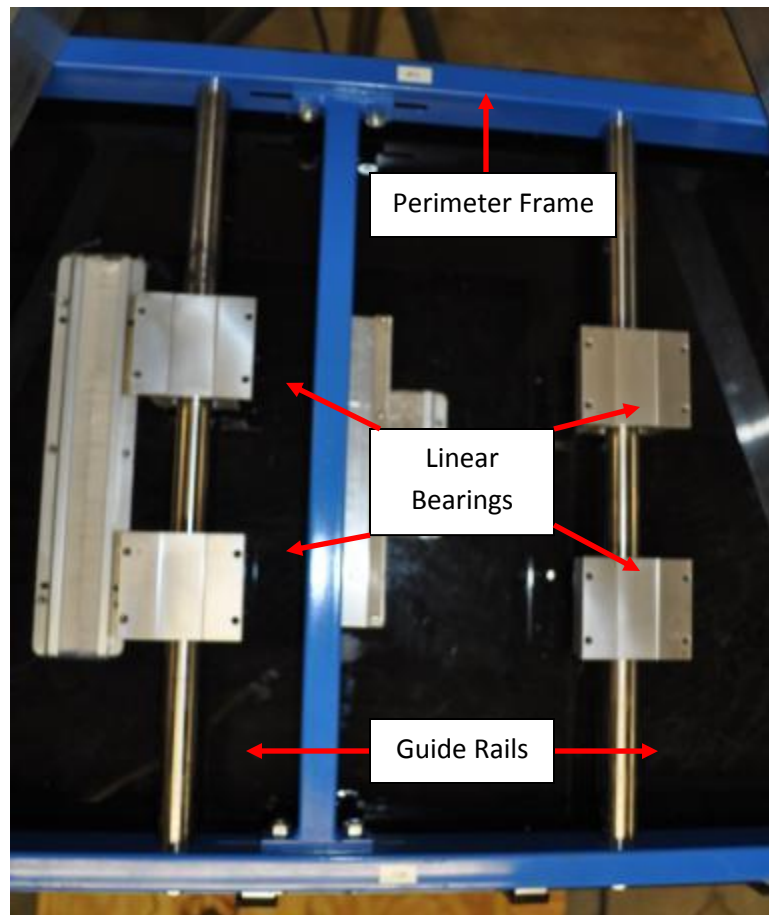
Figure 5-12: Perimeter Frame with Guide Rails and Linear Bearings

Next, the crossbar with rack was attached followed by the top plate and pitch bearing blocks. Crossbar attachment was accomplished with two 9.5mm bolts on each end and shown in Figure 5-13.
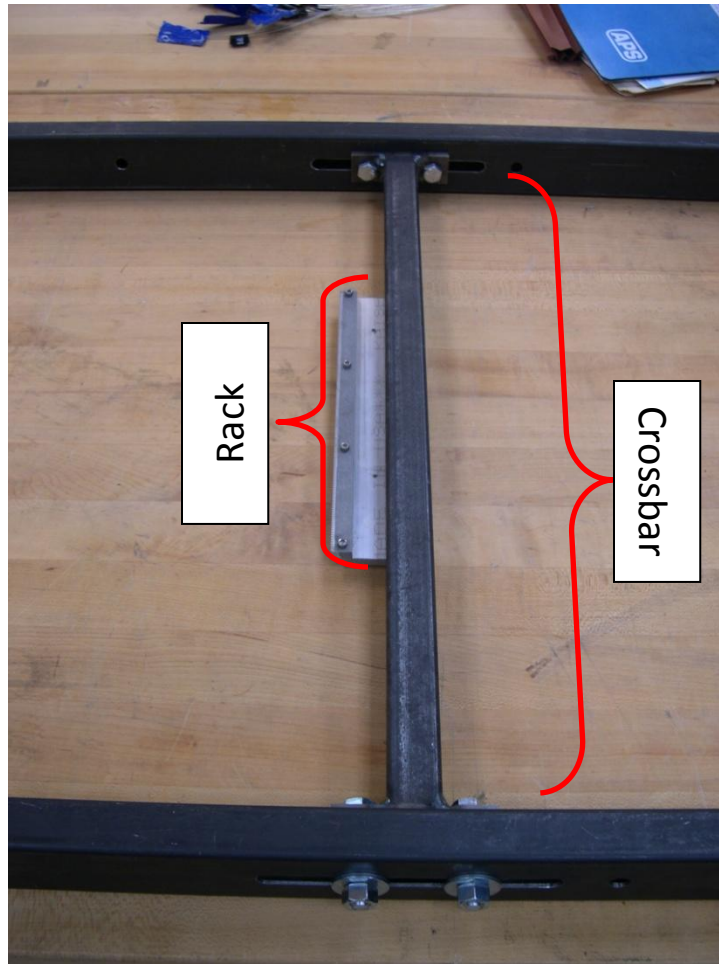
Figure 5-13: Crossbar Attached to Perimeter Frame

The top plate was bolted firmly onto the linear bearings while leaving the pitch bearing blocks loosely tightened. Before tightening the pitch bearings firmly, a 9.5mm-diameter rod was placed through both bearings to ensure alignment of the top and bottom pitch bearings.
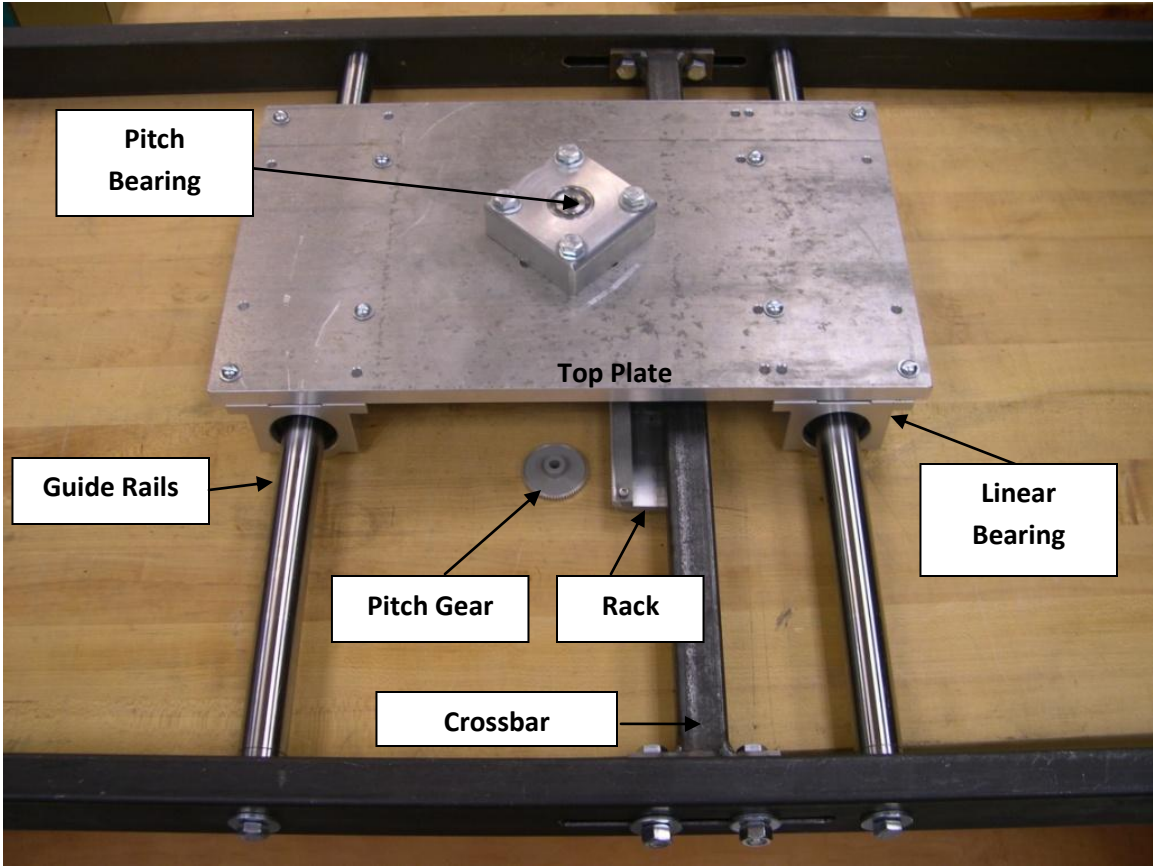
Figure 5-14: Complete Dynamic Fixture Assembly

With everything attached to the perimeter frame and shown in Figure 5-14, the fixture was mounted onto the wind tunnel. Attachment to the tunnel was accomplished with seven 6.3mm bolts through the front and rear of the fixture to the flange of the wind tunnel shown in Figure 5-15.
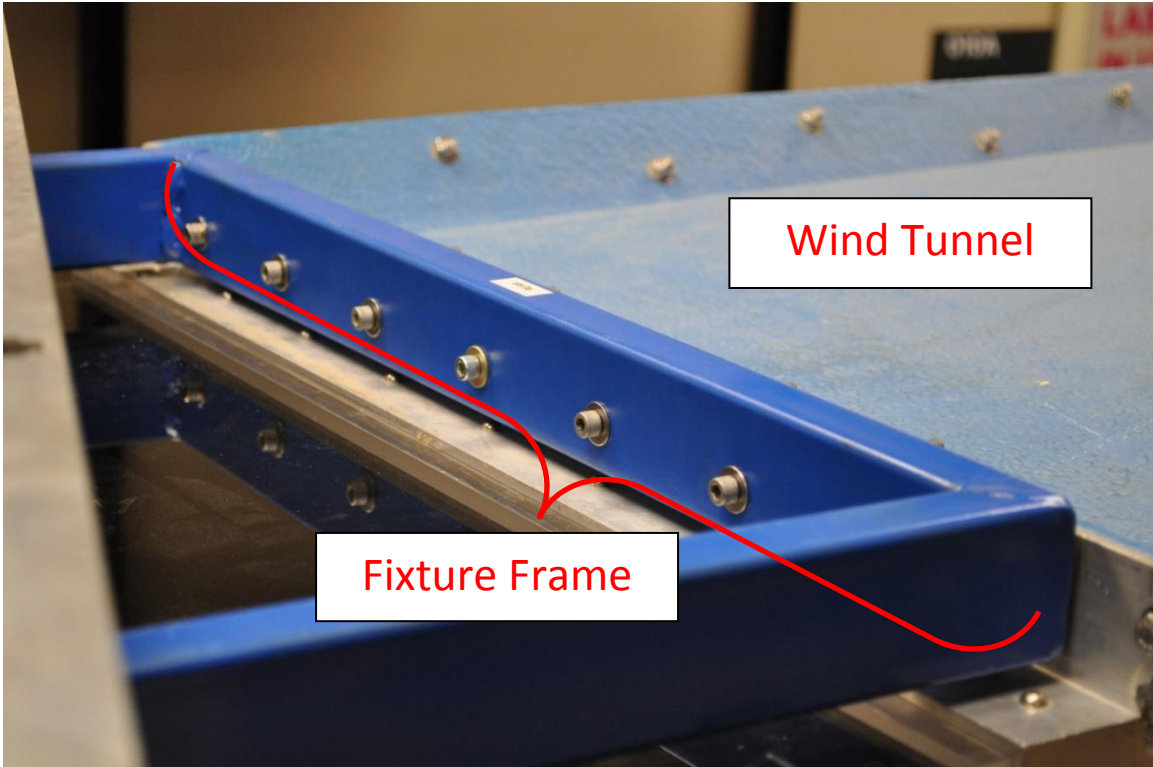
Figure 5-15: Fixture to Wind Tunnel Attachment

The APS 113 shaker was supported vertically with a heavy duty tripod and constrained to the wind tunnel with additional bracing. The 2.54cm x 7.62cm additional aluminum bracing attached to the sides of the shaker and spanned across the width of the fixture. This helped reduce the relative motion of the shaker with the fixture and can be seen in Figure 5-16. Without these braces, the shaker could move in relation to the fixture leading to inaccurate plunge and pitch displacement of the wing model.
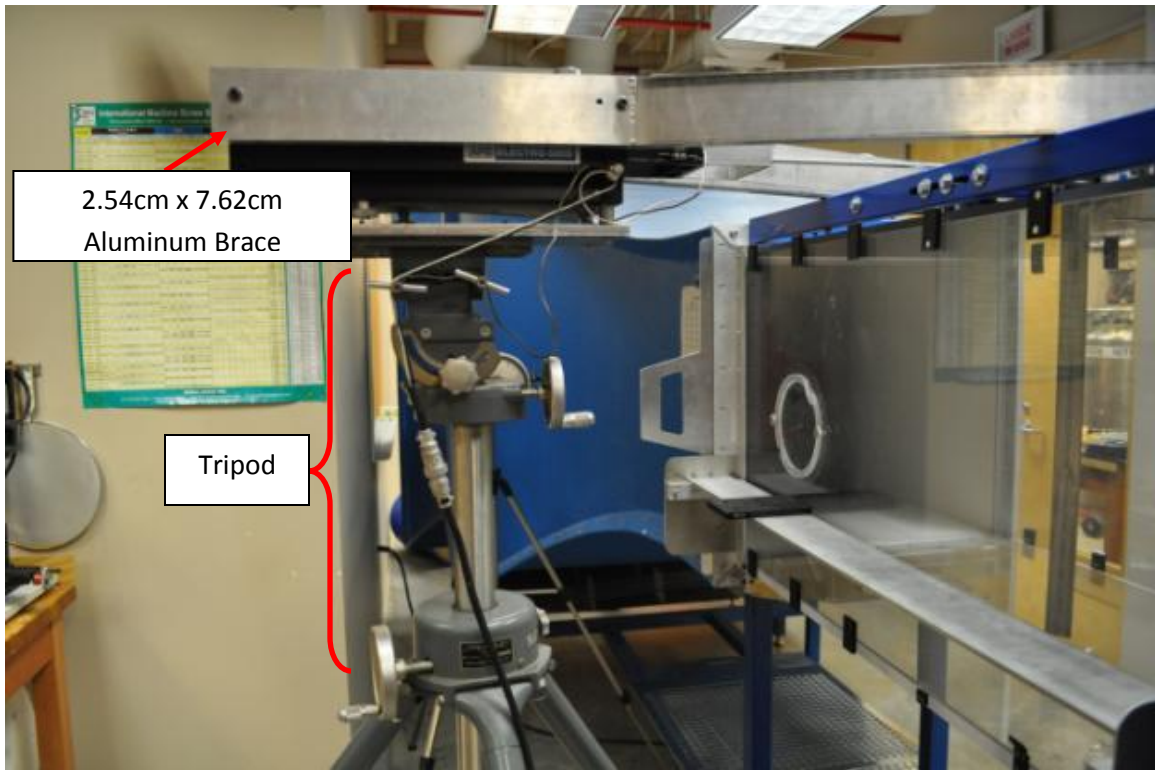
Figure 5-16: APS Long Stroke Shaker Support

Connecting the shaker to the top plate was accomplished with a steel rod threaded into the side of the top plate along with nuts and washers tightened onto a shaker bracket, Figure 5-17.
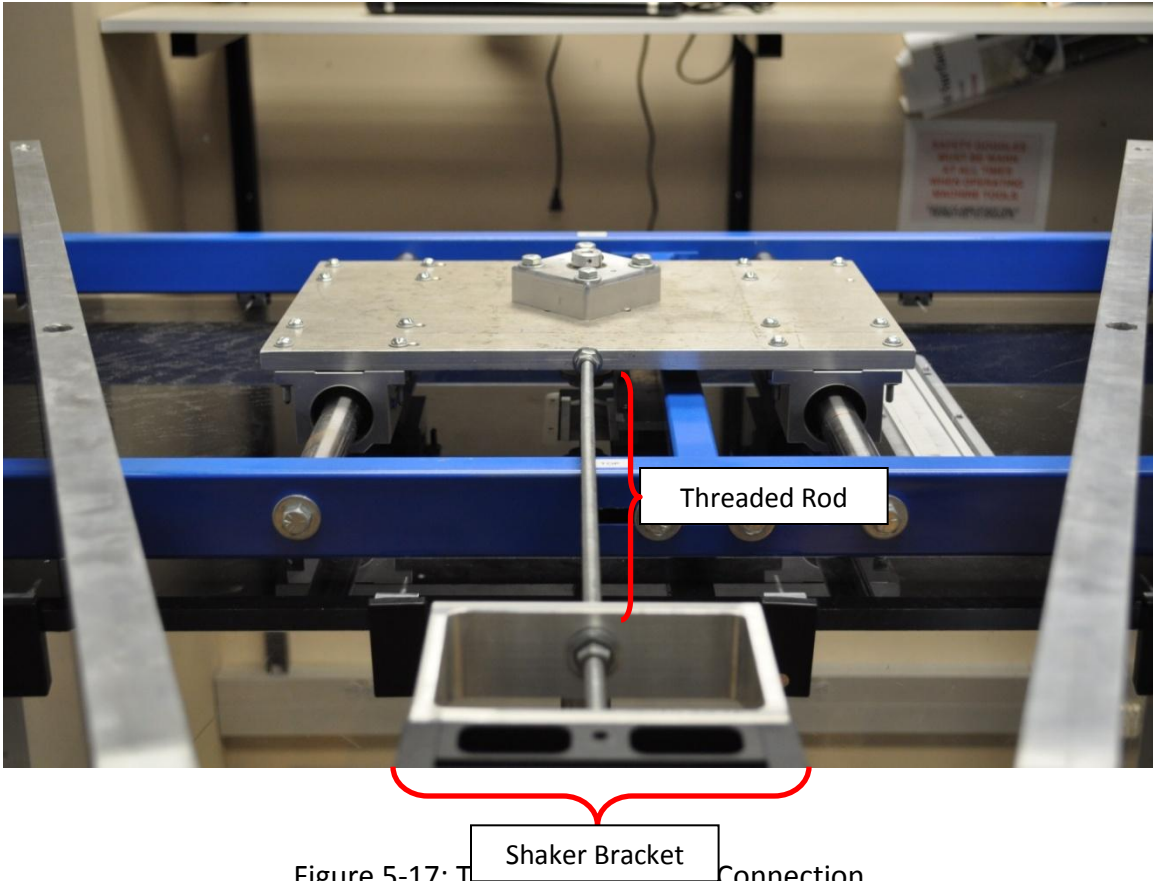
Figure 5-17: Top Plate to Shaker Connection

With the fixture frame completed, the airfoil test model was created. Specifications have been given previously for the maximum size and desired Reynolds number. Since the fixture is oscillating, care had to be given to the steady state response of the mounted model. The model is mounted in a cantilevered scenario and oscillating at a frequency dependant on Strouhal number. Since the wind tunnel minimum speed of 1m/s was selected, this speed was used for determining Reynolds and Strouhal number.

To reduce tip deflection of the model it was designed to have its first natural frequency to be at least twice the plunge frequency specified by the Strouhal number. This was an extremely important design criterion which was discovered after the first test model was found to have its first natural frequency near the plunge frequency. If this was not avoided, the model could deform severely out of plane under steady state response and cause 3D flow effects. Equation 10 was used to determine the first natural frequency for the cantilevered airfoil (Thompson, 1993).

$$f_1 = \frac{1.875^2}{2\pi}\sqrt{\frac{EI}{\rho_m l^4}} \qquad\qquad \text{(Eq. 10)}$$

Where E=Young's Modulus of Elasticity (Pa), I=Inertia (m^4), ρ_m=Mass density (kg/m), and l= Length (m).

A spreadsheet comparing the first natural frequency (Eq. 10) of aluminum test articles against the frequency specified by St = 0.2 (Eq. 2) is summarized in Table 5:**3**.

Table 5:3: Cantilevered Beam Natural Frequency

Chord (m)	Length (m)	Thickness (m)	1st f_n (Hz)	Plunge Frequency (Hz)	f_1/Plunge Freq	Reynolds #
0.025	0.61	0.0048	10.4	7.87	1.33	1618
0.027	0.61	0.0048	10.4	7.41	1.41	1719
0.029	0.61	0.0048	10.4	7.00	1.49	1820
0.030	0.61	0.0048	10.4	6.63	1.58	1921
0.032	0.61	0.0048	10.4	6.30	1.66	2022
0.033	0.61	0.0048	10.4	6.00	1.74	2123
0.035	0.61	0.0048	10.4	5.73	1.82	2225
0.037	0.61	0.0048	10.4	5.48	1.91	2326
0.038	0.61	0.0048	10.4	5.25	1.99	2427
0.040	0.61	0.0048	10.4	5.04	2.07	2528
0.041	0.61	0.0048	10.4	4.85	2.16	2629
0.043	0.61	0.0048	10.4	4.67	2.24	2730
0.044	0.61	0.0048	10.4	4.50	2.32	2831
0.046	0.61	0.0048	10.4	4.34	2.41	2932
0.048	0.61	0.0048	10.4	4.20	2.49	3033
0.049	0.61	0.0048	10.4	4.06	2.57	3135
0.051	0.61	0.0048	10.4	3.94	2.65	3236

Length of the model was fixed to 0.61m to match the wind tunnel cross section. The chosen model, shown in Figure 5-18, was 0.61m long, 0.038m chord, with a thickness of 0.0048m. A common thickness was chosen since it met our criteria of natural frequency being at least twice the plunge frequency and was easily available from a materials distributer.
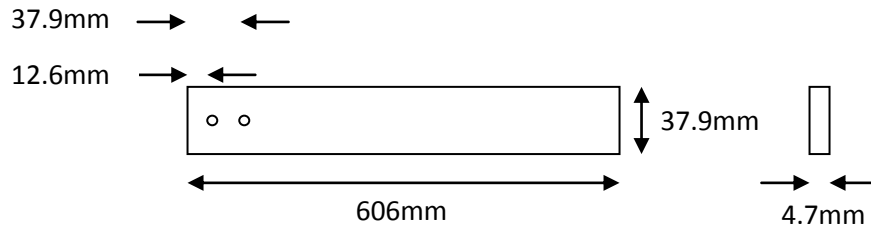
Figure 5-18: Wind Tunnel Flat Plate Airfoil Model

With model dimensions specified, the scaling parameters of Reynolds and Strouhal number were revisited to define final Reynolds number and plunge frequency. Applying the 0.038m chord and 1.0m/s fluid velocity of the wind tunnel to Equation 1, we attain a Reynolds number of 2427. While it does not match the *Re* = 1000 desired, it is well within the range of 1,000-10,000. Required plunge frequency was found to be 5.25Hz using Equation 2.

Recalling the specified pitch angle was +/- 45° with the displacement of +/-0.5c, the proper pinion gear was selected after specifying the test model chord using Equation 8 after converting 45° to radians and inputting the plunge displacement of 0.019m. The proper pinion gear was defined to have a radius of 0.024m and was purchased from Stock Drive Products/Sterling Instruments.

5.6 Experimental Setup

Flow visualization in the wind tunnel was accomplished by seeding the incoming air with fog while illuminating the flow at the test section with a laser sheet. Seeding the air was accomplished with a SAFEX F2010 fog generator which was placed at the inlet of the wind tunnel. To maintain consistent flow, the fog generator fed into an accumulation chamber which was then plumbed with a hose and adjustably powered inline fan used to pull the accumulated fog into the wind tunnel inlet. This setup is displayed in Figure 5-19.
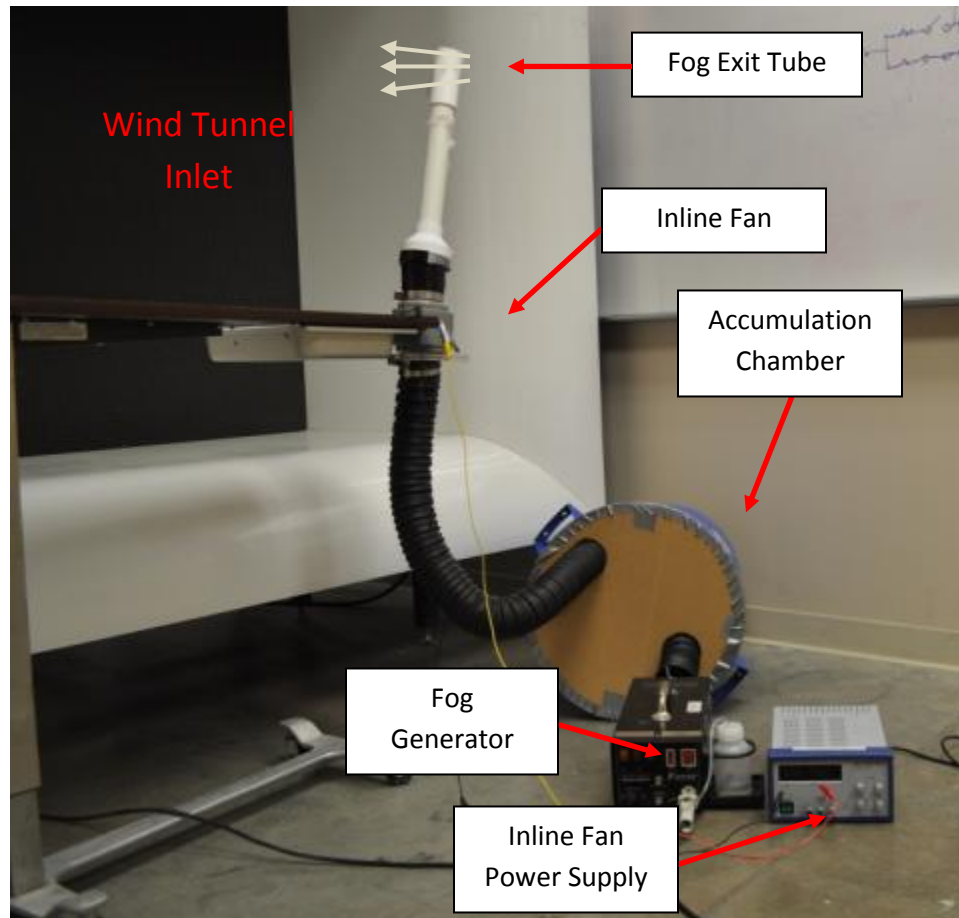
Figure 5-19: Fog Injection Experimental Setup

Having the fog exit from the tube made it easy to adjust fog position at the wind tunnel test section around the airfoil model. This was important in allowing enough fog to be illuminated by the laser sheet, but not too much which could make capturing images through fog difficult.

The laser utilized to illuminate the flow was an ELFORLIGHT L400Q with a 532nm wavelength. Controls for the laser were set at 1,000Hz pulse rate with a current of 16 amperes. Converting the laser beam to a horizontal light sheet was accomplished with a 9mm diameter, 30° fan Powell lens purchased from Edmund Optics. The laser and lens are shown in Figure 5-20 along with a close up image of the Powell lens in Figure 5-21.
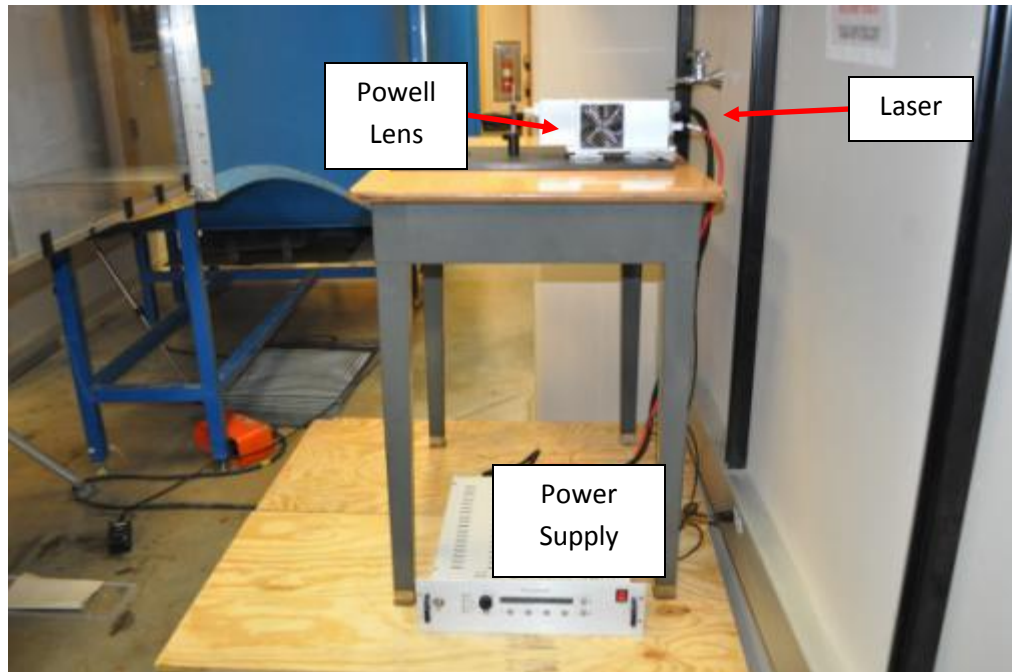
Figure 5-20: ELFORLIGHT L400Q Laser and Power Supply
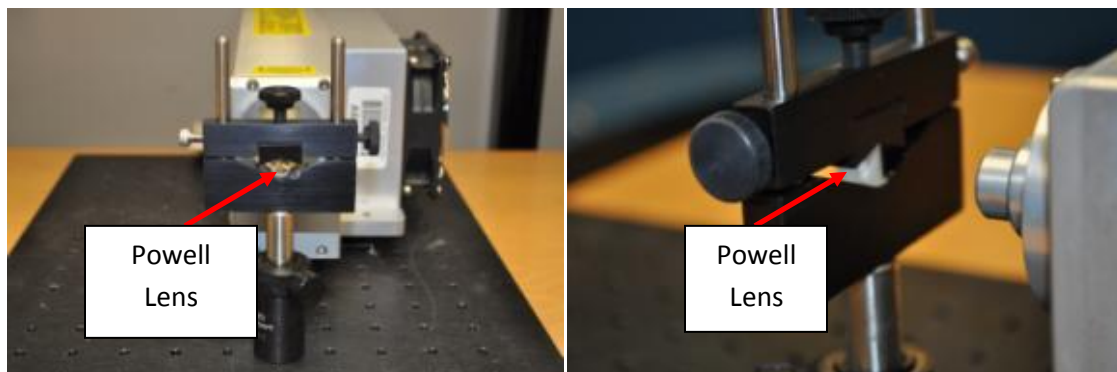
Figure 5-21: Powell Lens

Capturing images for the wind tunnel flow visualization turned out to be quite difficult. This scenario had a high speed, low light, and small depth of field which made it difficult to develop good, clear images. Typically, with low light a slow shutter speed is used to expose the image. However, a slow shutter speed blurred the image, making flow structures very difficult to identify. The key in taking these images clearly lay in choosing the proper lens and creating as bright of a laser sheet as possible, along with a fast shutter speed. A Nikon 50mm fixed focal length lens with an f-number of 1.4 was chosen to capture these images. The low f-number has a larger aperture allowing more light in while capturing images. To illuminate the flow better, the laser was turned to its

highest current setting of 16 amperes. Combining the brighter laser sheet with the low f-number lens and a shutter speed of 1/500s allowed clear images to be taken.

Plunge motion of the fixture was provided with the APS 113 long stroke shaker. Signal input to the shaker was provided by a function generator connected to the shaker's amplifier and an oscilloscope. The oscilloscope provided a more accurate readout of the function generator's input signal frequency. Amplitude of the function generator's signal was not enough to create the desired plunge displacement of the fixture; therefore, the function generator provided a sinusoidal signal of the proper frequency while the amplifier was utilized to reach the desired displacement.
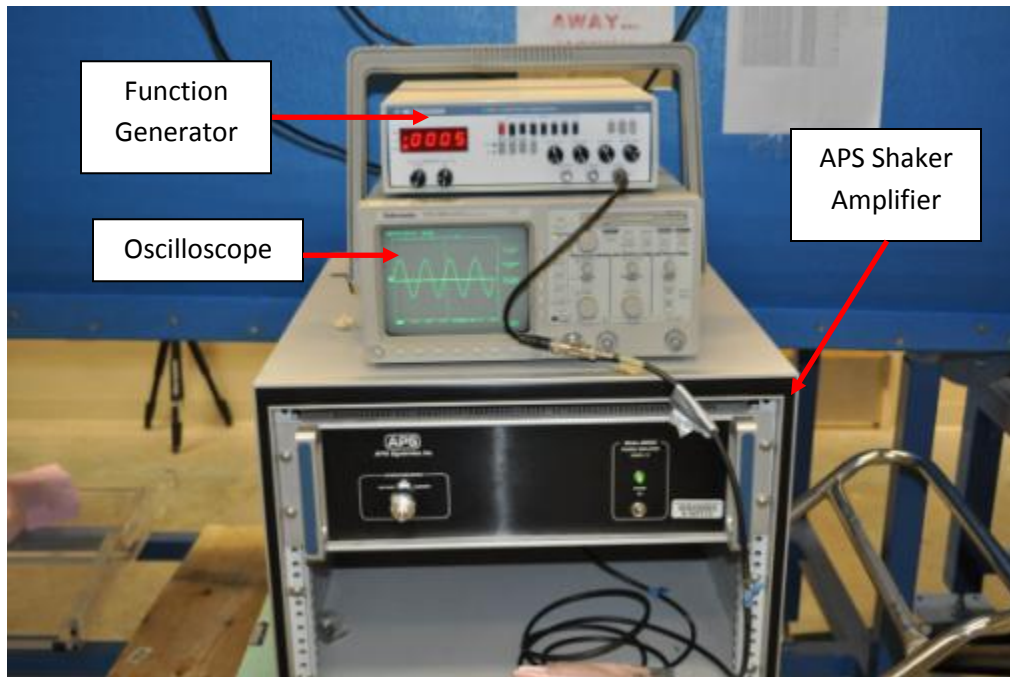
Figure 5-22: Function Generator, Oscilloscope, and Shaker Amplifier

5.7 Fixture Validation

Before gathering data with the dynamic fixture, the motion produced first had to be validated. Validation included inspection of fluid speed, airfoil displacement, and rotation. Validation of fluid speed was completed while investigating the wind tunnel for its feasibility to house the fixture. A schematic displaying the experimental setup to monitor wind speed is shown in Figure 3-4. To monitor the plunge displacement of the fixture, a Keyence LK-503 laser displacement sensor was used along with National Instruments LabVIEW 2010 software for capturing the data.

With a reflecting bracket attached to the top plate and the displacement laser clamped to the fixture frame as shown in Figure 5-23, the fixture was operated to document the plunge displacement. Displacement was desired to be +/- 0.5c which was dependent on the constructed airfoil of Figure 5-18 and gave a displacement of +/- 0.019m.
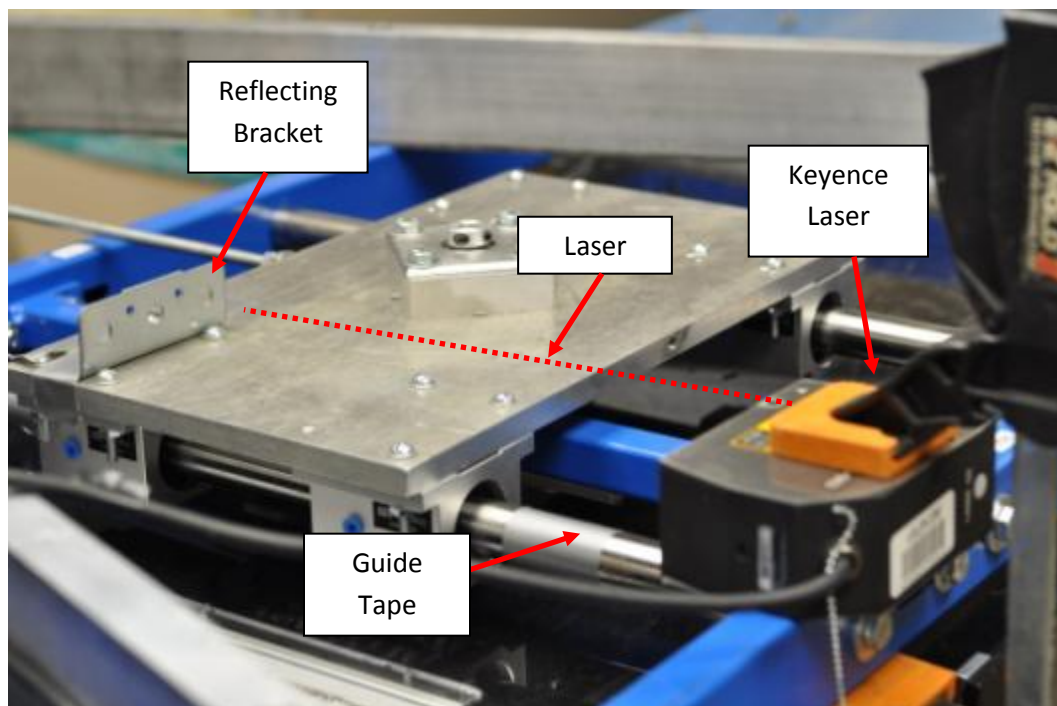
Figure 5-23: Keyence Displacement Laser Setup

Data gathered from the displacement experiment is represented below in Figure 5-24. Once the proper displacement was reached, tape was placed on the guide rails as shown in Figure 5-23 as a gauge for further experiments so the laser could be removed. Figure 5-24 has time in seconds as the horizontal column with displacement in meters in the vertical column. Data was sampled at a rate of 100Hz allowing for accurate frequency identification.
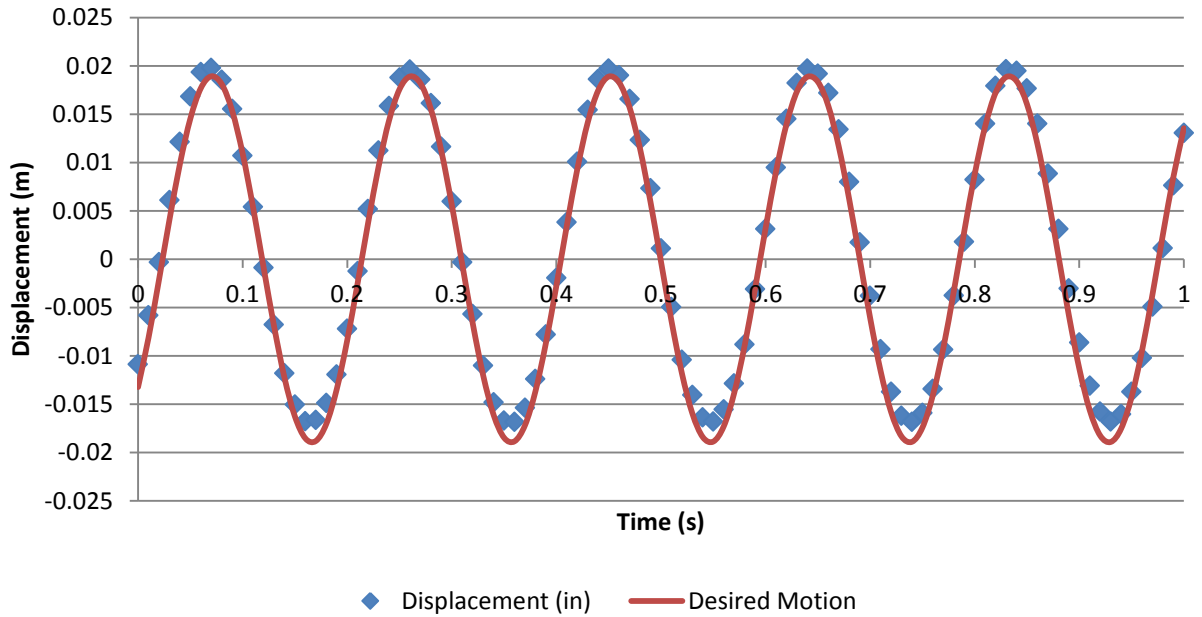
Figure 5-24: Plunge Displacement Data

The maximum displacement of collected data from the plot is 0.0197m and the minimum is -0.0168m. Taking the absolute value average of these values gives a mean displacement of +/- 0.018m which is very close to the specified displacement of +/- 0.019m, which matches +/- 0.5c. Pitch rotation is dependent on plunge displacement due to the rack and pinion setup. Since the plunge displacement was acceptable and the pinion gear was sized according to plunge displacement, the pitch angle was assumed acceptable as well.

Frequency of oscillation was obtained by recording the time at the first and last peak displayed in Figure 5-24. Time at the first peak was 0.06s and the last peak was 0.82s. The time difference here is 0.76s which accounts for four periods of oscillation.

$$f = \frac{n}{\Delta T}$$
(Eq. 11)

Where n= number of periods. Using Equation 11, a frequency of 5.26Hz is obtained which matches our desired frequency of 5.25Hz from St = 0.2 very well.

The solid line in the plot represents the desired motion using Equation 12 with f= 5.25Hz and c=0.038m.

$$y = y_0 + \frac{c}{2}\sin(2\pi f t + \varphi)$$
(Eq. 12)

76

The desired motion data points were used to compare the recorded displacement of the PPF for further validation. Over a time period of 1s, standard deviation between the recorded displacement and desired motion plot was 0.001m which is 5.2% of the desired amplitude of motion. Data for this comparison is displayed in the Appendix.

At this point the fixture and test model had been constructed along with the wind tunnel speed and fixture displacement validated; therefore, data was gathered.

Chapter 6 : Dynamic Flow Visualization Results

6.1 Phase Repeatability

Data was collected for dynamic flow visualization in the form of many still images. With the images collected, they were grouped according to the phase representation shown in

Figure 5-2. These phases were chosen since they are moments in time where the airfoil changes plunge and pitch direction. Figure 6-1 displays multiple images captured for Phase 2 for comparison.

In each image of Figure 6-1 you can see the pitch angle is positive with respect to horizontal and similarly sized vortices are developed on the lower side of the airfoil. It is important to notice that slight differences may exist in pitch angle due to images being triggered manually; however, the phase is still a moment in time with the same motion dynamics of positive plunge and pitch displacement.
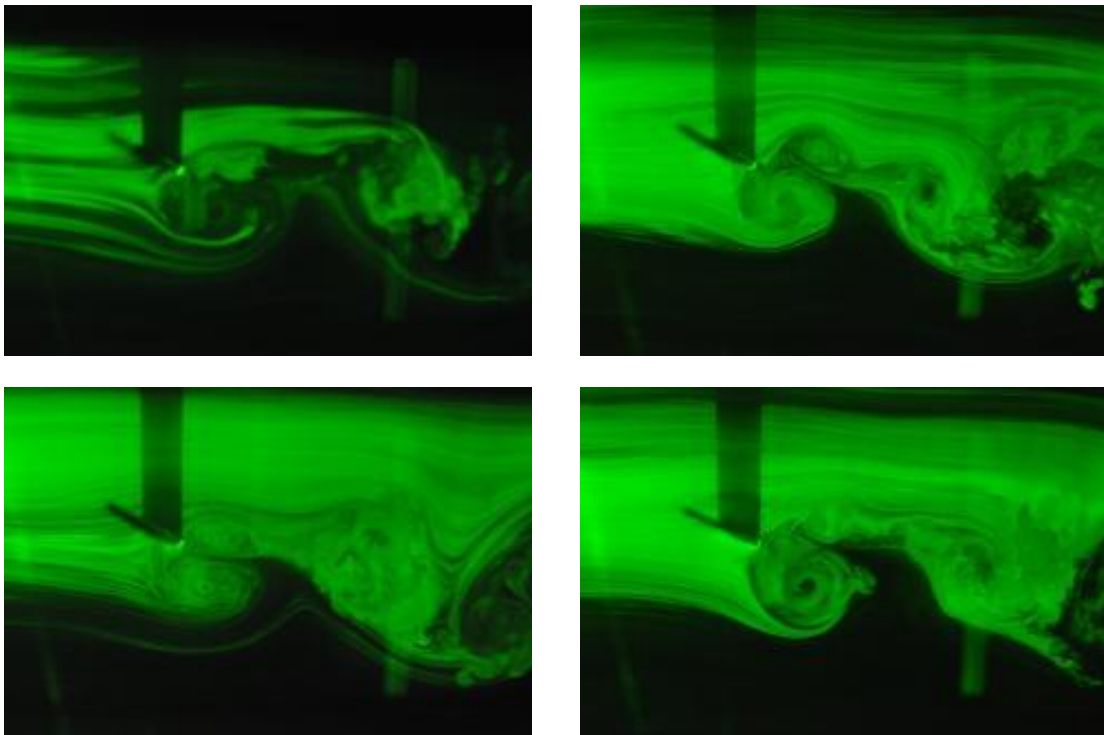
Figure 6-1: Phase 1 Flow Visualization Images

6.2 Complete Motion Results

From Figure 6-1, it was established the flow structures are repeatable between different images; therefore, only one image will be used to represent each phase for comparison of flow structure development. While many images were captured, those in Figure 6-2 were chosen due to the fact they were captured at the right time to represent the given phase while being clear enough to document vortex and flow structure formations around the pitching and plunging airfoil. Each individual image is labeled underneath of its respective phase. The shadow visible in the upper portion of the image is created by the airfoil obstructing the laser from illuminating the fog. To make the airfoil phase more clear, the airfoil is highlighted in red to help distinguish the airfoil from the flow.

Phase 1

Phase 2

Phase 3

Phase 4

Phase 5   Phase 6

Phase 7   Phase 8
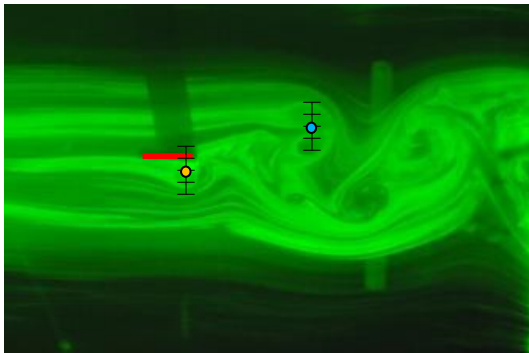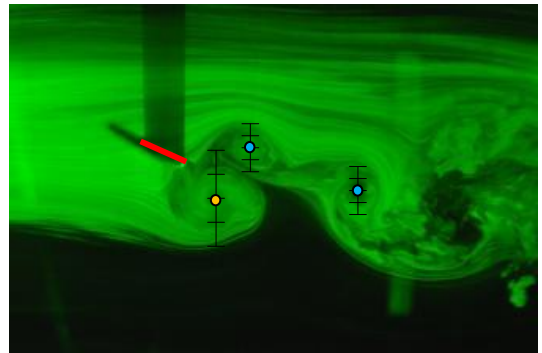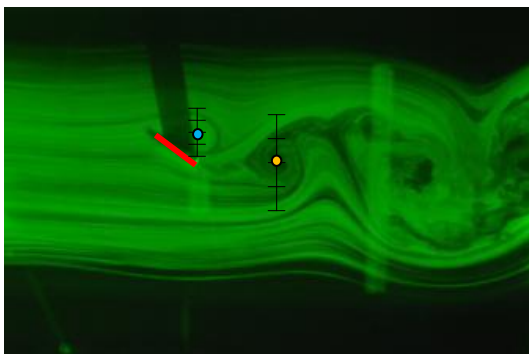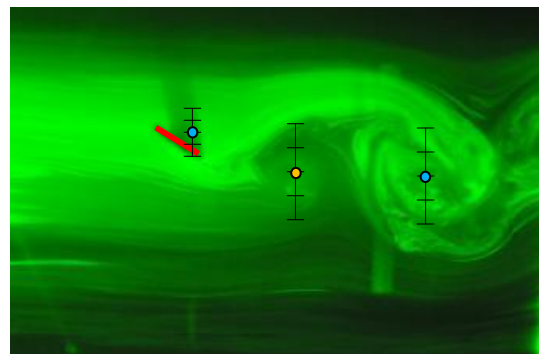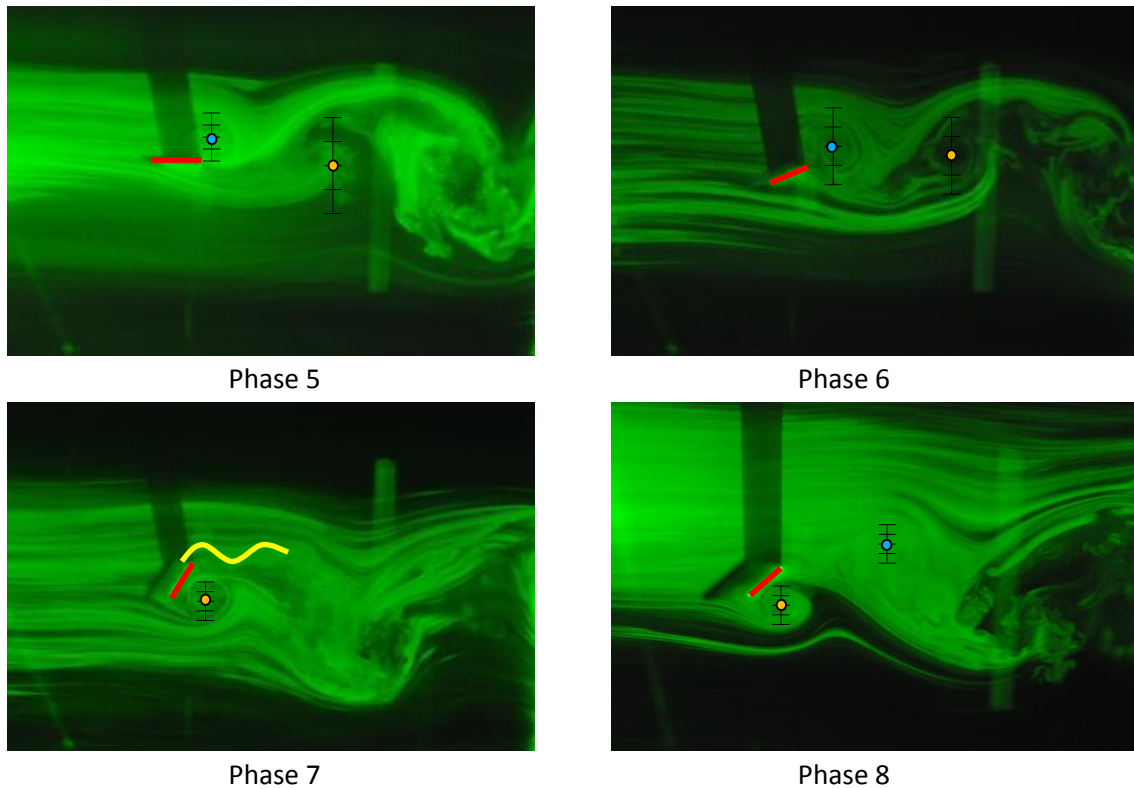
Figure 6-2: Wind Tunnel Flow Visualization Phases 1-8

By following the images in consecutive order you can gain an understanding of how the flow develops. Vortices discussed are indicated with an orange (counter-clockwise spin) or blue (clockwise spin) dot at the center of the vortex with all diameters measured vertically from their center. Phase 1 of Figure 6-2 displays an attached counter-clockwise spinning vortex with a diameter of 0.75c on the underside of the airfoil while streaklines on the top of the airfoil appear to be smooth and remain attached as well. Phase 2 is a slight instant in time later than Phase 1 and has shed the vortex from its bottom surface. At this instant the shed vortex has a diameter of 1.5c. Phase 3 is considered the maximum plunge and pitch displacement. The given image has a clockwise-spinning vortex attached to the top surface with a diameter of 0.75c while the bottom side of the airfoil has attached flow streaklines. Shed vortices can also be seen downstream which are larger in diameter and alternate from top to bottom. The first shed vortex downstream has a counter-clockwise rotation, a diameter of 1.75c and develops from streaklines flowing around the bottom side of the airfoil. At this point, you can take note of vortex spin direction based on which surface (top or bottom) from which it was shed. Clockwise spinning vortices are shed from the top surface of the airfoil, while counter-clockwise spinning vortices are shed from the bottom.

Phase 4 does not represent the top vortex observed in Phase 3 well, but the shed vortex from the bottom is observed more developed and further downstream. In this phase, the shed vortex mentioned in Phase 3 now has a diameter of 2.0c, which is twice that observed in the previous phase. Phase 5 returns back to a pitch angle of 0° but has its plunge displacement downward. A vortex is still attached to the top surface with a diameter of 0.75c.   Also, the downstream shed vortex being followed from Phase 3 and 4 is captured again with its diameter still being approximately 2.0c. It is hard to properly record the diameter since the fog is not distributed uniformly enough to provide a clear boundary of the vortex. Once again, the streaklines passing the bottom of the airfoil are clearly observed to form into the bottom shed vortex and begin to rotate. Phase 6 provides a really nice image of vortex formation on the top side of the airfoil with the boundary of the vortex clearly defined with both vortex streaklines and streaklines passing around the generated vortex. Here the vortex is at the trailing edge of the airfoil and has a diameter of 1.5c. Phase 7 is the minimum plunge and pitch angle of the airfoil motion. A vortex is formed on the bottom side of the airfoil with a diameter of 1.0c. Something to note also occurs at the trailing edge of the airfoil where unsteady streaklines (represented by yellow curve) are generated behind the trailing edge. Phase 8 is the final phase before the motion repeats itself. In this phase, a vortex is attached to the bottom surface with a diameter of 1.0c.   A shed vortex can also be seen downstream with a clockwise spin direction.   Beyond the second vortex seen here, turbulence develops with the flow becoming disturbed and widely dispersed.

Observing the flow structures we can notice common characteristics: 1) vortices form on the back side with respect to plunge direction, 2) shed vortices grow in diameter after being shed, 3) vortex spin direction is dependent on shed side, and 4) the wake of the airfoil becomes turbulent approximately 4c behind the trailing edge. The first characteristic can be seen in each image of Figure 6-2. Phases 1-2 and 7-8 have the vortex located on the bottom of the airfoil while the plunge direction is upward. Phases 3-6 have the closest vortex to the airfoil on the top of the airfoil while the plunge location is downward.

The first characteristic is exemplified by comparing the generated vortex location with respect to the plunge displacement of the representative phase. In each phase, the generated vortex develops on the back side of the airfoil with respect to plunge displacement as listed in Table 5**:1**.

The second characteristic can be observed by tracking vortices between images. While these images are not consecutive in time, the repeating motion allows similar generated vortices to be compared. Tracking the bottom vortex between Phase 1 and

Phase 2 of Figure 6-2 it can be observed that the vortex grows from a diameter of $0.75c$ in Phase 1 to $1.5c$ in Phase 2. In Phase 3, the same vortex has shed completely from the airfoil and grown to a diameter of $1.75c$ and increases to $2.0c$ in Phase 4. After Phase 4 the shed vortex is observed but the diameter is difficult to identify accurately with the vortex boundary not identified clearly.

Since the generated vortices are captured on the surface of the airfoil, their spin direction is easily documented with respect to which side of the airfoil they develop.

Using the reference scale presented in the images, the location downstream of where the flow becomes fully turbulent can be documented. Phase 5 presented in Figure 6-2 presents a good example of the flow transitioning from streaklines and vortices easily identified from $0-2c$ behind the trailing edge to becoming dispersed and irregular after $2c$ where the flow has become turbulent. Other phases present a different transition distance from the trailing edge possibly due unsteadiness.

6.3 Comparison with Computational Fluid Dynamics

Since the pitch and plunge motion of the airfoil is symmetrical, half of a cycle (Phases 1-5) was used to compare with CFD results. The CFD vorticity plots are displayed alongside of the representative experimental phase in Figure 6-3.
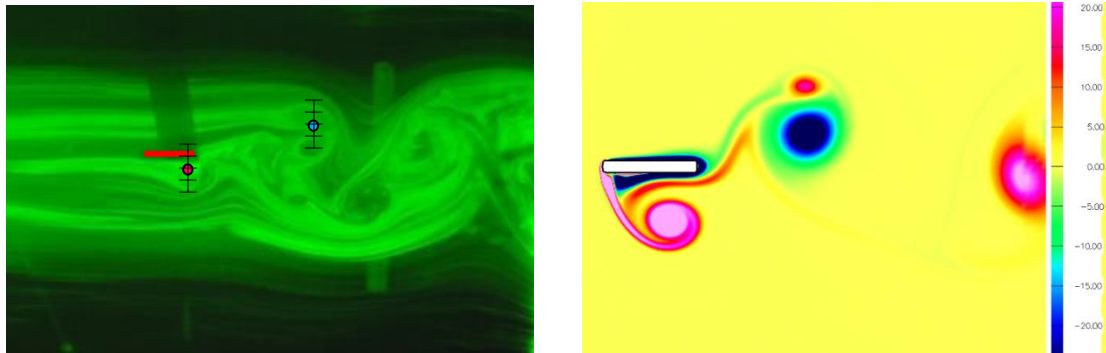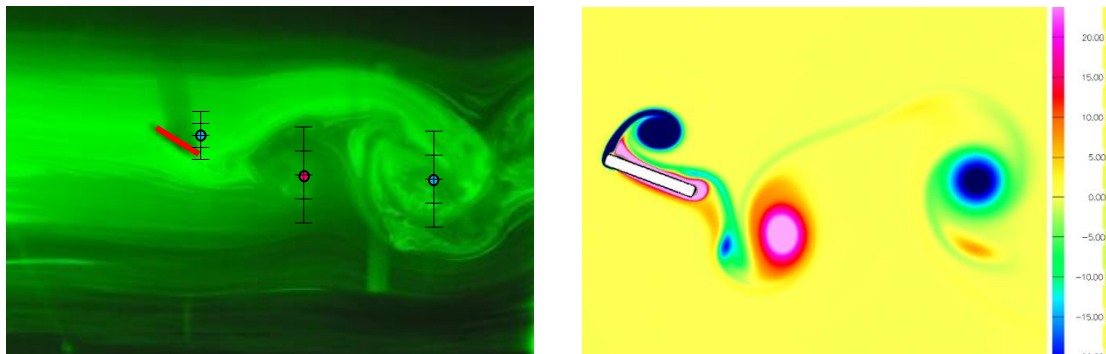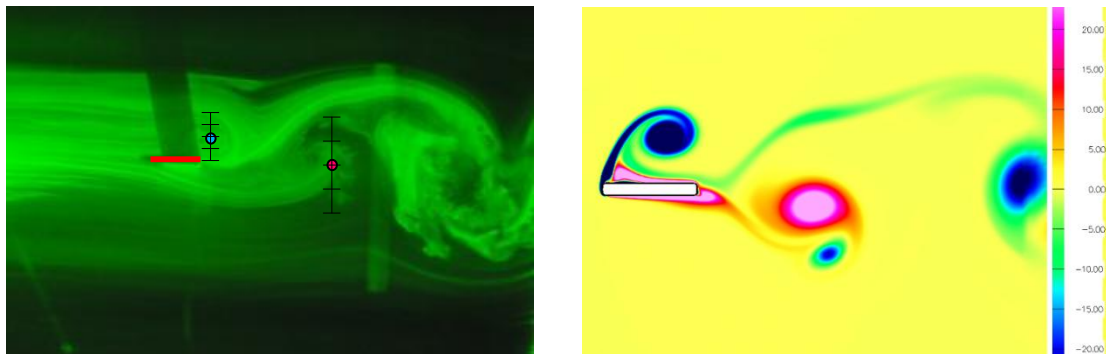

Phase 1
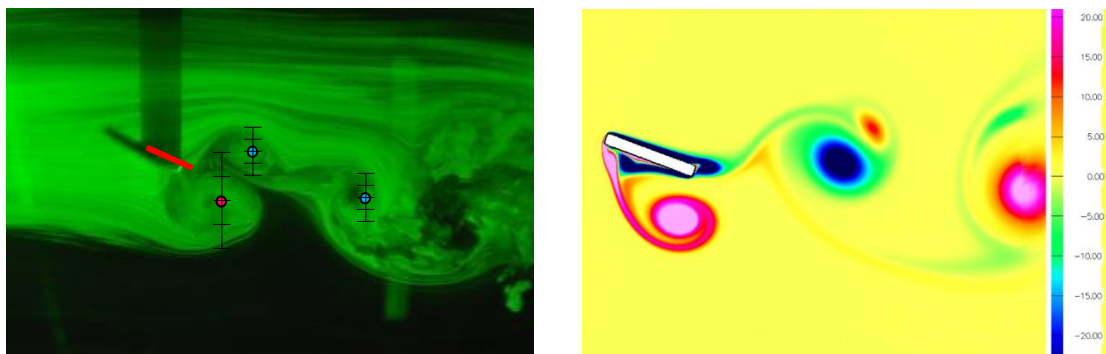
Phase 2
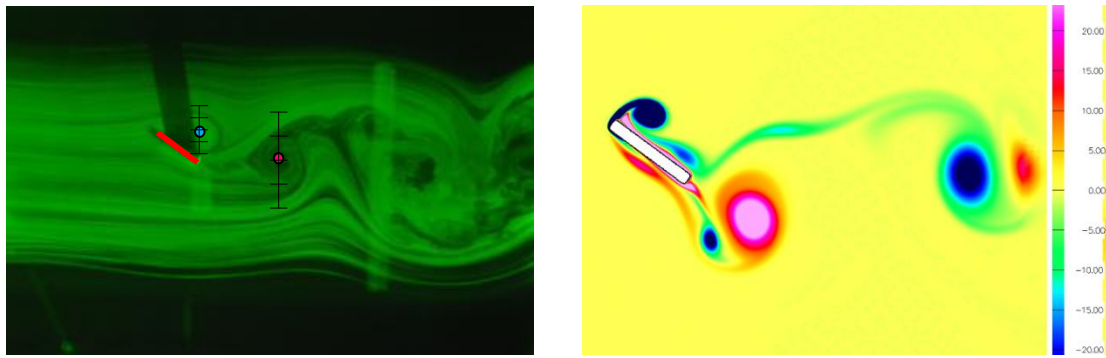
Phase 3

Phase 4

Phase 5

Figure 6-3: Dynamic Experimental vs. CFD Result Comparison

The CFD vorticity plot displays vortex strength but serves well to locate the vortex center and angular rotation. Blue vortices in the CFD result have clockwise while pink vortices have counter-clockwise angular rotation. At each phase, the two results have similar vortex location and angular rotation near the airfoil with a noted difference that the vortex center is consistently further from the airfoil surface for the CFD results than experimental. Also, after the vortex is shed, experimental results show the vortex continues to grow in diameter while the CFD results appears to maintain its shed diameter. Observing flow structure downstream of the CFD result does not represent the turbulence documented earlier for the experimental results. Lack of turbulence in the CFD simulation is due to the simulation not including a turbulence model.

Overall, the experimental and CFD results compare fairly well in terms of shed vortex location and vortex angular rotation direction during the pitch and plunge motion. However, as noted, the vortex center and size differ along with lack of turbulence generated in the CFD simulation. After providing evidence of the dynamic fixture being scaled properly and repeatable, updates to the CFD simulation can be made to improve how well the results match those generated with the wind tunnel PPF.

Chapter 7 : Conclusion

7.1 Summary

Observations documented in both the static and dynamic flow visualizations provide additional insight for low Reynolds number flow around airfoils. The static fixture provided results for low to high angles of attack indicating different corrugations do indeed create different flow structures even at Re_c=1,000. Different flow structures were able to be observed since the investigation compared the corrugated profiles of Kesel (2000) and Murphy (2009) against the standard NACA 0012 airfoil under identical conditions.

Both corrugated profiles performed favorably against the NACA 0012 profile in regards to drag at angles of attack above α=16° by generating smaller separation profiles. Stagnation point location was also found to trend consistently for the investigated airfoils. The NACA 0012 airfoil's stagnation point developed nearer to the leading edge than the corrugated profiles at each investigated angle of attack. At the same time the Murphy (2009) corrugated profile's stagnation point developed sooner than Kesel's (2000) at each angle of attack. This difference in stagnation point location may indicate the lift generated by the Kesel (2000) and Murphy (2009) corrugated airfoils are favorable when compared to the NACA 0012. The main increase in corrugated airfoil performance over the NACA 0012 airfoil appeared in post stall (α > 8°) cases. This is worth noting since the flight motion of a dragonfly, and other flying animals, has high angles of attack as part of its flight path (Shyy, Lian, Tang, Viieru, & Liu, 2008).

Different flow structures generated by the investigated profiles provided insight that corrugated profiles can be created to generate desirable aerodynamic characteristics of lift and drag even in low Reynolds number cases while performing favorably to a standard NACA 0012 airfoil. It was also shown that tuning the corrugated profile can lead to similar NACA four digit series flow structure profiles.

The dynamic fixture also provided valuable flow visualization results for the simplified two-dimensional motion path for a pitching and plunging flat plate. Observations of vortex generation and shedding for the flat plate captured with the dynamic PPF experimental setup are valuable for better understanding flow for this type of motion path. Results from this fixture also provide experimental data capable of being used to validate computational fluid dynamics (CFD) models. Aiding in CFD model validation is extremely important to ensure simulations incorporate proper assumptions which permit actual flow to be accurately modeled.

Development of the PPF flat plate test model yielded that care must be taken when designing a test model to be operated in a pitch-plunge motion to avoid excitation near the natural frequency of the test model. Choosing the natural frequency to be at least twice the excitation frequency in this investigation reduced the test model deflection to an acceptable level.

7.2 Future Work

While the research and results presented in this thesis provide valuable insight to flow generation around static corrugated airfoils and a pitching and plunging flat plate, additional investigations of different corrugated profiles and more angles of attack could provide further understanding around the topic.

Under static conditions, additional corrugated profiles could be investigated to study flow generated by different profiles. This type of investigation could provide more invaluable data in understanding how to create corrugated profiles which generate the desired flow structures.

Documenting flow of more angles of attack below stall would be valuable in comparing corrugated profiles. This investigation covered α = 0,8,16,28,40° but did not document the angle where stall developed for each airfoil. While the stall angle was not a goal of this investigation, knowing this angle would be beneficial in comparing airfoils.

With the dynamic fixture developed and validated, further investigation could entail flow visualizations with corrugated airfoils to compare against flow structures generated with the flat plate. This would be a desirable goal to provide flow structure comparisons of different airfoils.

Expansion of the dynamic fixture to tandem airfoils should also be considered to replicate dragonfly flight more accurately. While this fixture aimed to provide understanding for a single airfoil, real life dragonflies operate with tandem wings and should be a future goal of the fixture. In extending to a more real-life wing motion path, the fixture could be modified to allow phase differences between the pitch and plunge motion. This would allow different motion path patterns to be investigated, such as hovering or maneuvers where direction change occurs.
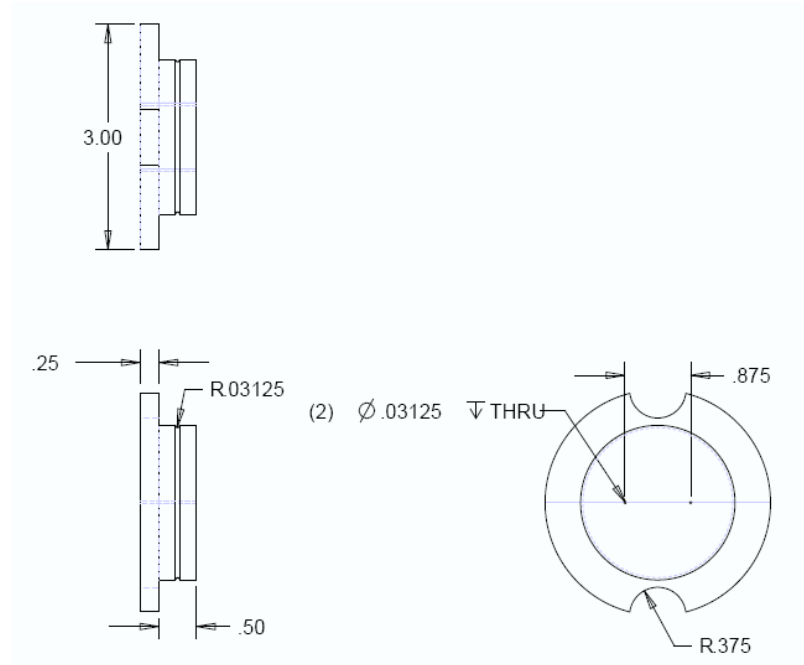
Appendix

Tow Tank Velocity Data

Trial	ω₁ (low)	ω₂ (high)
1	7.7	1.6
2	11.0	1.3
3	10.1	1.4
Average (sec)	9.6	1.4
Trolley Velocity (m/s)	0.1	0.7
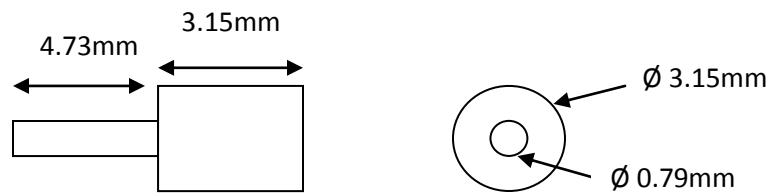
Water Tunnel End Pin

Water Tunnel Model Wall Plug (dimensions in inches)

Top Streakline Separation Distance

		Separation Distance (c)			
	α	Measured			AVG
NACA 0012	0	0.09	xxx	xxx	**0.09**
	8	0.19	xxx	xxx	**0.19**
	16	0.44	0.44	xxx	**0.44**
	28	0.75	0.75	xxx	**0.75**
	40	1.00	1.00	xxx	**1.00**
Murphy	0	0.13	xxx	xxx	**0.13**
	8	0.25	xxx	xxx	**0.25**
	16	0.41	xxx	xxx	**0.41**
	28	0.72	xxx	xxx	**0.72**
	40	0.88	xxx	xxx	**0.88**
Kesel	0	0.06	xxx	xxx	**0.06**
	8	0.16	xxx	xxx	**0.16**
	16	0.38	xxx	xxx	**0.38**
	28	0.66	xxx	xxx	**0.66**
	40	0.84	xxx	xxx	**0.84**

Stagnation Streakline Separation Distance

	α	Separation Distance (*c*)			AVG
		Measured			
NACA 0012	0	0.13	xxx	xxx	**0.13**
	8	0.19	0.13	xxx	**0.16**
	16	0.38	0.44	xxx	**0.41**
	28	0.81	0.88	xxx	**0.84**
	40	1.06	1.13	xxx	**1.09**
Murphy	0	0.19	xxx	xxx	**0.19**
	8	0.19	xxx	xxx	**0.19**
	16	0.38	xxx	xxx	**0.38**
	28	0.81	xxx	xxx	**0.81**
	40	1.00	xxx	xxx	**1.00**
Kesel	0	0.09	xxx	xxx	**0.09**
	8	0.13	xxx	xxx	**0.13**
	16	0.31	xxx	xxx	**0.31**
	28	0.75	xxx	xxx	**0.75**
	40	0.97	xxx	xxx	**0.97**

Stagnation Point Location Distance

|	α	Separation Distance (*c*)	
		Measured	AVG
NACA 0012	0	0.00	**0.00**
	8	0.00	**0.00**
	16	0.03	**0.03**
	28	0.06	**0.06**
	40	0.09	**0.09**
Murphy	0	0.00	**0.00**
	8	0.00	**0.00**
	16	0.05	**0.05**
	28	0.09	**0.09**
	40	0.13	**0.13**
Kesel	0	0.00	**0.00**
	8	0.00	**0.00**
	16	0.09	**0.09**
	28	0.11	**0.11**
	40	0.14	**0.14**

Plunge Displacement Comparison

| Time (s)	Recorded Motion (m)	Desired Motion (m)	Absolute Error (m)	Time (s)	Recorded Motion (m)	Desired Motion (m)	Absolute Error (m)
0	-0.011	-0.013	0.002	0.5	0.001	0.000	-0.001
0.01	-0.006	-0.008	0.002	0.51	-0.005	-0.006	0.001
0.02	0.000	-0.002	0.002	0.52	-0.010	-0.012	0.001
0.03	0.006	0.004	-0.002	0.53	-0.014	-0.016	0.002
0.04	0.012	0.010	-0.002	0.54	-0.016	-0.018	0.002
0.05	0.017	0.015	-0.002	0.55	-0.017	-0.019	0.002
0.06	0.019	0.018	-0.002	0.56	-0.016	-0.017	0.002
0.07	0.020	0.019	-0.001	0.57	-0.013	-0.014	0.001
0.08	0.019	0.018	0.000	0.58	-0.009	-0.009	0.000
0.09	0.016	0.015	0.000	0.59	-0.003	-0.003	0.000
0.1	0.011	0.011	0.000	0.6	0.003	0.003	0.000
0.11	0.005	0.005	0.000	0.61	0.009	0.009	0.000
0.12	-0.001	-0.001	0.000	0.62	0.015	0.014	-0.001
0.13	-0.007	-0.007	0.000	0.63	0.018	0.017	-0.001
0.14	-0.012	-0.012	0.000	0.64	0.020	0.019	-0.001
0.15	-0.015	-0.016	0.001	0.65	0.019	0.018	-0.001
0.16	-0.017	-0.019	0.002	0.66	0.017	0.016	-0.001
0.17	-0.017	-0.019	0.002	0.67	0.013	0.012	-0.002
0.18	-0.015	-0.017	0.002	0.68	0.008	0.006	-0.002
0.19	-0.012	-0.013	0.001	0.69	0.002	0.000	-0.002
0.2	-0.007	-0.008	0.001	0.7	-0.004	-0.006	0.002
0.21	-0.001	-0.002	0.001	0.71	-0.009	-0.012	0.002
0.22	0.005	0.004	-0.001	0.72	-0.014	-0.016	0.002
0.23	0.011	0.010	-0.002	0.73	-0.016	-0.018	0.002
0.24	0.016	0.014	-0.001	0.74	-0.017	-0.019	0.002
0.25	0.019	0.018	-0.001	0.75	-0.016	-0.017	0.001
0.26	0.020	0.019	-0.001	0.76	-0.013	-0.014	0.001
0.27	0.019	0.018	0.000	0.77	-0.009	-0.009	0.000
0.28	0.016	0.016	-0.001	0.78	-0.004	-0.003	0.000
0.29	0.012	0.011	0.000	0.79	0.002	0.003	0.001
0.3	0.006	0.006	0.000	0.8	0.008	0.009	0.001
0.31	0.000	-0.001	0.000	0.81	0.014	0.014	0.000
0.32	-0.006	-0.007	0.001	0.82	0.018	0.017	-0.001
0.33	-0.011	-0.012	0.001	0.83	0.020	0.019	-0.001
0.34	-0.015	-0.016	0.001	0.84	0.019	0.018	-0.001
0.35	-0.017	-0.018	0.002	0.85	0.018	0.016	-0.002
0.36	-0.017	-0.019	0.002	0.86	0.014	0.012	-0.002
0.37	-0.015	-0.017	0.002	0.87	0.009	0.006	-0.002
0.38	-0.012	-0.014	0.001	0.88	0.003	0.000	-0.003
0.39	-0.008	-0.009	0.001	0.89	-0.003	-0.006	0.003
0.4	-0.002	-0.003	0.001	0.9	-0.009	-0.011	0.003
0.41	0.004	0.003	0.000	0.91	-0.013	-0.016	0.003
0.42	0.010	0.009	-0.001	0.92	-0.016	-0.018	0.002
0.43	0.015	0.014	-0.001	0.93	-0.017	-0.019	0.002
0.44	0.019	0.017	-0.001	0.94	-0.016	-0.018	0.001
0.45	0.020	0.019	-0.001	0.95	-0.014	-0.014	0.001
0.46	0.019	0.018	-0.001	0.96	-0.010	-0.009	-0.001
0.47	0.017	0.016	-0.001	0.97	-0.005	-0.004	-0.001
0.48	0.012	0.011	-0.001	0.98	0.001	0.003	0.001
0.49	0.007	0.006	-0.001	0.99	0.008	0.009	0.001
				1	0.013	0.014	0.000
						St Dev.	0.001
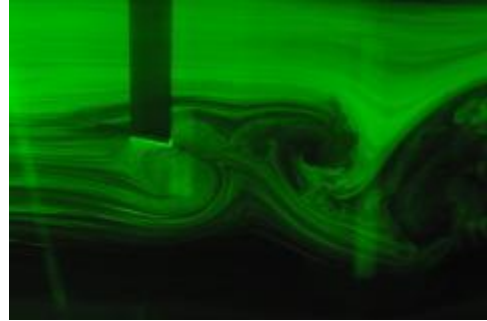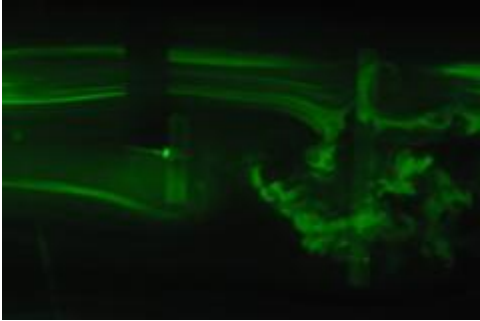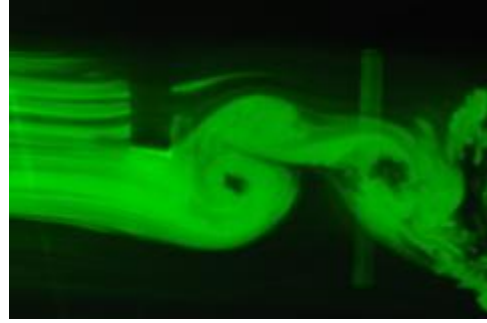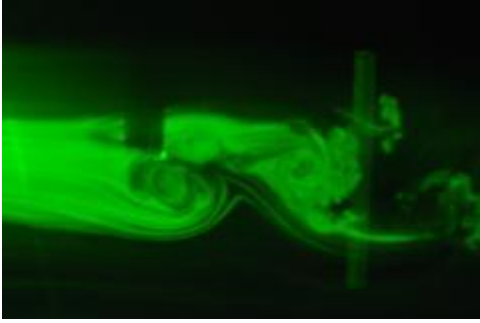
Additional Phase #1 Images
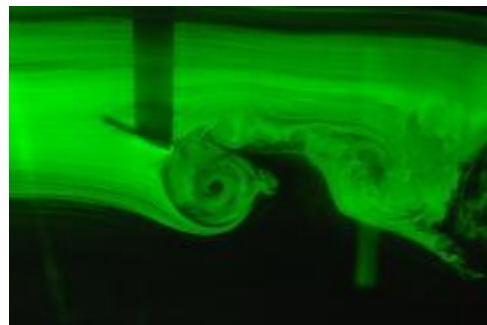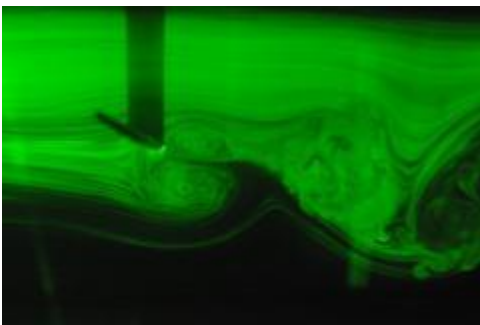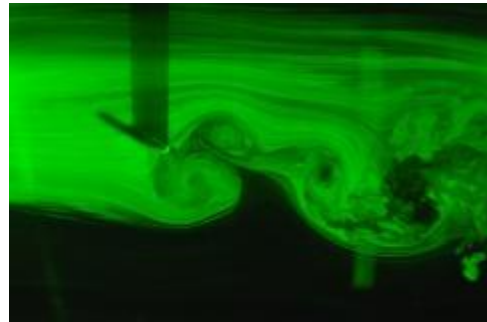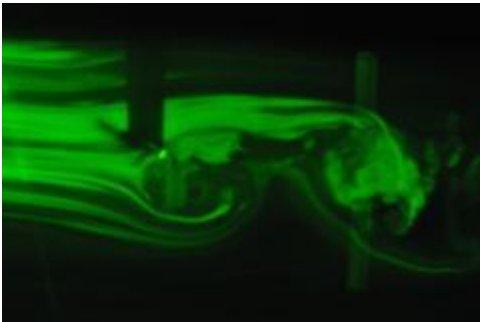
Additional Phase #2 Images
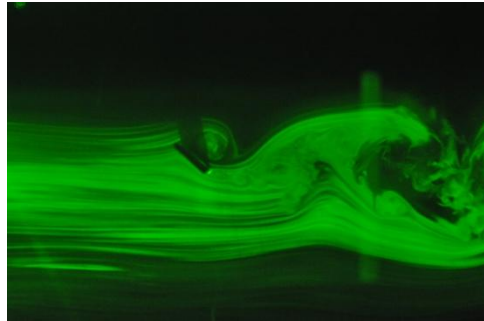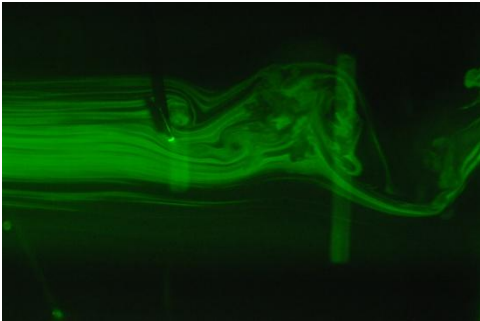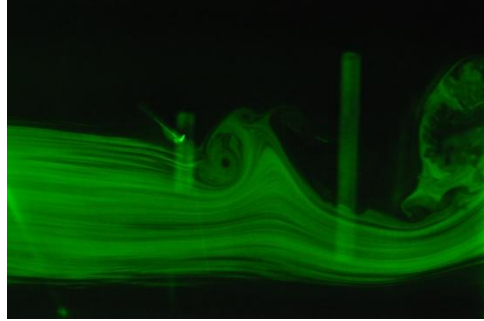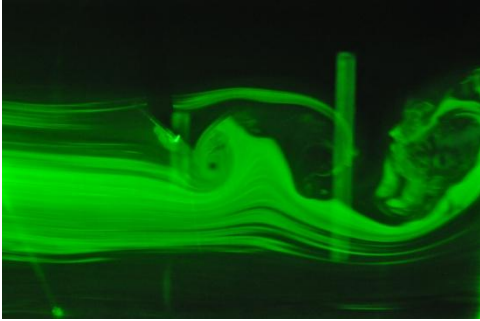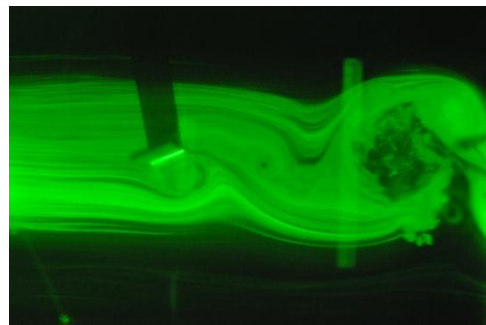
Additional Phase #3 Images
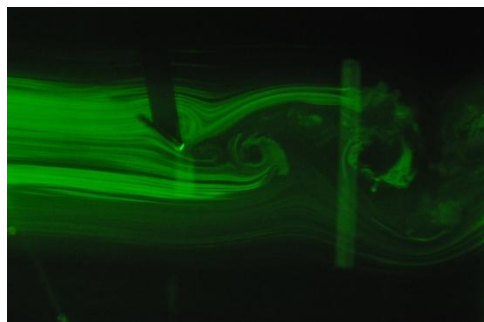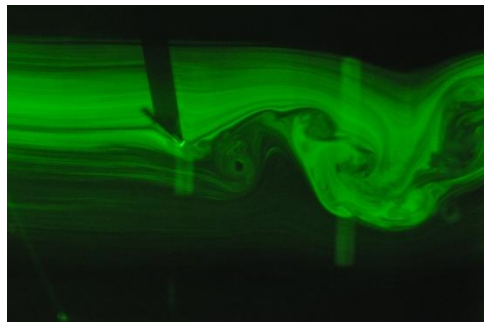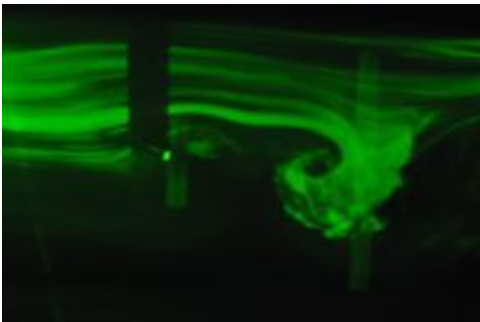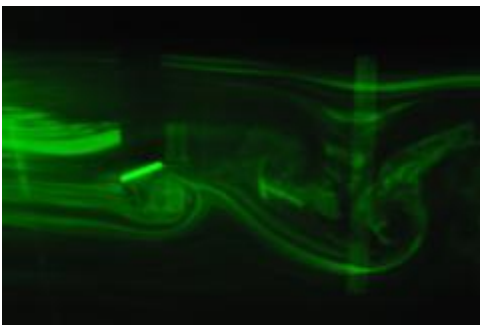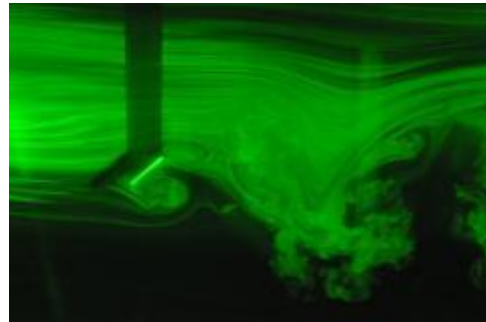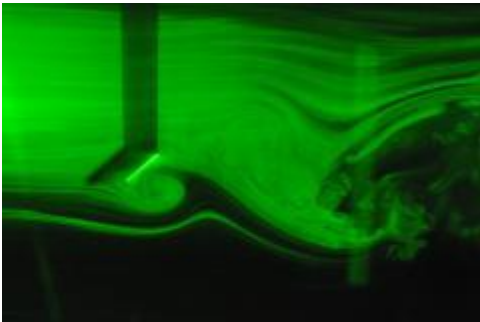

Additional Phase #4 Images
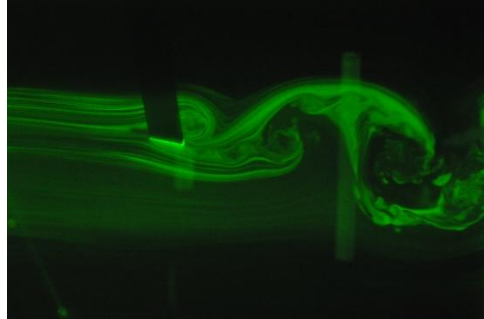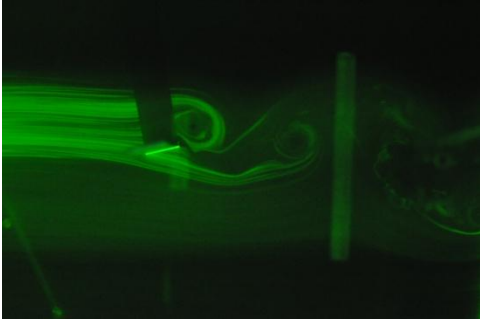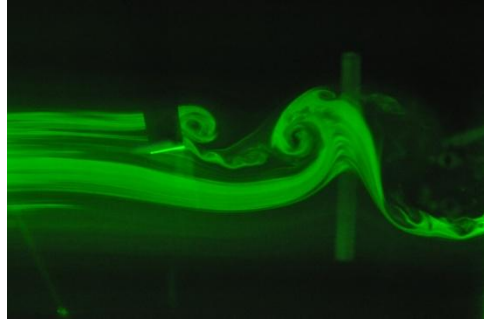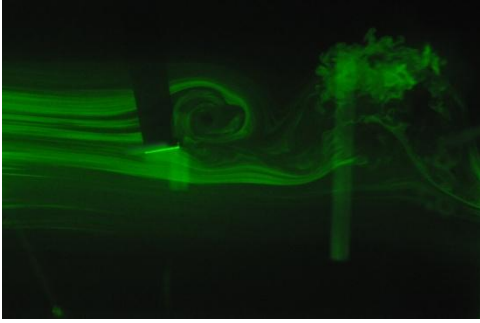
Additional Phase #5 Images
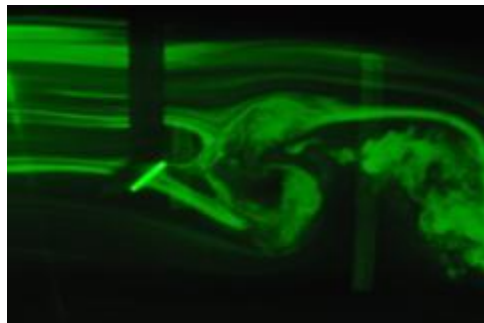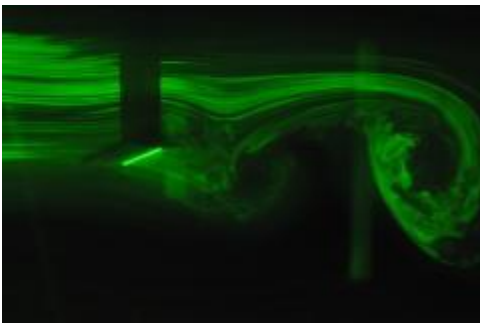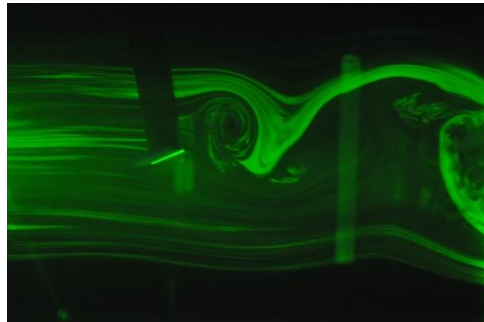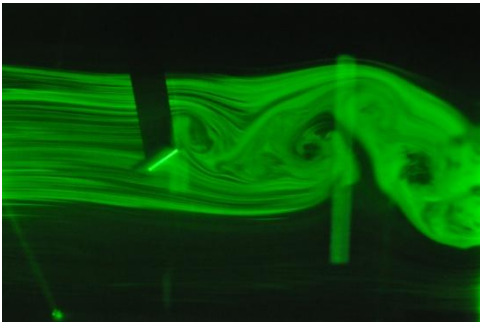
Additional Phase #6 Images
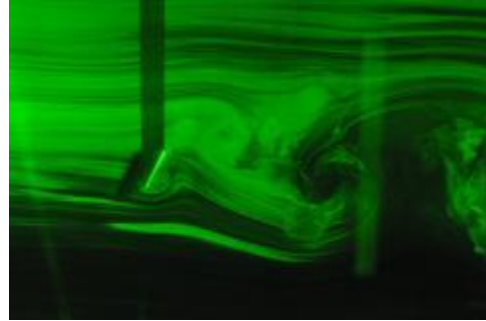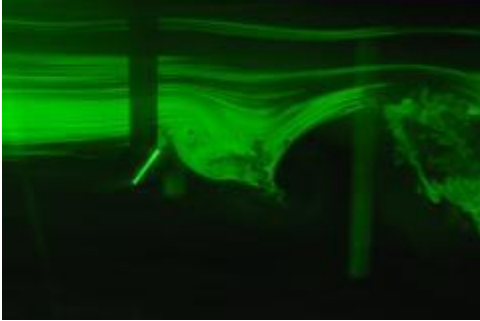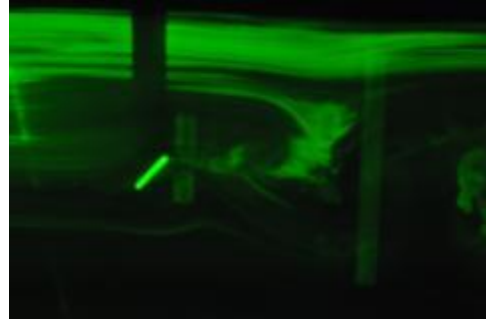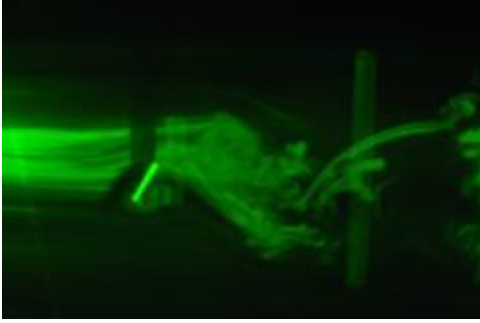
Additional Phase #7 Images

Additional Phase #8 Images

References

Abbott, I. H., & Von Doenhoff, A. E. (1959). *Theory of Wing Sections: including a summary of airfoil data.* Mineola, NY: Dover Publications.

Batchelor, G. (2000). *An Introduction to Fluid Dynamics.* New York, NY: Cambridge University Press.

Freymuth, P. (1990). Thrust Generation by an Airfoil in Hover Modes. *Experiments in Fluids v9*, 17-24.

Hord, K., & Lian, Y. (2011, June 21). Numerical Investigation of the Aerodynamic and Structural Characteristics of a Corrugated Foil. Louisville, KY, USA.

Kesel, A. B. (2000). Aerodynamic Characteristics of Dragonfly Wing Sections Compared with Technical Airfoils. *The Journal of Experimental Biology*, 3125-3135.

Kwok, M., & Mittal, R. (2005). Experimental Investigation of the Aerodynamics of a Modeled Dragonfly Wing Section. *Region I-MA Student Conference.* Charlottesville, VIrginia: American Institute of Aeronautics and Astronautics.

Murphy, J., & Hu, H. (2009). An Experimental Investigation on a Bio-inspired Corrugated Airfoil. *47th AIAA Aerospace Sciences Meeting Including The New Horizons Forum and Aerospace Exposium.* Orlando, Florida: American Institute of Aeronautics and Astronautics.

Okamoto, M., Yasuda, K., & Azuma, A. (1996). Aerodynamic Characteristics of the Wings and Body of a Dragonfly. *The Journal of Experimental Biology*, 281-294.

Shyy, W., Lian, Y., Tang, J., Viieru, D., & Liu, H. (2008). *Aerodynamics of Low Reynolds Number Fliers.* New York, NY: Cambridge University Press.

Simpson, R. L. (n.d.). *DyPPiR Research Overview*. Retrieved August 2, 2011, from Virginia Tech Aerospace & Ocean Engineering Research: http://www.aoe.vt.edu/research/facilities/dyppir/dyp_ovr.html

Sunada, S., Yasuda, T., Yasuda, K., & Kawachi, K. (2002). Comparison of Wing Characteristics at an Ultralow Reynolds Number. *Journal of Aircraft*, 331-338.

Thompson, W. T. (1993). *Theory of Vibrations with Applications.* Prentice Hall.

Vargas, A., & Mittal, R. (2004). Aerodynamic Performance of Biological Airfoils. *2nd Flow Control Conference.* Portland, Oregon: American Institute of Aeronautics and Astronautics.

Vargas, A., Mittal, R., & Dong, H. (2008). A Computational Study of the Aerodynamic Performance of a Dragonfly Wing Section in Gliding Flight. *Bioinspiration and Biomimetics*.

Wakeling, J., & Ellington, C. (1997). Dragonfly Flight: Gliding Flight and Steady-State Aerodynamic Forces. *The Journal of Experimental Biology*, 543-556.

Wilcox, D. c. (2003). *Basic Fluid Mechanics.* La Canada, California: DCW Industries.

Vita

1. Date and place of birth: August 1, 1984 Richmond, Kentucky
2. Educational Institutions attended and degrees already awarded:
   Bachelor of Science in Mechanical Engineering and Mathematics Minor, May 2009, University of Kentucky, Lexington, KY
3. Professional positions held:
   Estill County High School Head Baseball Coach
   College of Engineering Ambassador
4. Scholastic and professional honors:
   Dean's List Recipient: Spring 2003, Fall 2004, Spring 2005, Fall 2008, Spring 2009
5. Professional Publications: *Experimental Low Reynolds Number Plunge and Pitch Fixture Development*. Presentation. 36th Annual Dayton-Cincinnati Aerospace Sciences Symposium March 1, 2011.
6. Student Name: Jeremy Ryan Sparks